Optical study of strongly correlated electrons in metals

GURITANU, Violeta

Abstract

My thesis concerns the application of optical spectroscopy to transition metals, heavy fermions and superconductors to explore and understand the electronic properties of these materials. It includes the magnetic materials FeGe, UG[e2] and Gd?Si?Ge?, at low temperatures and the superconductor MgB?. I present a detailed optical study of compounds from the 3 main categories of the periodic system: iron series, actinides and rare earth elements represented by Fe, U and Gd atoms. In FeGe, with Tc=280K, I find a moderate mass enhancement below 100meV, indicating the formation of heavy electrons. Similar result I obtain for UG? with Tc=53K, except that temperature and energy scale are much lower 30meV. In addition I notice that the magnetic order triggers the transition into a state characterized by heavy and weakly scattered charge carriers. For Gd?Si?Ge?, with Tc=267K, I provide an original evidence for a new phase transition below 45K. In the last chapter of my thesis I present optical experiments on two-band superconductor [...]

GURITANU, Violeta. *Optical study of strongly correlated electrons in metals*. Thèse de doctorat : Univ. Genève, 2008, no. Sc. 4051

UNIVERSITÉ DE GENÈVE
Département de physique de la matière condensée

FACULTÉ DES SCIENCES
Professeur D. van der Marel

Optical study of strongly correlated electrons in metals

THÈSE

*présentée à la Faculté des sciences de l’Université de Genève
pour obtenir le grade de Docteur ès sciences, mention physique*

par

Violeta Guritanu
de
Chisinau (République de Moldavie)

Thèse n° 4051

GENÈVE
Atelier d’impression ReproMail
2008

This thesis is dedicated to Andrey, Alexandru and Valentina for
their support, encouragement, love and understanding.

Contents

Résumé en français

La spectroscopie optique est un outil expérimental puissant pour l'étude de la réponse électrodynamique des solides. De nos jours, la spectroscopie optique est considérée comme l'une des méthodes principales pour déterminer la structure de bandes des solides. Les matériaux d'intérêt actuel, qui sont étudiés dans cette thèse, sont notamment des métaux de transition, des fermions lourds et des supraconducteurs à haute température critique. L'objectif de ce travail est d'utiliser la spectroscopie optique, afin d'étudier et de comprendre l'impact des interactions fortes, et du couplage avec les phonons ou les fluctuations de spin sur la masse effective et la durée de vie de quasi-particules.

L'évidence optique de la présence d'électrons lourds dans le FeGe

Les composés intermétalliques avec une structure cristalline de type B20 ont suscité un grand intérêt en raison de leurs propriétés électriques et magnétiques. Le composé itinérant FeGe, qui présente un ordre hélimagnétique [1] en-dessous de 280 K, fait parti de cette famille. Un aspect intéressant de ce matériau est que, même si c'est un bon métal à basse température, une transition métal-isolant de Kondo apparait quand le Ge est remplacé par le Si dans la série $\mathrm{FeSi}_{1-x}\mathrm{Ge}_x$ pour une concentration critique de $x \approx 0.25$ [2].

Dans le chapitre 3, nous présentons les résultats de l'étude optique détaillée d'un monocristal de FeGe à différentes températures. Les parties réelles et imaginaires de la fonction diélectrique ont été obtenues à partir des mesures de réflectivité infrarouge et de spectroscopie ellipsométrique. Les spectres optiques du FeGe montrent la présence d'une importante transition interbande à 0.22 eV et une dynamique particulière des porteurs de charge libres [3]. L'analyse détaillée des données optiques révèle une renormalization de la masse effective et un taux de diffusion dépendant de la fréquence à basse température et basse fréquence. Nous observons que $m^*(\omega)/m \sim 5$ à 30 K dans la limite ou $\omega \to 0$.

Notre étude indique que la réponse optique du FeGe est assez semblable à celle des fermions lourds. Contrairement aux cas des fermions lourds, FeGe n'a ni d'électrons $4f$ ni d'électrons $5f$, mais présente malgré tout une masse effective éllevée. Dans les fermions lourds l'interaction entre la répulsion coulombienne des électrons f et leur hybridation avec une bande large des électrons de conduction conduit à une forte augmentation de la masse effective de la bande des électrons libres au niveau de Fermi. FeGe est un système avec des électrons $3d$, où les fonctions d'onde $3d$ sont relativement étendues par rapport aux fonctions d'onde des électrons $4f$ ou $5f$, ce qui entraîne une augmentation relativement petite de la masse effective. Dans ce contexte, nous montrons que FeGe devrais être considéré comme un système $3d$ avec des électrons lourds.

L'électrodynamique du fermion lourd UGe$_2$

Les composés à base d'uranium sont largement étudiés en raison de la variété des propriétés telles que le ferromagnétisme et la supraconductivité exhibées par ces systèmes. Récemment, la coexistence de la supraconductivité et du ferromagnétisme a été observée dans l'UGe$_2$ sous pression [4]. UGe$_2$ est un système ferromagnétique fortement anisotrope avec une température Curie de 53 K. De plus une autre transition magnétique a été détectée en-dessous de 30 K. Dans l'expérience de Haas-van Alphen (dHvA) des porteurs de charge avec des masses effectives relativement importantes $[(10-25)m_0]$ ont été retrouvés [5]. Il a donc été proposé que les électrons $5f$ dans l'UGe$_2$ soient itinérants, indiquant un magnétisme de bande, comme dans les systèmes avec des électrons $3d$.

Nous avons mesuré les propriétés optiques d'un monocristal d'UGe$_2$ dans la gamme d'énergie de 6.2 meV à 3.7 eV pour différentes températures allant de 11 K à 290 K, à pression ambiante. Comme on le verra dans le chapitre 4, une augmentation significative de la réflectivité se produit à travers la transition ferromagnétique. En outre, plusieurs structures remarquables apparaissent à basse fréquence et température, y compris un mode à fréquence zéro, très étroit, avec une forte dépendance en fréquence de la masse effective et du taux de diffusion [6]. L'analyse de la dépendance en température de la masse effective et du taux de diffusion montre que le magnétisme joue un rôle important dans la formation des quasi-particules lourdes dans l'UGe$_2$. En particulier, nous constatons que la formation de l’état fermion lourd débute à la même température que la transition ferromagnétique. Il s’agit d’un aspect très intéressant qui n’a pas encore été examiné. En outre, la dépendance en fréquence du taux de diffusion à basse température peut-être compatible avec le modèle de Stoner du magnétisme itinérant.

Une nouvelle transition de phase dans le $Gd_5Si_2Ge_2$

Depuis la découverte de l’effet magnétocalorique géant dans le $Gd_5Si_2Ge_2$ près de la température ambiante [7, 8], ce matériau a été largement étudié comme un candidat prometteur, respectueux de l’environnement, pour des systèmes de réfrigération magnétique [9]. $Gd_5Si_2Ge_2$ est un système ferromagnétique localisé, qui montre une variété de propriétés uniques associées à sa transition magnéto-structurelle. Comme une telle transition de phase implique des changements dans la structure électronique, il est intéressant d’examiner la structure électronique de ce système par des mesures optiques.

Nous avons étudié les propriétés optiques du matériau anisotrope $Gd_5Si_2Ge_2$ à différentes températures et fréquences. Notre étude optique présentée dans le chapitre 5 suggère la présence d’une nouvelle transition de phase en-dessous de 45 K. Dans le spectre optique cette transition est marquée par une forte diminution de la réflectivité et une importante perte du poids spectrale à basse température. Bien que les données optiques montrent une forte évolution, aucun signe d’une anomalie n’est observé dans les mesures de résistivité et d’aimantation à basse température.

Les deux couleurs du MgB_2

Le diboride de magnésium est un matériel bien connu, mais ce n’est que récemment que l’intérêt pour ce composé a été renforcé en raison de la découverte de la supraconductivité à une température relativement élevée de 40 K [10] pour un supraconducteur "classique" électron-phonon. En outre deux bandes supraconductrices [11] ont été mises en évidence. Cette particularité du composé MgB_2 offre la possibilité d’étudier l’électrodynamique de la supraconductivité à deux bandes.

Dans le chapitre 6 nous présentons une étude systématique des propriétés optiques du MgB_2 à température ambiante. Les parties réelles et imaginaires des conductivités optiques dans le plan et perpendiculaire au plan ont été déterminées à partir des mesures de réflectivité et d’ellipsométrie sur un cristal d’orientation ab et, pour la première fois, sur un cristal orienté selon l’axe c. Les mesures montrent une grande valeur, presque isotrope, de la fréquence de plasma (≈ 6.3 eV) [12]. Nous avons trouvé différentes fréquences de plasmas écrantées pour les deux polarisations. Cependant, cette anisotropie est due à l’écrantage supplémentaire des porteurs de charge par une transition interbande à 2.6 eV, qui est active optiquement dans le plan ab, plutôt qu’à l’anisotropie de la fréquence de plasma elle-même. Une belle manifestation de cette forte anisotropie reflète l’apparition multicolore du MgB_2. Les spectres anisotropes sont en bon accord avec les calculs de la structure de bandes et avec l’interaction électron-phonon. Nous discutons les corrections éventuelles à apporter à la structure électronique calculée découlant des nos résultats.

Summary in English

Optical spectroscopy is a powerful experimental tool used to investigate the electrodynamic response of solids. Currently, it is considered as one of the principal methods of determining the electron band structure of materials. The materials of current interest, which are studied in this thesis, include transition metals, heavy fermions and high-T_c superconductors. The aim of this work is optical spectroscopy, to explore and understand the impact of strong interactions and coupling to phonons or spin fluctuations on the effective mass and life time of the quasi-particles.

Optical evidence for heavy charge carriers in FeGe

The intermetallic compounds with a cubic B20 type of crystal structures have been very attractive systems to us because of their unusual electric and magnetic properties. Among them, the itinerant electron helimagnet FeGe orders in a helical magnetic structure below 280 K [1]. An interesting aspect of this material is that, even though it is a good metal at low temperatures, there is a transition to a Kondo insulator when Ge is replaced with Si in the compound series $\mathrm{FeSi}_{1-x}\mathrm{Ge}_x$ at the critical concentration of $x \approx 0.25$ [2].

In Chapter 3 we present the results of a detailed optical study of a cubic FeGe single crystal at different temperatures. The real and imaginary parts of the dielectric function were derived from the infrared reflectivity and spectroscopic ellipsometry measurements. Optical spectra of FeGe show the presence of an important interband transition at 0.22 eV and an unusual dynamics of the free-carrier charge [3]. Detailed analysis of the optical data reveals a renormalized effective mass and frequency dependent scattering rate at low-temperature and low-frequency. We observe $m^*(\omega)/m \sim 5$ in the $\omega \to 0$ limit at T = 30 K.

Our study indicates that the optical response in FeGe is quite similar to heavy fermion compounds. In contrast to heavy fermions, FeGe has no $4f$- nor $5f$-electrons, but an enhancement of the effective mass is clearly observed. In heavy fermions the interplay between the strong repulsion of the f-electrons and their hybridization with a wide band of conduction electrons leads to a strong enhancement of the effective mass of the free band electrons at the Fermi level. FeGe is a $3d$ electron system, where $3d$ wave functions are relatively extended compared to the $4f$ or $5f$ wave functions, which results in a relatively smaller enhancement of the effective mass. In this context we show that FeGe should be considered as a $3d$ heavy electron system.

Electrodynamic response of heavy fermion UGe$_2$

Uranium based compounds are widely studied due to the variety of properties such as ferromagnetism and superconductivity exhibited by these systems. Recently, the coexistence of superconductivity and ferromagnetism was found in UGe$_2$ under pressure [4]. UGe$_2$ is a strongly anisotropic uniaxial ferromagnet with T_C = 53 K, additionally a secondary magnetic transition was found below T_x = 30 K. In the de Haas-van Alphen (dHvA) experiment relatively large carrier masses $[(10 - 25)m_0]$ were found [5]. It was thus suggested that $5f$-electrons in UGe$_2$ are itinerant, indicating band magnetism as in the $3d$ electron systems.

We measured the optical properties of a single crystal of UGe$_2$ in the energy range from 6.2 meV to 3.7 eV for different temperatures ranging from 11 K to 290 K at ambient pressure. As will be shown in Chapter 4, significant increase in the reflectivity spectra occurs across the ferromagnetic transition. Furthermore, several remarkable low-frequency features appear at low-temperature, including a very narrow zero-frequency mode with strong frequency dependence of the effective mass and the scattering rate [6]. The analysis of the temperature dependence of the effective mass and the scattering rate show that the magnetism plays an important role in the formation of heavy quasi-particles. In particular, we observe that the onset of the heavy fermion state occurs at the same temperature as the ferromagnetic transition. This is a very interesting aspect that has not yet been considered. Additionally, the frequency dependence of the scattering rate at low temperatures is found to be compatible with the Stoner model of itinerant magnetism.

A new phase transition in $Gd_5Si_2Ge_2$

Since the discovery of the giant magnetocaloric effect in $Gd_5Si_2Ge_2$ near room temperature [7, 8], this compound has been extensively studied as a promising candidate for environmentally friendly magnetic refrigeration systems [9]. $Gd_5Si_2Ge_2$ is a localized moment system, which shows a variety of unique properties associated with the combined magneto-structural transition. As such a phase transition involves changes in the electronic structure, it is of great interest to explore it via optical measurements.

We have investigated the optical properties of the anisotropic compound $Gd_5Si_2Ge_2$ at different temperatures and frequencies. Our optical studies presented in Chapter 5 suggest the presence of a new phase transition below 45 K. In the optical spectra this transition is marked by a strong decrease in the reflectivity spectra and a significant loss of spectral weight at low-temperature. Although the optical data show strong changes, no sign of an anomaly is observed in the resistivity and magnetization measurements at low-temperature.

Two colors of MgB_2

Magnesium diboride is a well-known material, that only recently drew interest in because of the discovery of superconductivity [10] at a remarkably high critical temperature for a "conventional" electron-phonon superconductor, $T_c \sim$ 40 K. Additionally two distinct superconducting gaps [11] have been reported. This peculiarity of MgB_2 offers us the opportunity to study the electrodynamics of two-band superconductivity.

In Chapter 6 we present a systematic analysis of the optical properties of MgB_2 at room temperature. The real and imaginary parts of the in-plane and out-of-plane optical conductivities are derived from the reflectivity and ellipsometry measurements on the ab- and, for the first time, on the ac-oriented crystals. The measurements show a large ($\approx$ 6.3 eV) and almost isotropic plasma frequency [12]. We find different positions of the reflectivity plasma edges for the two light polarizations. However, this anisotropy is due to the extra screening of charge carriers by an interband transition at 2.6 eV, which is optically active along the ab-plane, rather than the anisotropy of the bare plasma frequency itself. A beautiful manifestation of this strong anisotropy reflects the multicolor appearance of MgB_2. The anisotropic spectra are in satisfactory agreement with the first-principles calculations of the band structure and the electron-phonon interaction. We discuss the possible corrections to the calculated electronic structure which follow from the optical results.

Chapter 1

Theoretical Background

The aim of this chapter is to give an overview on magnetism. This includes theoretical approaches which are used to describe the magnetic properties of solids. To begin with, we briefly mention the different types of magnetic ordering. Then we discuss the models of localized and itinerant electron magnetism focusing particularly on a simplified Heisenberg and Stoner models. Next we concentrate on the magnetism of heavy fermions including the discussion of the Doniach diagram and the periodic Anderson model (PAM).

1.1 Introduction

Magnetism in solids arises from the orientation of the magnetic moments of the atoms. These magnetic moments originate from orbital and spin magnetic moments of electrons. The combination of orbital and spin moments for every electron throughout a crystal defines its magnetic properties.

There are several types of magnetic materials: paramagnets, diamagnets and ordered magnetic materials. Ordered magnetic materials may show various magnetic states like ferromagnetism, antiferromagnetism, ferrimagnetism, helimagnetism or more complex types of order. The alignment of the magnetic moments in various ordering states is displayed in figure 1.1.

The simplest kind of magnetic order is ferromagnetism. Generally ferromagnetism is associated with metals like Fe, Ni, Co and some of their alloys. However, in reality this phenomenon is much more complex and widespread. A ferromagnetic material possesses a spontaneous magnetization, which means that it has a non-zero magnetization even in the absence of a magnetic field. The magnetic moments in a ferromagnet have the tendency to become aligned parallel to each other, which leads to a spontaneous magnetization. In some materials like heavy fermions, for example, one can find a multitude of different magnetic orders because they exhibit many magnetic phases.

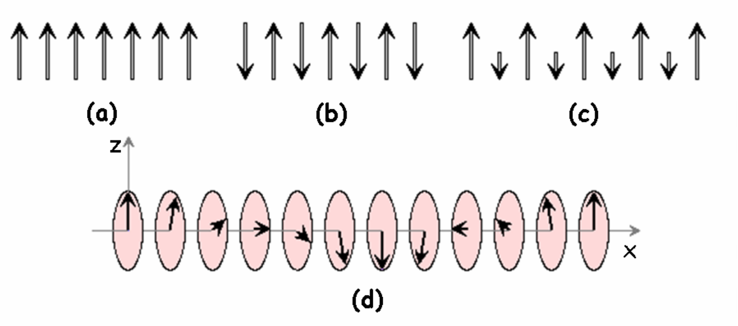

Figure 1.1: Various types of magnetic order. - (a) ferromagnet, (b) antiferromagnet, (c) ferrimagnet and (d) helimagnet.

The transition to an ordered magnetic state takes place at a critical temperature such as the Curie or Néel temperature. Above these temperatures the magnetic moments tend to point in random directions due to thermal fluctuations and the magnetic ordering is destroyed. Therefore above a critical temperature all ordered magnetic materials become paramagnets. The temperature dependence of the magnetic susceptibility in the paramagnetic state is generally described by the Curie-Weiss law.

1.2 Localized and itinerant electron magnetism

The magnetism of materials containing magnetic atoms appears to be much more complex then the magnetism of free atoms due to many body electron interactions. No definitive theoretical solutions exist up to now. However, in many cases models [13, 14] with some simplifications and extensions may be sufficient to account for the experimental observations.

Two main theories have been proposed to describe the origin of magnetism in solids. One theory is based on a localized electron picture, where electrons responsible for magnetism are considered to be localized on a single atom. According to the localized moment model the electrons in a solid arrange themselves in shells in such a way as to maximize the total spin due to Hund's rule. Once a shell is more than half filled, spins begin to pair up within the orbitals and the available magnetic moment decreases. Due to the complete cancellation of spin and orbital magnetic moments a filled shell has no magnetic moment.

For partially filled shells it is possible to have a net magnetic moment per atom. Typical examples are the transitions metals, rare earths and actinides in which the $3d$, $4f$ and $5f$-shells are incompletely filled.

The magnetism of a solid is described by the magnetization, M, defined as the sum of all individual magnetic moments per unit volume. At small fields the magnitude of magnetization is proportional to the applied field ($M = \chi H$) where the proportionality constant is the magnetic susceptibility, χ.

The second theory is the itinerant electron model, where the electrons responsible for magnetism are the completely delocalized conduction electrons.

A natural question, however, arises: "How can one decide whether a system is described by a localized or itinerant picture?" It is often very difficult and sometimes even meaningless, to associate experimental data with one of these theoretical approaches. However, nice physical ideas are contained in these models. The temperature dependence of the magnetic susceptibility of most ferromagnetic systems above T_C can be fitted with the Curie-Weiss law. This allows one the obtaining of the paramagnetic moment, which is regarded as an important measure of the degree of itinerancy of magnetism. This can be understood as follows: for localized spins the magnetic moment is largely conserved; it would have a value very close to the free ion. However, in itinerant ferromagnets the saturation moment arises from the different partial occupations of the spin-up and spin-down bands characterized by reduced atomic moments. The reduction of the magnetic moments reflects the itinerant behaviour.

1.2.1 Heisenberg model

The Heisenberg model [15] describes the quantum mechanical direct exchange interaction between two neighbouring electrons with overlapping wave functions. The main idea of this model goes back to the Heitler-London theory that used the exchange interaction to explain the binding energy of the hydrogen molecule. Heisenberg developed the theory of ferromagnetism by considering the exchange interaction of Heitler-London theory as an interaction between the spins on two neighbouring atoms. In this approach the hamiltonian of the spin system is commonly given by the exchange interaction as:

$$H = -\sum_{i,j} J_{i,j} \vec{S}_i \vec{S}_j, \tag{1.1}$$

where the summation extends over the nearest neighbour pairs. Here $J_{i,j}$ represents the exchange coupling constant between the atoms i and j, with spins $\vec{S}_i$ and $\vec{S}_j$. When we put $J_{i,j}$ equal to zero we obtain a free ion moment that will exhibit the Curie susceptibility. Therefore, in case of interacting system one should expect to find the Curie law for $T \gg J_{i,j}$. This model (sketched in figure 1.2) assumes that the exchange integral, $J_{i,j}$, is identical for all nearest neighbours.

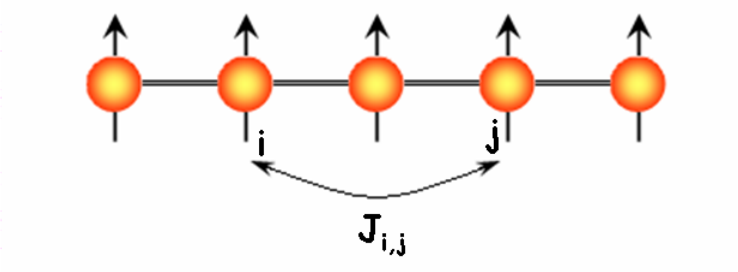

Figure 1.2: Heisenberg model. - Schematic illustration of Heisenberg model based on a localized moment picture.

The exchange interaction is a consequence of the Pauli principle that excludes the possibility of finding two electrons with the same quantum numbers on the same site. On the basis of this model one finds a limit where $J_{i,j} > 0$ is positive, in which case we have a situation that favours the parallel alignment of spins, and a situation, where $J_{i,j} < 0$ that corresponds to an antiferromagnetic ordering. As can be seen from the Heisenberg hamiltonian, flipping the direction of a single spin costs the neighbouring atoms the exchange energy. Within this approach the linear temperature dependence of the inverse magnetic susceptibility, predicted by the Curie-Weiss law, is naturally explained. Additionally, in the systems with localized moments one expects to find a saturation magnetization, which is an integer multiple of the Bohr magneton, μ_B.

The localized moment model has been widely used to discuss the magnetism in many magnetic compounds: in particular in the lanthanide series of elements, where the $4f$-electrons are closely bound to atomic cores. However, this model seems to fail to describe magnetism in transition metals. There are two main discrepancies with the experimental observations: Firstly, according to the localized moment theory the magnetic moments on each atom should be the same for both paramagnetic and ferromagnetic phases, while experimentally a reduced magnetic moment is found in the ferromagnetic phase compared to the paramagnetic one. The second discrepancy is that the magnetic moment on each atom or ion should correspond to an integer number of electrons. Usually a non-integral number of the magnetic moments per atom is obtained.

1.2.2 Stoner model

The simplest model that describes the ferromagnetic materials is considered the Stoner model [14] called also the itinerant electron or band model. In this theory the conduction electrons are considered relatively free to move through the crystal and their atomic energy levels are spread out to form energy bands. In a conventional itinerant ferromagnet, single particle excitations named Stoner excitations exist in addition to the spin waves excitation. The general picture of magnetic excitations is summarised in figure 1.3. For the zero wave vector the Stoner excitations require an energy E_{ex} to occur, while at higher momentum transfer the minimum energy for Stoner excitation is Δ. In addition to this one-particle excitation low-lying excited states are present in the Stoner excitation spectrum. These collective excitations called spin waves are represented as a quadratic dispersion in figure 1.3(a). The energy required for such excitation is much smaller then for Stoner excitations and may even be zero. This small energy for spin waves occurs because the spins are almost parallel and the restoring force is small.

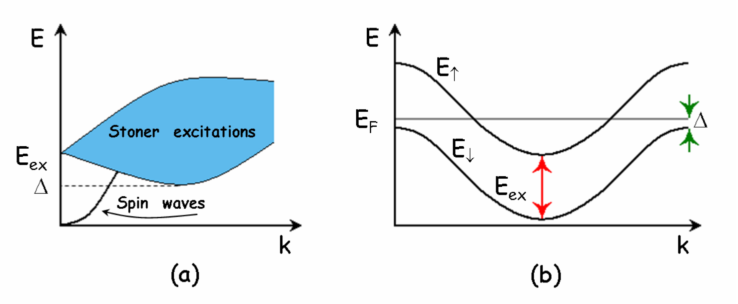

Figure 1.3: Stoner model for itinerant magnetism. - (a) The blue area represents the Stoner continuum of single electron excitations. Spin waves are shown as a quadratic dispersion. In the region close to Stoner excitations, spin waves strongly decay into electron excitations. (b) Exchange-split parabolic bands $(E_{\uparrow}, E_{\downarrow})$ with the spin-down band below the Fermi level, E_F, illustrating a strong ferromagnet. Here Δ is the Stoner gap and E_{ex} is the exchange energy as described in the text.

A model band structure of this approach is represented in figure 1.3(b). The spin-up direction is shifted relative to the spin-down direction by the exchange energy, E_{ex}. In this situation the spin-down band lies completely below the Fermi energy, which represents a strong ferromagnet. The energy and wave vector transfer needed to excite an electron from an occupied spin-down state to an unoccupied spin-up state is sketched in figure 1.3(a) as a blue area. For strong ferromagnets the minimum energy to flip a spin is given by the distance between the top of the occupied band and the Fermi level which defines the Stoner gap, Δ.

The occurrence of ferromagnetism in a system can be studied using the Stoner condition $IN(\epsilon_F) > 1$. This relation describes a competition between the exchange interaction, I, that drives the system into the ferromagnetic state and the non-magnetic density of states, $N(\epsilon_F)$, at the Fermi level. Thus, the ferromagnetic behaviour is favoured for a large exchange integral but also for a high density of states at the Fermi energy that makes the non-magnetic state unstable. A schematic band diagram for ferromagnetism is sketched in figure 1.4. There are two subbands corresponding to the up and down spin electrons [see figure 1.4(a)]. When ferromagnetism occurs, the spin-up band and the spin-down band are shifted in energy with respect to each other by the exchange splitting integral $E_{ex} = IM$, where M is the value of the magnetic moment. This leads to a different density of states at the Fermi level for the two subbands. If the two spin bands are not filled as sketched in figure 1.4(b), the system is called a weak ferromagnet. This configuration usually leads to a non-integer number of the magnetic moments per atom. If the exchange splitting is large enough, it can lead to a complete energy separation between the two spin bands as illustrated in figure 1.4(c) and then the system is called a strong ferromagnet or half-metallic ferromagnet. This strong magnetism in closely related to the strong ferromagnetism in Co and Ni except that they have $4s$ bands of both spin characters at the Fermi level. More specifically, the strong magnetism refers to a situation where the Fermi level lies in a gap, or low density of states region, of either the spin-up or spin-down bands. As a consequence, the conduction electrons are fully spin-polarized at the Fermi level as in, for example, CrO_2. In this case an integer number of magnetic moments per atom is expected.

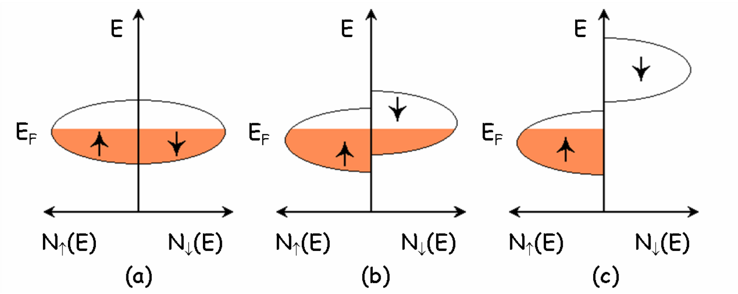

Figure 1.4: Sketch of the spin dependent density of states. - The colored region shows the occupied electron states. $N_\uparrow$ and $N_\downarrow$ indicate the spin dependent density of states at the Fermi energy for: (a) paramagnet, (b) weak ferromagnet and (c) strong ferromagnet.

The Stoner theory seems to give a correct description of the ground state of many transition metals, in particular it explains the non-integer number of the magnetic moments at zero temperature. However, it can not describe the finite temperature properties such as the Curie-Weiss susceptibility. In particular it overestimates the value of the ferromagnetic transition temperature compared to experiments. These discrepancies are satisfactorily explained in the self-consistent renormalization theory of spin fluctuation and by other related theoretical approaches [16].

1.3 Magnetism of rare earth systems

Heavy fermions present a very interesting class of materials essentially because of their non-universal behaviour. Various phenomena like magnetism, superconductivity and non-Fermi liquid behaviour have been reported. In most cases these compounds contain rare earth or actinide elements from the f transition metal series namely Ce, Yb, and U where the $4f$ and $5f$-electron states are relatively close to the Fermi energy. To distinguish them from normal metals, heavy fermions are defined as materials with a large low-temperature specific heat coefficient, γ, and correspondingly large Pauli susceptibility, χ. Both quantities are proportional to the quasi-particle density of states at the Fermi level which in turn, is related to an increased electronic effective mass several orders of magnitude larger than the electron mass. Generally it is believed that these very large mass enhancements result from strong electron-electron interactions. The overall behaviour can be characterized by a Wilson ratio, $R = \chi/\gamma$ of the order of unity, which indicates that both γ and χ are enhanced in a similar manner. Another interesting aspect of the heavy fermions is the emergence of superconductivity and, even more exciting the coexistence of magnetic order and superconductivity.

1.3.1 Kondo effect

In normal metals the electrical resistivity usually decreases at lower temperatures, since the lattice vibrations become small and the electrons tend to move freely in metal. Nevertheless, at the lowest temperatures the resistivity saturates due to static defects in the material. However, small concentrations of magnetic impurities drastically change this behaviour. As the temperature drops, the resistivity first decreases showing a minimum but then tends to increase upon further cooling rather then simply saturating. Magnetic impurities are usually atoms with partially filled d or f-shells, generally having more then one orbital available. It turned out that the resistivity minimum phenomenon is strongly correlated with the presence of the localized magnetic moments in the system. The question of how the presence of magnetic impurities affects the low-temperature properties of a system remained unanswered for a long time. In 1964 Kondo [17] gave the first explanation to this behaviour using a second-order perturbation-type calculation of the $s-d$ exchange model. The perturbed hamiltonian of this model is given by the following expression:

$$\begin{aligned} H_{s-d} = \sum_{kk\prime} J_{kk\prime}[S^{+}c^{+}_{k,\downarrow}c_{k\prime,\uparrow} \quad &+ \quad S^{-}c^{+}_{k,\uparrow}c_{k\prime,\downarrow} + \\ &S_z(c^{+}_{k,\uparrow}c_{k\prime,\downarrow} - c^{+}_{k,\downarrow}c_{k\prime,\uparrow})], \end{aligned} \tag{1.2}$$

where J denotes the coupling constant and $S^{\pm} = S_x \pm iS_y$ and S_z are the spin operators for a state of spin S. This is the simplest approach, which considers the interaction between a single localized spin and the spins of the conduction electrons. Usually, the resistivity due to simple impurities is calculated in a first-order approximation and, indeed, a temperature independent term is obtained. However, a temperature dependent term appears in a second-order calculation. Kondo has shown that the temperature dependence of the electrical resistivity is given by:

$$\rho_{imp.} = \frac{3\pi m J^2 S(S+1)}{2e^2\hbar\epsilon_F}\left[1 - 4J\rho_0(\epsilon_F) ln\frac{k_B T}{D}\right], \tag{1.3}$$

where D is the bandwidth. To explain the minimum of the resistivity as a function of temperature, J must be negative, *i.e.* antiferromagnetic exchange coupling. The expression shows that the resistivity increases logarithmically when the temperature is lowered and, thus, explains the minimum observed at low-temperature. The resistivity minimum is now called the Kondo effect and the temperature at which the resistivity starts to increase defines the so-called "Kondo temperature". The Kondo model gives a qualitative interpretation of the resistivity behaviour. However, this model makes the unphysical prediction that the resistivity should diverge as the temperature approaches zero.

The challenge to find a solution for the Kondo problem led to an enormous amount of activity [18]. An important contribution to understanding the physics of this problem was developed by Anderson and co-workers [19, 20]. Later Wilson [21] found the solution to this problem using a "numerical renormalization group technique" for an $S = 1/2$ classical exchange hamiltonian. He showed numerically that the exact solution at $T = 0$ for the Kondo problem consists of a non-magnetic singlet formed by an antiferromagnetic exchange coupling between the impurity spin and the conduction electron spin. This leads to a non-magnetic solution and the low-temperature properties were found to be those of a Fermi liquid. The exact analytical solution of the Kondo problem has been found by Andrei [22] and Wiegmann [23] using Bethe ansatz methods for both the classical exchange $s-d$ hamiltonian and the N fold degenerate model, Coqblin-Schrieffer hamiltonian. The renormalization group and Bethe ansatz solutions have led to a complete picture of the ground state and thermodynamic behaviour for the Kondo problem.

As mentioned above, the exchange $s-d$ model deals with a single impurity problem. This idea was generalized for a lattice which has a magnetic impurity on every site, the so-called Kondo lattice [18].

1.3.2 Interactions

In general the conduction electrons are responsible for magnetism in metals. However, the cases of transition metals and rare earth metals are different. In transition metals the $3d$-electrons are responsible for the magnetic moment and the exchange interaction. In rare earth metals on the other hand the magnetic moment is due to f-electrons and the exchange interaction is due to the s, p and d conduction electrons. Exchange interaction or direct exchange arises from direct Coulomb interaction between localized electrons whose orbitals are centered on different sites. The f-electrons that determine magnetic properties are strongly localized so that there is no significant overlap and hence, no direct exchange interaction can occur. In fact, in the f-electron systems the f-orbital is much smaller than the interatomic distances which results in a negligible exchange interaction between the f-electrons of different atoms.

To explain the magnetism in these systems the so-called indirect exchange mechanism, known as a Ruderman-Kittel-Kasuya-Yoshida (RKKY) interaction is used. The magnetic order in rare earth metals emerges through the indirect exchange interaction, in which the interaction between two ions is mediated by conduction electrons. The main idea is that a spin localized on a certain atom interacts with conduction electrons leading to a spin polarization. The spin polarization then interacts with a spin localized on another atom and mediates the indirect exchange interaction between the localized spins. The resulting magnetic ordering can either be ferromagnetic or antiferromagnetic depending on the band structure filling. In general, the RKKY interaction leads to ferromagnetism for a less then half filed band and to antiferromagnetism for half filled band.

Another way for localized spins to interact is through the superexchange interaction, in which the mediator is a neutral atom situated between the magnetic ions.

1.3.3 Energy scale

Heavy fermion behaviour requires the presence of a low-energy scale in the system. Usually, that energy scale is characterized by a characteristic temperature, T_{coh}, called the coherence temperature. Below T_{coh}, coherent quasi-particles with large effective masses develop. One can roughly identify T_{coh} as a temperature below which the coherent scattering between magnetic sites emerges [24]. When the temperature increases, the quasi-particles loose their heavy mass character. For a long time it was believed that the Kondo effect, which involves the formation of a singlet ground state due to weak hybridization of the $4f$-electrons with the conduction electrons, is the mechanism responsible for heavy fermion behaviour [18, 25, 26, 27]. However, recently it has been found that heavy quasi-particles may have rather different origin than the Kondo effect, like Zeeman splitting of the f-states for example [28]. Therefore, instead of having one mechanism responsible for the occurrence of heavy electron behaviour there may exist a variety of effects. What is common in all cases is that the $4f$ or $5f$-electrons are involved and the spin degrees of freedom seem to have important contribution.

1.3.4 The Doniach picture

Magnetic order in heavy fermions has proved difficult to explain in quantitative terms. It is relevant that in some rare earth metals a heavy electron state may develop within a magnetically ordered metal. In such systems the ground state results from a competition (or coexistence) between two main interactions: i) the itinerant RKKY interaction which gives rise to a magnetic interaction between different rare-earth atoms and ii) the Kondo interaction between local moments and the conduction electrons, which on the contrary favours a non-magnetic ground state. Both interactions arise from the same exchange coupling energy, J. This coupling has a characteristic temperature, which is given by $T_{RKKY} \propto J^2 N(E_F)/k_B$ for the RKKY interaction and by $T_K \propto N(E_F)^{-1} exp\left[-1/N(E_F)J\right]$ for the Kondo interaction. Here $N(E_F)$ is the density of states at the Fermi energy. It is believed that the competition between the RKKY and Kondo interaction gives rise to heavy fermion behaviour. This competition leads to a rich phase diagram, the so-called "Doniach diagram" [29]. Figure 1.5 displays the dependence of the magnetic ordering temperature, T_{RKKY}, and the Kondo temperature, T_K, as a function of the exchange parameter times the density of states of the conduction band at the Fermi energy, $|J|\, N(\epsilon_F)$. Notice that the two curves cross and for a large values of $|J|\, N(\epsilon_F)$ the Kondo temperature is always larger then T_{RKKY}, thus the Kondo effect dominates in this limit. The magnetic moments are strongly screened and a singlet ground state is formed below T_K, so that no magnetic order is expected. For a small value of $|J|\, N(\epsilon_F)$ the ordering temperature is much larger then T_K, yielding an antiferromagnetic order, in most cases. Of particular interest is the intermediate region, where the RKKY and Kondo characteristic temperatures become comparable. As a result the magnetic structure can be complicated. We observe that the ordering temperature of a real system (see the red area in figure 1.5) follows T_{RKKY} while $|J|\, N(\epsilon_F)$ is small, but then exhibits a global maximum and goes to zero at a critical value of $|J|\, N(\epsilon_F)$ corresponding to a quantum critical point (QCP) between the Kondo singlet and RKKY magnetic ground states. This can leave the system in the proximity of a zero temperature magnetic phase transition, or quantum phase transition, which is one of the scenarios believed to give rise to so-called non-Fermi liquid behaviour. Such a trend has been observed in pressure measurements in many heavy electron antiferrromagnets [30, 31]. In some measurements the maximum was not observed, but the ordering temperature clearly decreased with a rising of pressure and eventually vanished. With some extensions, this diagram describes the experimental observations in cerium and ytterbium compounds, well.

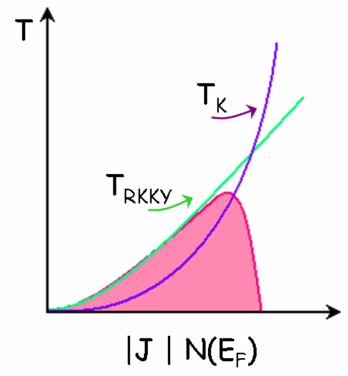

Figure 1.5: Doniach phase diagram. - Schematic illustration of the temperature versus exchange parameter,J, times the density of states, $N(\epsilon_F)$. The characteristic temperatures T_{RKKY} and T_K are indicated by green and violet lines, respectively. The pink area represents the temperature of the magnetic transition.

However, some uranium compounds exhibit quite different behaviour from cerium compounds, due to the coexistence of competing phenomena such as: magnetism and the Kondo effect, or more excitingly, the coexistence of magnetism and superconductivity. We will focus on the coexistence of magnetic order and Kondo behaviour, experimentally reported, for example, in $\mathrm{UNiSi_2}$ [32] and $\mathrm{UCo_{0.5}Sb_3}$ [33]. It is specific to these compounds that they order ferromagneticaly at a relatively high-temperature ($T_C \sim 100$ K) while the Kondo behaviour is observed above T_C, and survives in the ferromagnetic state. This implies that the magnetic order and the Kondo behaviour coexist rather than compete. These are unusual features, which cannot be explained by the phase diagram described above. A similar kind of coexistence of ferromagnetism and Kondo behaviour has also been observed in several cerium compounds. However, the Curie temperature in these cases remains low (of order 5 K), which is considered a sign of competition between the two phenomena. To account for the coexistence of ferromagnetism and the Kondo effect a "ferromagnetic Doniach diagram" was proposed in Ref. [34].

1.3.5 Periodic Anderson model

As has been mentioned above there is no completely accepted theory up to now to describe heavy fermion metals. It is generally believed that the periodic Anderson model (PAM), which describes the hybridization of localized orbitals with a conduction band, captures the main physics of heavy fermions. This model is defined by the following hamiltonian:

$$\begin{aligned} H = \sum_{k\sigma} \epsilon_k c^+_{k\sigma} c_{k\sigma} + \epsilon_f \sum_{i\sigma} f^+_{i\sigma} f_{i\sigma} V (\sum_{k,i\sigma} c^+_{k\sigma} f_{i\sigma} \quad + \quad f^+_{i\sigma} c_{k\sigma}) + \\ U \sum_i n^{\uparrow}_{fi} n^{\downarrow}_{fi}. \end{aligned} \tag{1.4}$$

The first term in Eq. 1.4 describes a wide conduction band with dispersion ϵ_k, the second corresponds to a narrow f-band of energy ϵ_f and the third to their hybridization. The last term describes the on-site Coulomb repulsion of f-electrons. Since this model cannot be solved exactly various approximations have been proposed in order to reproduce the experimental observations. We will consider a simplified approach based on perturbation theory in U [18], where the general solution of the Hamiltonian is given by two renormalized quasi-particle bands with energies:

$$E^{\pm}_k = \frac{1}{2}\left[\epsilon_F + \epsilon_k + \tilde{\epsilon}_{f,k} \pm \sqrt{(\epsilon_F + \tilde{\epsilon}_{f,k} - \epsilon_k)^2 + 4\left|\tilde{V}_k\right|^2}\right], \tag{1.5}$$

where ϵ_F is the Fermi level. These are the same bands as in the non-interacting case, $U = 0$, except that the bare energies $\epsilon_{f,k}$ and V_k are replaced with renormalized parameters $\tilde{\epsilon}_{f,k}$ and $\tilde{V}_k$.

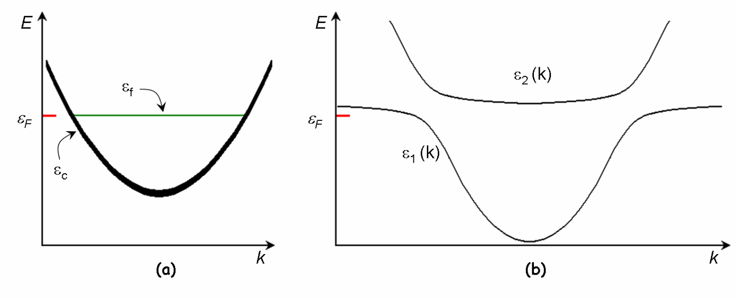

Figure 1.6: Schematic PAM band structure. - Energy dispersion of the conduction, ϵ_c, and f-electrons, ϵ_f. The Fermi energy is indicated by a red line. (a) The case where $V = 0$. (b) The limit where $V \neq 0$. $\epsilon_1(k)$ and $\epsilon_2(k)$ denote the renormalized quasi-particle bands.

These dispersion relations, schematically illustrated in figure 1.6(b), provide a simple picture, in which many aspects of the low-energy physics of heavy fermion systems can be visualized. In a system with no hybridization ($V = 0$) the f-electrons are localized and uncoupled from the conduction electrons which simply leads to an independent particle picture sketched in figure 1.6(a). Switching on the hybridization and the on-site Coulomb repulsion leads to fundamental departure from this independent particle picture, in which the eigenstates become a mixture of both f- and conduction-electron character. The obtained ground state depends on the position of the Fermi level, which results from filling. For a metallic state the Fermi level lies in the partially filled lower band.

The effective mass of quasi-particle excitations is a function of the band curvature. Generally the large effective mass of heavy fermions is explained by the presence at E_F of the nearly flat part of the hybridized bands [see figure 1.6(b)]. As will be shown later, this model can qualitatively explain the mass enhancement observed in many compounds studied in this thesis.

Chapter 2

Some aspects of optical spectroscopy

In this chapter we give a short review of some basic concepts of optical spectroscopy. We shall briefly discuss the interaction of electromagnetic radiation with matter, further we shall present the measurement techniques of optical experiments, ellipsometry and reflectivity, used to study optical properties of materials. Their mutual complementarity allows the extraction of optical quantities, such as the dielectric function and the optical conductivity, over a broad frequency range. In addition, we describe in detail the data analysis procedure. Finally, we discuss the interpretation of the complex dielectric function in terms of absorption process in solids.

2.1 Electromagnetic response of a solid

The macroscopic interaction of electromagnetic radiation with matter is expressed by the well-known Maxwell equations [35, 36, 37]. In order to describe the behaviour of matter under the influence of a field we have to consider the electric dipoles, magnetic moments, polarization charges and induced currents. Thus, additional relations are introduced to account for the material properties, where the electric field strength, E, is connected with the electric displacement, D, through expression $D = \epsilon E = E + 4\pi P$ and in a similar way the magnetic induction, B, is related to the magnetic field strength, H, by $B = \mu H = H + 4\pi M$. The other parameters are the dielectric function, ϵ, the polarization, P, the magnetic permeability, μ, and the magnetization, M.

Therefore the macroscopic Maxwell's equations are written as:

$$\begin{aligned} \nabla \times E(r,t) &= -\frac{1}{c}\frac{\partial B(r,t)}{\partial t}, \quad \nabla \cdot B(r,t) = 0, \qquad (2.1) \\ \nabla \times H(r,t) - \frac{1}{c}\frac{\partial D(r,t)}{\partial t} &= \frac{4\pi}{c} J_{cond}(r,t), \quad \nabla \cdot D(r,t) = 4\pi \rho_{ext}(r,t), \end{aligned}$$

where c is the velocity of light, J_{cond} and ρ_{ext} are the current and external charge densities. If we separate the total charge and current densities into bound and free contributions considering the effects of polarization and magnetization then the total charge and current density are expressed as: $\rho_{tot} = \rho_{ext} + \rho_{ind}$ with $\rho_{ind} = -\nabla P$ and $J_{tot} = J_{ext} + J_{ind}$ with $J_{ind} = J_{cond} + J_{bound}$ and $J_{bound} = \partial P/\partial t + c\nabla \times M$. Substituting these terms into Maxwell's Eq. 2.1 we obtain:

$$\begin{aligned} \nabla \cdot E(r,t) &= 4\pi \left\{ \rho_{ext}(r,t) - \nabla \cdot P(r,t) \right\}, \qquad (2.2) \\ \nabla \times B(r,t) - \frac{1}{c}\frac{\partial E(r,t)}{\partial t} &= \frac{4\pi}{c} \left\{ J_{cond}(r,t) + \frac{\partial P(r,t)}{\partial t} + c\nabla \times M(r,t) \right\}. \end{aligned}$$

Thus far these relations consider a linear response in the applied fields, which assumes that the applied fields are sufficiently small. Therefore, we can consider that the induced electrical currents are linearly proportional to the applied fields. If the fields are exceptionally strong such as, for example, the ones generated by a pulsed laser, the response of polarization and magnetization must be completed by terms involving components of the field vectors in higher power leading to a nonlinear response.

Eq. 2.3 can take a simplified form if we represent all the fields as a Fourier sum of plane waves, for example $E(q,\omega) = \frac{1}{(2\pi)^4} \int dr \int_{-\infty}^{\infty} E(r,t) e^{i(-qr+\omega t)} dt$. As our attention is focused on light propagating inside a solid, the external charge densities vanish. After some manipulations [35, 36] the transverse and longitudinal parts of fields and currents densities are:

$$\begin{aligned} J^T_{ind}(q,\omega) &= \frac{-ic^2\omega}{4\pi\omega} \left\{ q^2 \left(1 - \frac{1}{\mu} \right) - \frac{\omega^2}{c^2}(1 - \epsilon^T) \right\} E^T(q,\omega), \qquad (2.3) \\ J^L_{ind}(q,\omega) &= \frac{i\omega}{4\pi}(1 - \epsilon^L) E^L_{total}(q,\omega), \qquad (2.4) \end{aligned}$$

where ϵ^T and ϵ^T are the transverse and longitudinal dielectric function tensors, respectively. It is worthwhile to mention that these relations refer to isotropic and homogeneous media where the eigenstates of the Maxwell equations are either completely longitudinal or completely transverse. In the long-wavelength limit ($q \rightarrow 0$) $\epsilon^L(0,\omega)$ and $\epsilon^T(0,\omega)$ are identical. Using Ohm's law, $J = \sigma_1 E$, we now define the optical conductivity tensor, $\sigma(\omega) = \sigma_1(\omega) + i\sigma_2(\omega)$, as:

$$\sigma(\omega) = -\frac{i\omega}{4\pi}\left[\epsilon(\omega) - 1\right]. \tag{2.5}$$

This relation is particularly important because it relates the optical conductivity and the dielectric function, which is an experimental quantity. Theoretically, one usually calculates the charge's response to electrical fields and, hence, estimates conductivities, while experimentally one measures the dielectric functions rather than conductivities. Therefore, the connection between these quantities, expressed in Eq. 2.5 constitutes an important link between theory and experiment.

2.2 Kramers-Kronig transformation and sum rules

The response of a system to an external force is characterized by a response function. The real and imaginary parts of the response function are not independent quantities but related via the Kramers-Kronig (KK) relation [35, 36, 37]. This transformation is very general and can be applied to various kinds of response functions such as the dielectric constant, conductivity or susceptibility. The linear response, $X(r,t)$, of a system at location r and time t to an external perturbation, $f(r't')$, at some different position r' and time t' is described by the response function $G(r,r',t,t')$:

$$X(r,t) = \int\int_{-\infty}^{\infty} G(r,r',t,t')f(r't')dr'dt'. \tag{2.6}$$

If we assume that only the excitation at the same place leads to a response then $G(r,r',t,t') = \delta(r-r')G(t-t')$. If we add an additional requirement that only the excitations at a time $t > t'$ can take place, which is simply the causality principle, that is the effect can not precede the cause, and implies that $G(t-t')$ = 0 for $t < t'$. The simplified response function is given by:

$$X(t) = \int_{-\infty}^{\infty} G(t-t')f(t')dt'. \tag{2.7}$$

Using the space of Fourier transform variables for each of these functions, for example for the response function $G(\omega) = \int G(t-t')exp\left[i\omega(t-t')\right]dt$, and using the Cauchy's theorem we can show that:

$$ReG(\omega) = \frac{1}{\pi}P\int_{-\infty}^{\infty}\frac{ImG(\omega^{'})}{\omega^{'}-\omega}d\omega^{'}, \tag{2.8}$$

$$ImG(\omega) = -\frac{1}{\pi}P\int_{-\infty}^{\infty}\frac{ReG(\omega^{'})}{\omega^{'}-\omega}d\omega^{'}, \tag{2.9}$$

here P denotes the principal value. With this general transformation we can obtain relations connecting the real and imaginary parts of various response functions [35, 36]. The Kramers-Kronig relation for the real, $\epsilon_1(\omega)$, and imaginary, $\epsilon_2(\omega)$, parts of the complex dielectric function is:

$$\epsilon_1(\omega) - 1 = \frac{2}{\pi}P\int_{0}^{\infty}\frac{\omega^{'}\epsilon_2(\omega^{'})}{\omega^{'2}-\omega^2}d\omega^{'}, \tag{2.10}$$

$$\epsilon_2(\omega) = \frac{4\pi\sigma_{dc}}{\omega} - \frac{2\omega}{\pi}P\int_{0}^{\infty}\frac{\epsilon_1(\omega^{'})}{\omega^{'2}-\omega^2}d\omega^{'}, \tag{2.11}$$

where σ_{dc} denotes the dc conductivity. This transformation has an important application in optics because it means that measurement of the imaginary part of the dielectric function can be used to find the real part and vice versa. The main limitation of this transformation is the requirement of having measured data over a large frequency range. As will be shown in the next chapters we use more then one technique in order to cover a broad spectral range.

There are other properties of the dielectric function, for example the sum rules [35, 36], which are often used in the analysis of absorption spectra. They may be written in terms of the dielectric function or the optical conductivity. The most common is the f-sum rule that expresses charge conservation in a system:

$$\int_{0}^{\infty}\sigma_1(\omega')d\omega' = \frac{\pi ne^2}{2m} = \frac{\omega_{pl}^2}{8}, \tag{2.12}$$

where $\sigma_1(\omega)$ is the real part of the optical conductivity, n is the electron density and m is the electron mass. However, Eq. 2.12 requires integration from zero to infinity, while experimental data are available only in a limited frequency range. Therefore, the *partial* optical sum rule is introduced as:

$$\int_{0}^{\omega_c}\sigma_1(\omega')d\omega' = \frac{\pi ne^2}{2m_b}, \tag{2.13}$$

with m_b the bandmass. This finite integration limit represents the effective number of carries that contribute to the optical absorption process up to a certain frequency ω_c. Generally, the energy cutoff, ω_c, should be of the order of the plasma frequency edge, ω^*_{pl}, which is much smaller then the onset energy of interband transitions. This sum rule, which will be used in the next chapters, is particularly helpful in determining the plasma frequency and for studying the spectral weight transfer.

2.3 Electronic transitions

Optical properties of materials are determined by optical absorption processes. By analysing the dielectric response of materials as a function of frequency it is possible to obtain information about their electronic structure.

Optical transitions are induced by the electromagnetic field between different electronic states which are described by a set of bands. Therefore, in describing optical processes we have to distinguish between the interband and intraband transitions [35, 36]. Typical optical transitions are illustrated in figure 2.1. The letters A and B refer to interband transitions and letter C refers to intraband transitions. An interband transition occurs when an electron from the initial state is excited to an empty state in the next higher band, while the electron’s crystal momentum remains unchanged. Other possible transitions may also occur such that the crystal momentum of the electron changes as well. They are called indirect transitions and are illustrated in figure 2.1 by a blue arrow. One possible mechanism for these indirect transitions is provided by the electron-phonon interaction. The change in momentum of the electron can be removed by a phonon which is absorbed or emitted in the transition process. Quite intuitively, the interband contribution to the optical spectra starts at a finite onset energy. Any interband transitions will be directly reflected in the imaginary part of the dielectric function, which smoothly increases near the onset energy of absorption. The phenomenon responsible for interband transitions is described by the Lorentz model [35, 36]. In this case the dielectric function can be written as a superposition of a high frequency dielectric constant, ϵ_∞, and one or more Lorentz oscillators as:

$$\epsilon(\omega) = \epsilon_\infty + \sum_{i=1}^{N} \frac{\omega_{p,i}^2}{\omega_{0,i}^2 - \omega^2 - i\omega\gamma_i}, \tag{2.14}$$

where $\omega_{0,i}$ is the oscillator frequency, $\omega_{p,i}$ is the plasma frequency and γ_i is the scattering rate.

Intraband absorption occurs in a metal when an electron is excited from a state below the Fermi energy to another state above the Fermi energy within

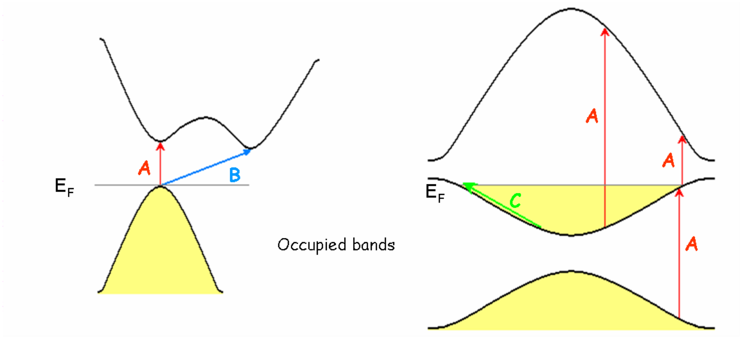

Figure 2.1: Schematic illustration of the possible types of electronic transitions. - Left sketch illustrates the optical transitions in a semiconductor or insulator while the right sketch addresses optical transitions in a metal. The letters A and B denote interband transitions and the letter C denotes intraband transition as described in the text.

the same band. While interband transitions have an onset energy, the intraband transitions occur over a continuous wide range of energies starting from zero. Such transitions are responsible for the infrared absorption and high reflectivity in the low-frequency range. The high reflectivity of metals is due to a partially filled conduction band which allows photons to be absorbed and reflected over a large frequency range, forming a continuum of energy from the far-infrared up to ultra violet. At high frequency an energy is reached beyond which the reflection and absorption usually decrease due to an inability to excite electrons just above the top of the conduction band. The intraband contribution to the optical conductivity is usually described by the Drude model:

$$\sigma(\omega) = \sigma_{dc}/(1 + (\omega\tau)^2). \tag{2.15}$$

In which the dc conductivity, σ_{dc}, is proportional to the relaxation time, τ.

2.4 Experimental techniques and analysis

Optical spectroscopy is one of the most powerful tools for investigating the electrodynamic response of a solid, which has enormous importance in material science and condensed matter physics. The study of the optical properties usually yields information concerning the electronic band structure as well as electron-electron interactions in solids.

In the present study two experimental techniques, reflectivity and ellipsometry were used in order to measure the optical quantities.

2.4.1 Spectroscopic ellipsometry

Ellipsometry is a powerful optical technique of great sensitivity, particularly appreciated for the non destructive characterization of surface phenomenon, for the optical characterization of materials. Ellipsometry measures the changes in the polarization state of light when it is reflected from, or transmitted through, a material. When linearly polarized light is reflected at oblique incidence from a surface then the reflected beam is elliptically polarized. The nature of the ellipticity reveals the optical properties of the material. This technique is widely used to determine the optical quantities for bulk and thin film materials, the band gap and electronic transitions, the film's thickness and the surface roughness. The main advantages of this technique are that it gives phase information and that it is self-normalizing. Thus it avoids problems related to normalization that can occur in conventional reflectivity measurements.

The typical geometry of ellipsometic technique is schematically illustrated in figure 2.2. The ellipsometry experiment determines the complex ratio of the two reflection coefficients for light with polarization parallel, r_p, and perpendicular, r_s, to the plane of reflection:

$$\rho = |r_p/r_s| = tan(\Psi)e^{i\Delta}, \tag{2.16}$$

where Ψ represents the relative amplitude of the two polarizations while Δ represents the relative phase difference. The reflection coefficients r_p and r_s are given by Fresnel formulas:

$$r_p^{\nu} = \frac{E_{r,p}}{E_{i,p}} = \frac{\sqrt{1-\varepsilon_z^{-1}\sin^2\theta} - \sqrt{\varepsilon_x}\cos\theta}{\sqrt{1-\varepsilon_z^{-1}\sin^2\theta} + \sqrt{\varepsilon_x}\cos\theta}, \tag{2.17}$$

$$r_s^{\nu} = \frac{E_{r,s}}{E_{i,s}} = \frac{\cos\theta - \sqrt{\varepsilon_y - \sin^2\theta}}{\cos\theta + \sqrt{\varepsilon_y - \sin^2\theta}}, \tag{2.18}$$

where $\epsilon_\nu = \epsilon_{1\nu} + i\epsilon_{2\nu}$ (ν = x, y, z) are the components of the complex dielectric tensor and θ is the angle of incidence. The reflection coefficients are complex numbers containing reflection amplitudes and phase shifts caused by reflection. The optical response is completely described by the complex dielectric response.

Furthermore, the complex pseudo-dielectric function can be obtained from the numerical inversion of the Fresnel equations:

$$\epsilon_{pseudo} = sin^2\theta\left[1 + tan^2\theta\left(\frac{1-\rho}{1+\rho}\right)^2\right]. \tag{2.19}$$

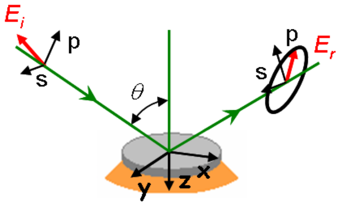

Figure 2.2: Schematic illustration of the ellipsomety technique. - E_i denotes the incident linear polarized light and E_r the reflected elliptically polarized light. The directly measured relative amplitude and phase difference allow reconstructing the dielectric function, $\epsilon(\omega) = \epsilon_1(\omega) + i\epsilon_2(\omega)$.

In general the term ρ depends on the orientation of the sample. Hence to get the complete dielectric function, additional measurements along different crystal axes or with different angles of incidence are required. For isotropic materials the situation is much simpler, because the pseudo-dielectric function is actually the true dielectric function and ρ has the same value for any orientation.

As mentioned above, ellipsometry is a surface sensitive technique. Some materials have very reactive surfaces and special care has to be taken during the surface preparation and measurements. When we measure such materials, we must take into account that spectra may be substantially affected by extrinsic surface properties (oxidized surface, different surface compositions etc.).

2.4.2 Near-normal incidence reflectivity

Near-normal incidence reflectivity is a technique that is widely used in optical spectroscopy. This technique is robust and accurate. Experimentally, reflectivity is the simplest optical property to measure.

Near-normal incidence reflectivity measurements (10° in our experiments) consist of impinging a light beam on a sample and measuring the intensity of the reflected beam (see figure 2.3). The absolute value of the reflectivity is obtained by calibrating the instrument using a gold layer deposited *in situ* on the sample surface, without breaking the vacuum and without moving the sample. This calibration procedure is designed to fully compensate for the frequency dependence of the instrument and the geometry of the sample. Problems of inaccuracy may appear for highly reflective sample, where the measured reflectivity is very close to unity.

From measured intensities of the light reflected from the sample, $I_s(\omega)$, and from the reference, $I_{ref}(\omega)$, it is possible to calculate the reflection coefficient as:

$$R(\omega) \equiv \frac{I_s(\omega)}{I_{ref}(\omega)}. \tag{2.20}$$

It has to be kept in mind that the measured reflectivity does not contain phase information.

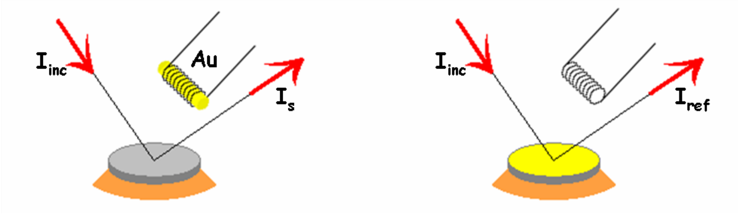

Figure 2.3: Schematic illustration of the reflectivity technique. - Left sketch shows the measurement on sample surface while right one the measurement on reference as described in the text.

2.4.3 Data analysis procedure

As mentioned above the optical measurements presented in this thesis were performed using near-normal incident optical reflectivity in combination with spectroscopic ellipsometry. The employed instruments are listed in Table 2.1. The near-normal incidence reflectivity, $R(\omega)$, was measured in the far- and mid-infrared spectral ranges using two infrared Fourier transform spectrometers, a Bruker IFS 66/v and a Bruker 113. They cover the frequency range from 6 meV to 0.7 eV. Different light sources, beamsplitters, polarizers and detectors with large spectral overlaps were combined for the reflectivity experiments. The high frequency spectra were collected using a Woollam VASE32 ellipsometer. In order to measure the temperature dependence we used continuous-flow liquid He cryostats. Generally the data between different spectral regions show a small mismatch of about $1-2\%$. Such a mismatch is, in particular, observed between the far- and mid-infrared spectral ranges for very highly reflecting sample. This could be because the reference used to normalize the reflectivity may not be perfect. To correct for this error, and to produce smooth spectra, the far-infrared data are scaled to the mid-infrared with the same factor used at all temperatures.

There are different ways to extract optical quantities from the experimentally measured quantities. Kramers-Kronig analysis of the normal incidence reflectivity is the most widely used technique for this purpose. However, specific problems arise, because this procedure requires integration over frequency from zero to infinity, while experimental data are available in a limited frequency range. Therefore, extrapolations to low and high frequencies are used. This procedure can be questionable because different data extrapolations, when applying the Kramers-Kronig transformation, can lead to artificial features in the conductivity spectra. Very highly reflecting samples are particularly sensitive to the extrapolations used.

Table 2.1: Summary of the optical components used for measurements*.

Frequency	6.2 meV - 0.07 eV	0.06 eV - 0.7 eV	0.1 eV - 1 eV
Lightsourse	Mercury lamp	Globar lamp	
Beamsplitter	6μMultilayer	KBr	
Detector	4.2 K bolometer	DTGS	MCT
Polarizers	gold grid	KRS5	

---

*KBr- potassium bromide, DTGS- deuterated triglycine sulfate, MCT- mercury cadmium telluride, KRS5-thallium bromide and iodide mixed crystals.

In this work, the applied procedure is different from the usual one. Instead of applying the KK relation directly to the reflectivity, we fit the reflectivity with a KK-constrained variational dielectric function. The main advantage of this method is that knowledge of the reflectivity data in the whole spectral range is no longer required. While the dielectric function, $\epsilon(\omega) = \epsilon_1(\omega) + i\epsilon_2(\omega)$, in our experiments is measured directly at high frequencies, at low frequencies we applied a variational Kramers-Kronig constrained analysis of the data. In this approach, described in detail in Ref. [38], one finds a KK-consistent dielectric function, that gives the best detailed match to the reflectivity, $R(\omega)$, at low frequencies and both $\epsilon_1(\omega)$ and $\epsilon_2(\omega)$ at high frequencies simultaneously. For illustration of the data analysis we give the example shown in figure 2.4 without giving further detail of the observed structures and their interpretation. The experimentally determined $\epsilon_1(\omega)$ and $\epsilon_2(\omega)$ of CoSi are displayed in the figure together with the reflectivity data. For fitting the optical spectra the RefFIT software [38] was used.

The fitting routine consists of two main steps. In the first step the experimental data (in our case it is $R(\omega)$ at low frequencies and both $\epsilon_1(\omega)$ and $\epsilon_2(\omega)$ at high frequencies) are fitted with a Drude-Lorentz model that defines a limited set of oscillators. Each oscillator is characterized by adjustable parameters: $\omega_{0,i}$, $\omega_{p,i}$, γ_i that define the oscillator frequency, plasma frequency and linewidth, respectively, and a contribution from all oscillators at very high frequency, ϵ_∞. The parameters can be adjusted in order to get a good match between the model-generated data and the experiment. An acceptable fit describ-

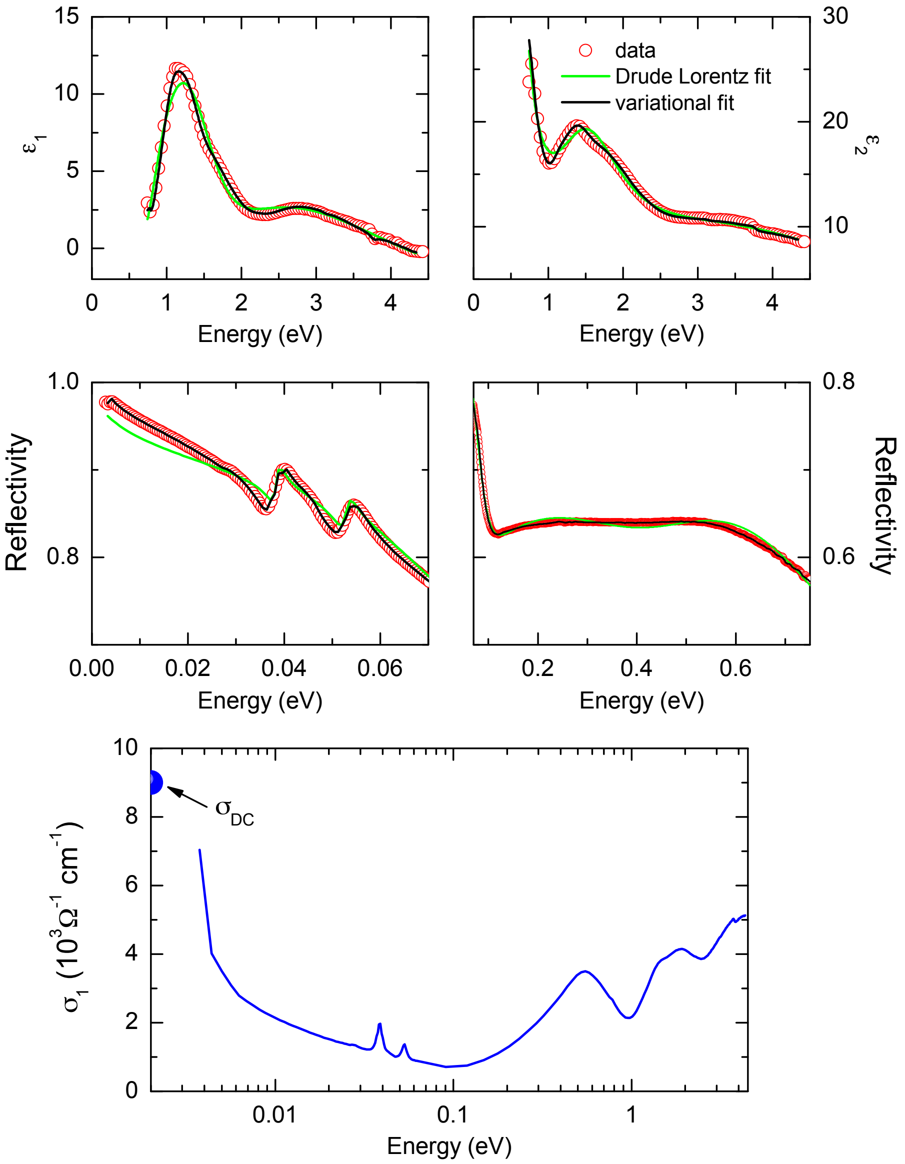

Figure 2.4: Room temperature experimental data for real, $\epsilon_1(\omega)$, and imaginary, $\epsilon_2(\omega)$, parts of the dielectric function and reflectivity data with model curves for CoSi. - The green and black lines show the Drude-Lorentz model and the variational fitting, respectively. Also represented in this figure is the obtained optical conductivity including the independently measured dc conductivity.

ing the major features can be obtained, for example, by using a least-square fitting method. Generally the number of oscillators must be much lower then the number of data points. The obtained spectra are rather smooth, however, depending on details of the spectra, some important information can be lost. The fit curves are shown in figure 2.4 by green lines. We see that this model does not fit perfectly the experimental data, especially in the low-frequency region, but, as a first approximation, it is acceptable.

In the second step a variational fitting is performed in order to take into account the fine structure of the spectra. The idea is to put a KK-constrained variational dielectric function on top of the Drude-Lorentz model and perform the final fitting. This procedure allows one to anchor the phase of the complex reflectivity at low frequencies by the ellipsometrically measured real and imaginary parts of the dielectric function at high frequencies. This technique is thus more accurate then the usual KK transformation.

Finally, by deriving the real and imaginary parts of the dielectric function from the spectra over a broad frequency range many other significant frequency dependent optical quantities such as the complex conductivity, $\sigma(\omega)$, can be extracted:

$$\sigma(\omega) = \frac{\omega\epsilon_2(\omega)}{4\pi} + i\frac{\omega}{4\pi}[1 - \epsilon_1(\omega)]. \tag{2.21}$$

Chapter 3

Optical spectroscopy of FeGe

In this chapter we present the optical spectrum of the cubic helimagnetic metal FeGe that has been investigated in the frequency range from 15 meV to 3.1 eV for temperatures between 30 K and 296 K. The optical conductivity shows the evolution of a low-energy (0.22 eV) interband transition and the development of a narrow free carrier response, with a strong energy and temperature dependence. The frequency dependent effective mass and scattering rate, derived from the optical data, indicate the formation of dressed quasi-particles with a mass renormalization factor of 5. Similar to FeSi the spectral weight in FeGe is not recovered over a broad frequency range, an effect usually attributed to the influence of the on-site Coulomb interaction.

3.1 Introduction

Cubic FeGe is a good metal which undergoes a transition to helimagnetic order at T_C = 280 K with a saturated magnetic moment of $1\mu_B$ per Fe atom [39]. The helix, with a period of 700 Å, changes its orientation in a temperature interval ± 20 K and shows pronounced temperature hysteresis between 211 K and 245 K [1]. FeGe crystallizes in the B20 crystal structure and the cubic space group $P2_13$ with the unit cell containing four iron and four germanium atoms as shown in figure 3.1 (left panel), the lattice parameter being 4.7 Å. The crystal structure lacks a centre of inversion symmetry responsible for the modulation of the ferromagnetic structure.

This compound is iso-electronic and iso-structural with FeSi. FeSi has a large magnetic susceptibility at room temperature which vanishes as the temperature approaches zero due to a small (70 meV) semiconductor gap at E_F. A continuous series FeSi$_{1-x}$Ge$_x$ can be formed, where the metal insulator transition [2] occurs for $x \approx 0.25$ (see figure 3.1 right panel). Theoretical models which have been proposed to explain this behaviour, invoke disorder [40], narrow bands and different ways of incorporating electron correlations [41, 42, 43, 44]. The temperature dependent disappearance of the gap has been explained as a result of a correlation gap using a two-band Hubbard model [45, 46], and excellent agreement was obtained with optical data [47, 48, 46] but it has been shown that vibrational disorder, if sufficiently strong, also closes the gap [49].

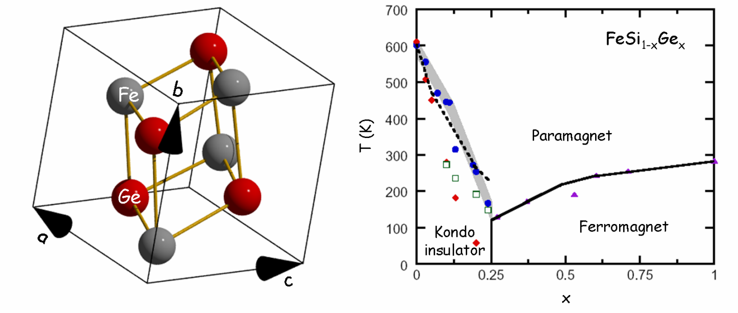

Figure 3.1: B20-type crystal structure of FeGe and the phase diagram of FeSi$_{1-x}$Ge$_x$. - Left panel: There are four Fe and four Ge ions in a unit cell of FeGe arranged in such way that every atom has seven nearest neighbours of the opposite kind. Gray and red spheres indicate the Fe and Ge atoms, respectively. Right panel: Temperature versus concentration phase diagram of FeSi$_{1-x}$Ge$_x$ from Ref. [2]. A first-order transition from the Kondo insulator phase to a ferromagnetic phase occurs at $x \approx 0.25$. For $x = 1$ the phase diagram corresponds to FeGe.

It turns out that FeGe is a rare case where external pressure can be used to tune the transition from a metallic to an insulating state [2, 50, 40]. However, so far the transport measurements [51] have shown that the metallic state persists up to 23 GPa. This suggests that higher pressure is needed in order to observe such transition.

Anisimov *et al.* [50] have predicted a magnetic field driven semiconductor to metal transition in FeSi$_{1-x}$Ge$_x$, and argue that the difference in electronic structure between FeSi and FeGe in essence consists of a rigid relative shift of the majority and minority spin bands for the latter material. According to this model the optical spectra at low energies is expected to be the superposition of a Drude peak and an interband transition across an energy range corresponding to the aforementioned relative shift of the majority and minority bands.

3.2 Thermodynamic and transport properties

Cubic FeGe single crystals were grown by a chemical vapour transport method as described in detail in Ref. [52]. According to this reference the following reaction has been proposed for the vapour transport reaction with chemical agent iodine:

$$FeGe_{(s)} + 2GeI_{4(g)} = FeI_{2(g)} + 3GeI_{2(g)}, \tag{3.1}$$

where the indices s and g indicate the solid and gas phases, respectively. To characterize the single crystals we measured the temperature dependence of the specific heat, resistivity and magnetization.

3.2.1 Specific Heat

The specific heat of FeGe was measured by an adiabatic calorimeter in the temperature interval from 10 to 300 K. The variation of the specific heat with temperature is displayed in figure 3.2 (left panel). The sharp peak that appears at T_C = 280 K is compatible with the first-order phase transition. We note that the phase transition into the helical state in FeGe is first-order. Also shown in this figure (right panel) is C/T versus T^2 at low-temperature. The low-temperature specific heat can be fitted to the expression $C(T)/T = \gamma + \beta T^2$ where γ and β are constants arising from charge carriers and lattice, respectively. The experimentally obtained specific heat coefficient is found to be 10.4 mJ mol^{-1}K^{-2}.

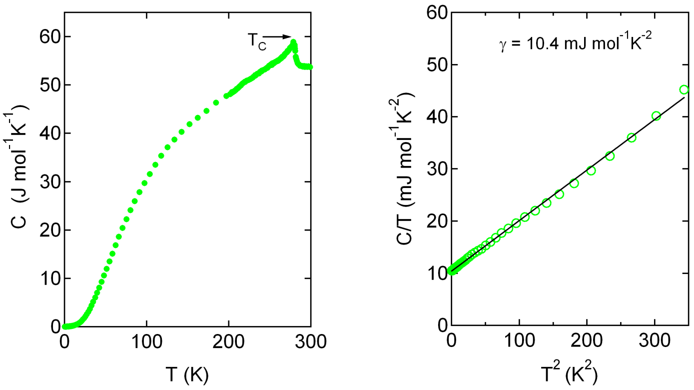

Figure 3.2: Specific heat of FeGe at zero magnetic field. - Left panel: C versus T dependence. The arrow indicates the Curie temperature. Right panel: C/T versus T^2 giving γ = 10.4 mJ mol^{-1} K^{-2}. The black line is the fit to the form $C(T)/T = \gamma + \beta T^2$.

The magnitude of γ is consistent with previous experiments [2]. The high-value of the specific heat coefficient suggests a relatively large electron effective mass.

In the case of FeGe the value of the specific heat coefficient is quite large compared to the value found in most transition metals [53]. In addition, this value is not too far from the value found in some heavy fermion materials [54, 55]. It is believed that the main difference between the transition metals and heavy fermions is that the latter are strongly correlated. Therefore the large value of the specific heat coefficient in FeGe suggests the presence of a strong interaction between the d-electrons and the development of heavy quasi-particles in the Fermi liquid state.

3.2.2 Resistivity

The resistivity measurements on FeGe single crystal were carried out by the four-point contact technique in the temperature range from 15 to 300 K. The temperature dependent electrical resistivity, $\rho(T)$, of FeGe is displayed in figure 3.3 (left panel). A metallic behaviour is observed above and below the Curie temperature in agreement with previously reported data. The resistivity increases with temperature and a small slope change is seen close to the transition temperature of 280 K. At low temperatures the resistivity fits to a simple T-square dependence $\rho(T) = \rho_0 + AT^2$ (see figure 3.3 right panel), which indicates a Fermi liquid behaviour. Here ρ_0 = 8.5 $\mu\Omega$ cm is the residual resistivity from the electron impurity scattering. The small upturn seen below 10 K probably comes from the contribution due to impurities or defects.

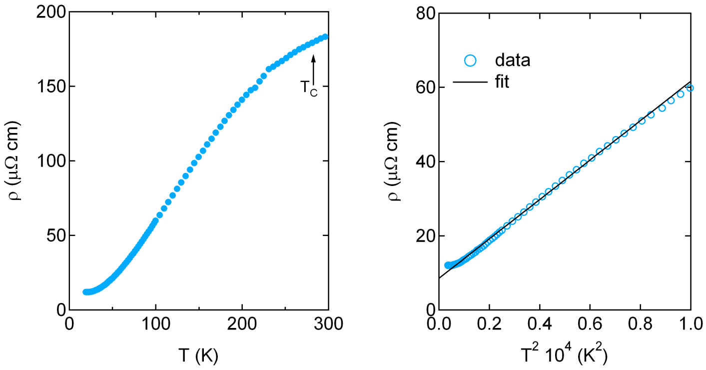

Figure 3.3: Temperature dependent resistivity of FeGe. - Left panel: $\rho(T)$ versus T dependence. Right panel: the low-temperature ρ versus T^2. The solid line represents the $\rho(T) = \rho_0 + AT^2$ fit.

The Fermi liquid theory is the accepted description of electron-electron interactions in metals and assumes a Fermi liquid ground state. To be specific, Fermi liquid behaviour is characterized by a quadratic temperature dependence for the resistivity, which is a direct consequence of the T-square dependence of the scattering rate. Because there is always a residual resistivity, due to lattice imperfections, vacancies or impurities, the resistivity for a Fermi liquid can only be found at low-temperature. At high-temperature contributions like phonons dominate the electron-electron scattering.

3.2.3 Magnetization

The temperature dependent magnetization of FeGe, measured at 5 G applied magnetic field, is shown in figure 3.4 (left panel). A sharp maximum appears at 280 K and corresponds to a transition from the paramagnetic phase to the helical magnetic state. As the applied magnetic field is increased the peak magnitude decreases and completely disappears. This behaviour suggests that the field induces a transition to a ferromagnetic phase. Similar shape of the magnetization has been seen in MnSi. In the paramagnetic state the magnetic susceptibility, $\chi = M/H$, follows the Curie-Weiss temperature dependence as can be seen in the figure 3.4 (right panel).

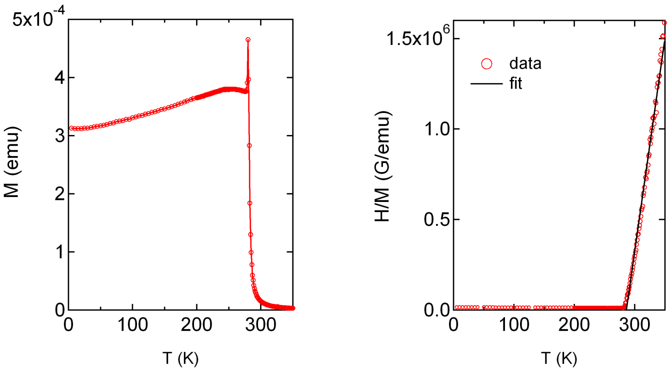

Figure 3.4: The magnetization of FeGe as a function of temperature. - Left panel: M versus T curve. Right panel: inverse magnetic susceptibility versus temperature and the Curie-Weiss fit.

FeGe, like MnSi, is considered to be a weak itinerant ferromagnet for which the magnetism arise from the spin polarization of the electronic bands, as described in Chapter 1.

3.3 Optical properties

Optical properties of FeGe were obtained using spectroscopic ellipsometry from 0.75 to 3.1 eV and near normal incidence reflectivity spectra measured in the energy range from 15 meV to 0.85 eV for temperatures from 30 to 296 K. The optical quantities, such as the complex dielectric function, $\epsilon(\omega)$, and complex optical conductivity, $\sigma(\omega)$, on a broad frequency spectral range, were obtained by combining the two sets of measurements and using a variational KK-constrained analysis described in detail in Chapter 2.

3.3.1 Frequency and temperature dependent optical quantities

Figure 3.5 shows the reflectivity, $R(\omega)$, the optical conductivity, $\sigma_1(\omega)$, and the dielectric function, $\epsilon_1(\omega)$, of single crystalline cubic FeGe at a series of temperatures from 30 to 296 K over a broad frequency range. The two distinct sharp excitations in the far infrared spectrum (28.5 meV, 35.9 eV) are due to optically active phonons [48]. In addition, small structures are seen at 49 meV and 65 meV. Repeated experiments showed that these two weak features are not reproducible. They coincide with the frequencies of strong interference fringes of the thin polyethylene cryostat window. The fact that they are not fully removed by the calibration procedure is due to a gradual evolution of the window properties during the time (several hours) lapsed before and after depositing the gold layer on the crystal.

We observe that at low-frequency the reflectivity increases with decreasing temperature. In contrast, the range between 62 meV and 0.18 eV $R(\omega)$ is strongly suppressed and a minimum develops at low-temperature. Consequently the far infrared region of the optical conductivity spectrum displayed in figure 3.5(b) is strongly temperature dependent. At low-temperature $\sigma_1(\omega)$ shows a minimum around 0.1 eV, which vanishes near T_C. Below the Curie temperature a peak in the optical conductivity appears at 0.22 eV which looks like an onset of interband transitions. We observe a narrowing of the free carrier response while the temperature is lowered to zero. However, a large finite conductivity remains below the interband transition at 0.22 eV which appears to be the high-energy tail of the free carrier response, due to the coupling to bosonic degrees of freedom. In the present case these are most likely spin fluctuations. The narrowing of the free carrier response signals a strong reduction in the scattering rate, whereas the simultaneous appearance of an interband transition is similar to observations in Kondo-lattice compounds like URu_2Si_2 [56], $CeAl_3$ [57], $CeCoIn_5$ and $CeIrIn_5$ [54].

It is also interesting to look at the temperature and frequency dependence

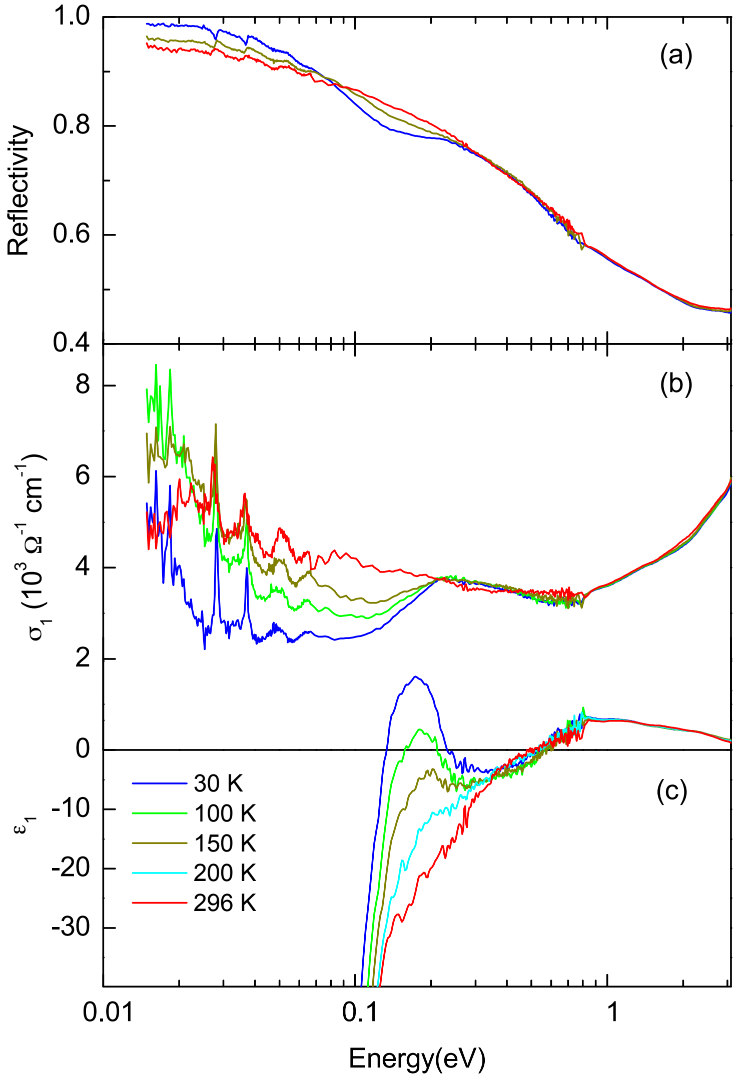

Figure 3.5: Optical spectra of FeGe. - (a) The normal-incidence reflectivity, (b) the optical conductivity and (c) the real part of the dielectric function of FeGe derived from the ellipsometry and reflectivity measurements at several temperatures ranging from 30 to 296 K on a logarithmic scale.

of the real part of the dielectric function plotted in figure 3.5(c). For a good metal $\epsilon_1(\omega)$ is large and negative at low-frequency. The behaviour for $\epsilon_1(\omega)$ and $\sigma_1(\omega)$ are consistent with each other as required by KK transformation. We observe that the dielectric function has a zero-crossing at 0.4 eV for all measured temperatures, which we assign to the plasma resonance of the conduction electrons. A second zero-crossing, occurs below 150 K. This low-frequency crossing is strongly temperature dependent and is shifting towards lower energy as the temperature is decreasing. Such a line shape of $\epsilon_1(\omega)$ resembles the heavy fermion systems, where the low-frequency plasmon is a characteristic feature of the heavy quasi-particles [54].

3.3.2 Band structure calculation

We calculated the electronic structure using the linear muffin-tin orbital (LMTO) code [40] with the self-consistent local spin-density approximation (LSDA) method, resulting in a ferromagnetic ground state with a magnetic moment of $1\mu_B$ per Fe-atom. The density of states, shown in figure 3.6, is consistent with the schematic density of states of Anisimov *et al.* (see figure 3 of Ref. [50]). The theoretical optical conductivity has been calculated as a sum of all band transitions within 2.7 eV of E_F at 9216 k-points of the irreducible Brillouin zone, including the dipole matrix elements. The effect of thermal disorder and zero-point motion on the band structure is introduced as a band broadening, which is assumed to be equal for all bands. The result of disorder is also a smearing of the spectra at higher energies. The parameter for the band broadening is estimated from calculations of disordered supercell calculations for FeSi and FeGe [49, 51].

The comparison between the calculated and measured optical conductivity (see figure 3.7) is not as good as for CoSi and FeSi [58]. Theoretically we find the onset of weak interband transitions at an energy as low as 80 meV followed by a gradual increase in the optical conductivity to a maximum of 0.4 eV. The experimental data show a minimum at 0.1 eV followed by a peak at 0.22 eV. In addition two peaks are predicted at 1.6 eV and 2 eV. The experimental high-frequency optical spectrum is less structured compared to the calculated one. The reason could be that at high-energy the scattering is very large. We associate the experimental maximum at 0.22 eV with the theoretical peak at 0.4 eV and the higher energy structures to the theoretical peak predicted at 1.6 eV. It is not uncommon in transition metal silicides to observe discrepancies between the energy of the measured and local density approximation (LDA) calculation peaks of the optical spectrum. The most likely source of these discrepancies is renormalization effects arising from the strong on-site Coulomb interaction of

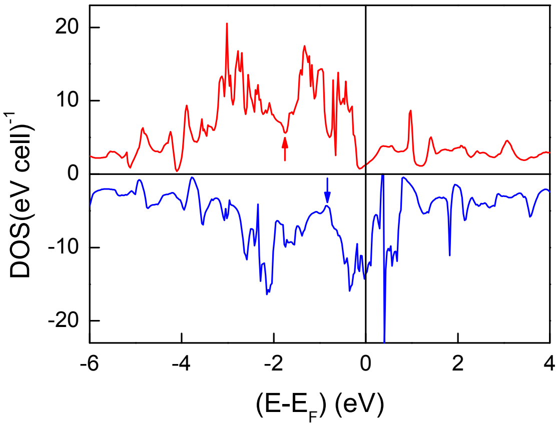

Figure 3.6: Spin-polarized density of states (DOS) of FeGe. - The energy is relative to E_F. Up and down arrows show the DOS for spin-up and spin-down, respectively.

the transition metal atoms. We have varied the lattice parameter in the LSDA calculation to see if this would improve the agreement with the experimental data, but the position of the peak at 0.4 eV turned out to be robust.

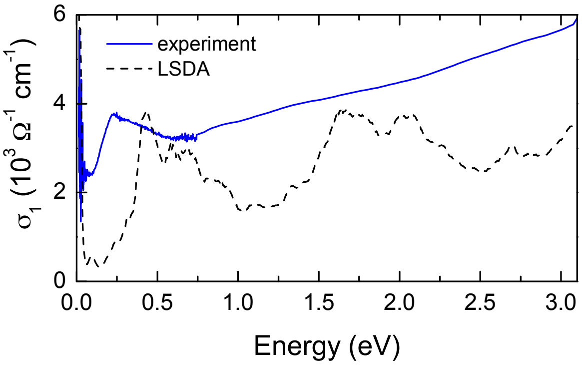

Figure 3.7: The optical conductivity spectra of the helimagnetic state of FeGe. - Solid and dashed lines denote the experimental and calculated optical spectra, respectively.

We have calculated the linear specific heat coefficient $\gamma = \frac{\pi^2}{3} k_B \, N(E_F)$ taking the density of states from figure 3.6. The band structure derived electronic specific heat coefficient is $\gamma_{calc.}$ = 4.4 mJ mol^{-1} K^{-2}. We measured a $\gamma_{meas.}$ = 10.4 mJ mol^{-1} K^{-2}. This value is roughly a factor of two larger then the value obtained from the band structure calculation suggesting some mass renormalization. Comparing the measured specific heat coefficient with the calculated one we obtain a mass enhancement $m^*/m = 2.4$.

3.3.3 Extended Drude model

The extended Drude model has been particularity interesting because of its successful applicability to a broad range of materials. This approach provides a natural way to go beyond the simple Drude model, in which the scattering rate and the effective mass are assumed to be frequency independent, by simply introducing a frequency dependent scattering rate, $1/\tau(\omega)$, and effective mass, $m^*(\omega)/m$, in the conductivity expression of the Drude model [36]. Both quantities $1/\tau(\omega)$ and $m^*(\omega)/m$ can be extracted from the measured complex dielectric function:

$$\frac{1}{\tau(\omega)} = -\frac{\omega_p^2}{\omega}\,\mathrm{Im}\left(\frac{1}{\epsilon(\omega)-\epsilon_\infty}\right), \tag{3.2}$$

$$\frac{m^*(\omega)}{m} = -\frac{\omega_p^2}{\omega^2}\,\mathrm{Re}\left(\frac{1}{\epsilon(\omega)-\epsilon_\infty}\right). \tag{3.3}$$

Here $\hbar\omega_p = \sqrt{4\pi ne^2/m_b} = 2.7$ eV is the Drude plasma frequency which acts as scaling factor here and is chosen so as to give $m^*(\omega)/m$ = 1 at 296 K and $\omega/2\pi c$ = 0.12 eV. Furthermore ϵ_∞ = 264 is the high-frequency dielectric constant due to the bound charge polarizability. We should point out that here $1/\tau(\omega)$ is the scattering rate of unrenormalized carriers while $m^*(\omega)/m$ is a renormalized quantity. We also should mention that this model is only meaningful in the energy region where the optical response is due to mobile carriers and not to bound ones. The strong temperature dependence of the optical data shown in figure 3.5(b) for frequencies below 0.1 eV, naturally assigned to the mobile carriers, suggests that this model can be applied at frequencies lower than 0.1 eV.

Figure 3.8 displays the spectra of effective mass (upper panel) and the scattering rate (lower panel) as a function of frequency for different temperatures. Note that at room temperature both the scattering rate and the effective mass are almost constant. However, as the temperature is reduced below the transition temperature, $1/\tau(\omega)$ shows strong frequency and temperature dependence. The value of the scattering rate at high-temperature becomes quite large and seems difficult to describe the metallic state of this material. On the other hand, at low-temperature $1/\tau(\omega)$ is much smaller than at room temperature. This behaviour of the scattering rate reflects the narrowing of the zero-frequency mode. This

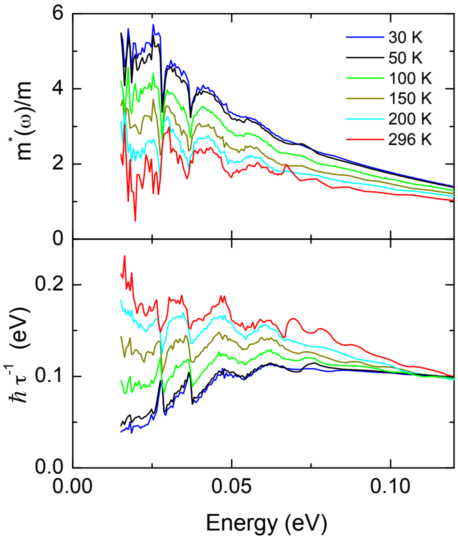

Figure 3.8: Extended Drude analysis of the optical conductivity of FeGe. - Upper panel: $m^*(\omega)/m$ versus frequency. Lower panel: $1/\tau(\omega)$ as a function of frequency. Here ω_p = 2.7 eV and ϵ_∞ = 264 as described in the text.

suggests that the temperature dependence of the optical response shown in figure 3.5(b) cannot be explained in terms of the simple Drude model. In addition, we notice a strong suppression of the scattering rate upon cooling, as in MnSi [58] and the heavy fermion compounds URu_2Si_2 [56], $CeAl_3$ [57], $CeCoIn_5$ and $CeIrIn_5$ [54], suggesting the development of heavy quasi-particles at low-temperature. As a result a renormalized Drude absorption due to these heavy quasi-particles is observed in the optical spectra. In relation to this, at low-frequency the electrons are dressed by interactions giving them a large effective mass. For $\omega \rightarrow 0$ we observe $m^*(\omega)/m \sim 5$. This value appears to be slightly higher compared to that calculated from a comparison of the band structure and specific heat value $m^*/m = 2.4$. A possible explanation for this difference is the fact that the mass enhancement in the specific heat and transport are associated with different bands in the electronic structure. At high-frequency the electrons are no longer dressed by the interaction and the effective mass reduces to the band mass as can be seen in figure 3.8 (upper panel). In contrast to the case of heavy fermions systems, FeGe has no $4f$-electrons but the large mass renormalization factor appears to be of the same order of magnitude as that observed in $CeCoIn_5$ and $CeIrIn_5$ [54]. In this context we speculate that FeGe may be considered as a $3d$ heavy fermion system.

The half-metallic ferromagnet chromium dioxide has an optical conductivity [59] very similar to that of FeGe. A suppression of $1/\tau(\omega)$ was observed below T$_C$, which was stronger than in FeGe. This is a natural consequence of the half-metallic ferromagnetism: Spin-flip scattering, which is the dominant scattering mechanism in ferromagnets, is completely suppressed for frequencies smaller than the gap separating the minority bands from the Fermi level. Note, that in *disordered* Co-doped FeSi, which is also a half-metallic ferromagnet, the opposite behaviour is observed, in that the scattering rate *in*creases in the magnetically ordered state [60, 61, 62].

3.4 Discussion

In FeSi the spectral weight removed at frequencies below 70 meV due to the opening of a gap at low temperatures, was observed not to be recovered for energies up to at least 6 eV [47, 63, 58]. Since this implies the coupling of the conduction electrons to high-energy scale excitations, possibly on the scale of the on-site Coulomb interaction, it may be an indication that the material has features in common with a Kondo lattice, and the insulating gap of FeSi is due to strong local electron correlation effects presumably in the $3d$-shell of the iron atoms. In view of the structural and chemical similarities between FeSi and FeGe, one might suspect electron correlation effects to be equally important in the latter material. While FeGe has no insulating gap at low temperatures, the optical spectra depend strongly on temperature. In order to estimate the transferred spectral weight the function

$$N_{eff}(\omega) = \frac{2mV}{\pi e^2} \int_0^{\omega_c} \sigma_1(\omega) d\omega \tag{3.4}$$

is displayed in figure 3.9 (left panel) together with $N_{eff}(\omega)$ of FeSi (right panel) from Ref.[63].

For $\omega_c \to \infty$ this represents the total number of electrons per formula unit of FeGe. In the region below 0.1 eV we observe at low temperatures that $N_{eff}(\omega)$ increases more sharply as a function of frequency than the high-temperature data, which is a consequence of the fact that $1/\tau$ is smaller and the Drude peak narrower at low-temperature. However, all curves cross at 0.1 eV, and above 0.18 eV $N_{eff}(\omega, \text{296 K})$ exceeds $N_{eff}(\omega, \text{30 K})$ by a constant amount of $\simeq 0.005$ per FeGe formula unit. In other words: Just like in FeSi, cooling down the sample results in a loss of spectral weight in the frequency range 0.1 eV, which is not recovered over a broad frequency range. We note that the temperature dependence of $\epsilon_1(\omega, T)$ for $\hbar\omega \approx 1$ eV observed directly with ellipsometry confirms quantitatively the trends seen in figure 3.9 (left panel). This suggests

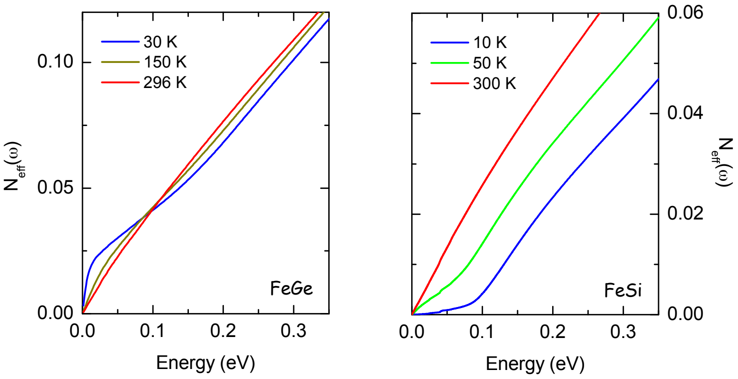

Figure 3.9: The integrated spectral weight for a number of representative temperatures. - For comparison we plot $N_{eff}(\omega)$ of FeGe (left panel) and $N_{eff}(\omega)$ of FeSi (right panel) from Ref. [63].

that in FeGe, just as in FeSi, spectral weight is redistributed over an energy range of order 1 eV or higher when the temperature is varied. This behaviour may have its origin in the temperature dependence of the electron correlations resulting from the Hund’s rule interaction on the Fe-atoms [47, 46], or in a change of character of the bands near E_F due to thermal disorder [40], or in a combination of the two.

3.5 Conclusions

Different techniques, specific heat, resistivity and magnetization, were used to characterize the FeGe samples. All measurements are in agreement with the occurrence of magnetic order at T_C = 280 K. We also reported a systematic study of the optical properties of single crystalline cubic FeGe, with detailed frequency and temperature dependence. At the temperature where magnetic order occurs, a distinct and narrow free carrier response develops, with a frequency dependent scattering rate and a moderate mass enhancement in the zero-frequency limit. Similar behaviour as in FeSi is observed in FeGe, where the low-energy (Drude) spectral weight appears to be transferred to higher energies, on an energy scale of at least 1 eV, when the material is cooled down. This, together with the observed frequency dependent mass enhancement, indicates the important role of electron correlations in these materials.

Chapter 4

Optical spectroscopy of UGe_2

In this chapter we report a detailed study of UGe_2 single crystals using infrared reflectivity and spectroscopic ellipsometry. The optical conductivity suggests the presence of a low-frequency interband transition and a narrow free-carrier response with strong frequency dependence of the scattering rate and effective mass. We observe a sharp increase in the low-frequency mass and a reduction of the scattering rate below the upper ferromagnetic transition, T_C = 53 K, indicating the emergence of a heavy fermion state trigged by the ferromagnetic order. The characteristic changes are exhibited most strongly at an energy scale below 12 meV. They recover their unrenormalized value above T_C and for $\omega >$ 40 meV. In contrast no sign of an anomaly is seen at the lower transition temperature of unknown nature, $T_x \sim$ 30 K, observed in transport and thermodynamic experiments. The frequency dependent scattering rate at low-temperature is found to be compatible with the Stoner model.

4.1 Introduction

The possibility of unconventional superconductivity mediated by ferromagnetic fluctuations has long been a subject of theoretical speculation [64, 65]. Interest in this subject has been recently renewed with the discovery of superconductivity coexisting with the ferromagnetic state of UGe_2 under pressure [4]. UGe_2 is a strongly anisotropic uniaxial ferromagnet with partially filled $5f$-electron states. Due to correlations and conduction band $5f$ hybridization, carrier masses are found to be strongly enhanced [5] $[(10-25)m_0]$ although specific heat coefficients still fall an order of magnitude short of the largest values found in antiferromagnetic uranium-based heavy fermion compounds. UGe_2 exhibits a

Curie temperature that strongly decreases with increasing pressure from about 53 K at ambient pressure to full suppression around 1.6 GPa. Superconductivity exists in a pressure region from 1 to 1.6 GPa, just below the complete suppression of ferromagnetism [4]. This was surprising as superconductivity and ferromagnetism are usually found to be antagonistic phenomena. However, the observation fits within the now common scenario of finding superconductivity near the zero-temperature termination of a magnetic phase. In this sense it seemed quite natural to associate the superconductivity with the magnetic fluctuations that diverge at a quantum critical point (QCP), perhaps, as in the case of pressure driven superconductivity in the antiferromagnetic heavy superconductors. However, the paramagnetic to ferromagnetic transition is strongly first-order and is not associated with a peak in the effective electronic mass or superconducting transition temperature. It therefore appears that superconductivity is not directly related to the quantum phase transition connecting the ferromagnetic and paramagnetic states [66, 67].

In addition to the main ferromagnetic transition T_C (see figure 4.1 right panel), there appears to be a secondary first-order transition, T_x, of more enigmatic origin at lower temperatures which has been observed in many experiments such as resistivity [66, 68, 69] magnetization [67] and heat capacity [68, 69]. As seen from the figure 4.1 at p = 0, T_x = 30 K, with increasing pressure T_x decreases and becomes zero at the pressure $p_x \approx$ 1.2 GPa. The critical pressure, p_x, is very close to the pressure where the superconducting temperature is maximum and it may be that the superconductivity is mediated *via* fluctuations from this weak first-order transition. The exact nature of the state below T_x is not clear at present. It has been suggested that these two magnetic phases are related by a first-order Stoner-type phase transition in the spin magnetization due to a sharp double-peak in the density of states near E_F [70]. An alternative suggestion is that a competition between the dominance of spin-orbit coupling and crystal field effects drives a change in the local moment configuration [71]. Other possibilities such as a coexisting charge-density wave or spin-density wave order exist, however neutron scattering has failed to detect any such phases thus far [66]. We also note that at ambient pressure the signatures of the lower transition T_x is only weakly visible in the resistivity [72] and magnetization measurements [67, 73]. Moreover there is also no or almost no anomaly in the specific heat at ambient pressure [66, 69]. It may be that this transition at T_x does not extend all the way to zero-pressure and, in fact, the line of first-order transitions terminates in a critical end point at finite temperature and pressure. T_x at ambient pressure is then indicative of a crossover and not a true phase transition.

4.2 Crystal structure and magnetic properties

UGe_2 crystallizes in orthorhombic crystal structure with lattice parameters a = 4.0089 Å, b = 15.0889 Å and c = 4.0950 Å [74]. Figure 4.1 (left panel) displays the crystal structure of UGe_2 together with the pressure-temperature phase diagram reproduced from the Ref. [69]. The crystal structure can be viewed as zigzag chains of U atoms running along the a crystallographic axis. The magnetic properties of UGe_2 are strongly anisotropic with the easy magnetization direction corresponding to the a-axis. The ferromagnetically ordered magnetic moment is of 1.48 μ_B/uranium which is much lower than the full moment of 3.6 μ_B of Uf^3 configuration and is smaller than the Curie Weiss moment (2.7 μ_B) measured above the Curie temperature [66]. Experimentally an enhancement of the magnetic moment from 1 μ_B/U at ambient pressure to 1.35 μ_B/U at about 0.9 GPa is observed below the second magnetic transition, T_x, [66, 69]. Therefore the region between the two magnetic phases (see figure 4.1 (right panel) green region) is called the weakly spin-polarized phase, while the region below T_x (see figure 4.1 (right panel) yellow region) is called the strongly spin-polarized phase [66]. Moreover, the electronic contribution to the specific heat at low-temperature shows a large value γ = 35 mJ mol^{-1} K^{-2} which suggests mass renormalization effects. Indeed carriers with heavy masses were found in de Haas-van Alphen (dHvA) measurements, suggesting itinerant but strongly correlated $5f$-electrons. These values are rather small when compared with the

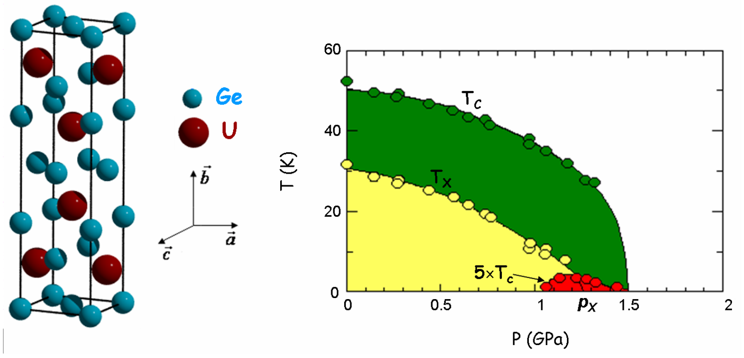

Figure 4.1: The crystal structure and the phase diagram of UGe_2. - Left panel: The orthorhombic C_{mmm} based centered crystal structure (red circles uranium atoms, blue circles germanium atoms). The unit cell contains two formula units of UGe_2. Right panel: Sketch of the temperature-pressure phase diagram after the Ref. [69]. The main ferromagnetic transition, T_C, the second magnetic transition, T_x, and the superconducting transition, T_c, are indicated.

values of other uranium based heavy fermion systems which suggests that UGe$_2$ is a moderately heavy fermion system.

Additionally, in UGe$_2$ like in most of the uranium based heavy fermion systems the $U - U$ distance is found to be larger then the so called Hill limit ($d_{U-U} = 3.25 - 3.5$). Therefore, no direct overlap between the $5f$-electrons is expected which suggests the presence of local moments on the uranium site. The hybridization between the $5f$-electrons and the $3d$-electrons of Ge are likely to be responsible for the smaller uranium magnetic moment compared to the free ion moment. The difference in value of the paramagnetic and ordered magnetic moment is observed in the $3d$ magnetic metals and is consistent with the itinerant electron magnetism picture.

4.3 Results

The optical measurements were performed in the frequency range from 6.2 meV to 3.7 eV combining infrared reflectivity via Fourier transform spectroscopy, and ellipsometry from the visible to ultraviolet energy range. The absolute value of the reflectivity, $R(\omega, T)$, was measured by calibrating the signal against a reference gold layer evaporated *in situ* on the sample surface. Ellipsometry and infrared data were combined using the procedure described in Chapter 2 in order to extract the frequency dependent and temperature dependent optical quantities such as, for instance, the complex conductivity, $\sigma(\omega, T)$, over a broad energy range. The sample used for this study was grown at the CEA, Grenoble by the Czochralski technique [4]. Measurements were taken in quasi-normal incidence to the ac-plane using linearly polarized light. We found only a small shift of the optical spectra between the two crystal directions with any difference being smaller then our experimental accuracy (1$\%$). The displayed spectrum is the average between these two directions.

4.3.1 Reflectivity spectra

Figure 4.2 (left panel) shows the reflectivity spectra, $R(\omega)$, over the full measured energy range from above T_C down to 11 K. At high-temperature $R(\omega)$ exhibits a monotonic increase as expected for a metal with $R(\omega) \rightarrow 1$ as $\omega \rightarrow 0$. As the sample is cooled below T_C the reflectivity shows a significant increase with the largest effects at low-frequency. Reflectivity spectra for three different frequencies are shown in figure 4.2 (right panel). It can be seen that with decreasing temperature the low-frequency data increase strongly below T_C. However, no sign of an anomaly is found at the temperature T_x, which may be not surprising considering its weak signature in transport and thermodynamics at ambient pressure.

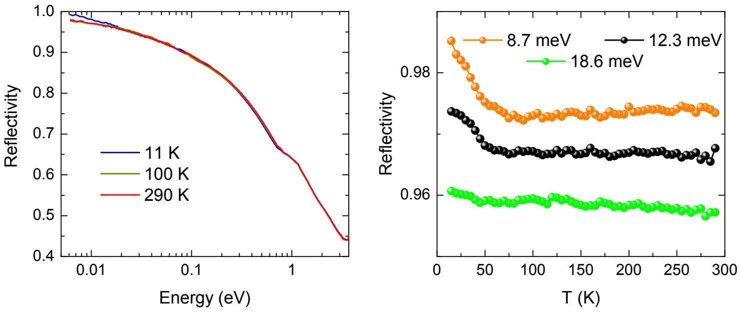

Figure 4.2: Near-normal incidence reflectivity spectra of UGe$_2$. - Left panel: $R(\omega)$ at three distinct temperatures: 11, 100 and 290 K. The reflectivity curves at 100 and 290 K overlap on this scale. Right panel: $R(\omega)$ versus T at 8.7, 12.3 and 18.6 meV.

We observe that the reflectivity has no significant temperature dependence above 0.12 eV, which suggests negligible temperature dependence at higher frequencies. We used therefore room temperature ellipsometry for frequencies greater then 0.74 eV to perform a KK analysis and calculate the complex optical conductivity over the entire spectral range displayed in figure 4.3(a).

4.3.2 Optical conductivity

In order to investigate the electronic structure quantitatively we plot in figure 4.3(a) the optical conductivity spectra. At high-temperature the low-frequency optical conductivity, $\sigma_1(\omega)$, shows a broad Drude like behaviour as expected for a metal. The high frequency optical conductivity is dominated by interband transitions. We assign the sharp peak at approximately 1 eV to an interband transition.

The low-frequency $\sigma_1(\omega)$ is strongly temperature and frequency dependent. To clarify this trend we show the enlargement of the low-energy data in figure 4.3(b). Several remarkable low-frequency structures form at low temperatures out of the broad Drude peak, including a very narrow zero-frequency mode which represents the intraband response of the heavy quasi-particles. The presence of a narrow zero-frequency mode is born out by two independent pieces of evidence: First, the imaginary part $\sigma_2(\omega)$ of the optical conductivity, plotted in figure 4.3(c), rises sharply when temperature is lowered below T_C. This implies a strong increase in metallic screening originating from the zero-frequency

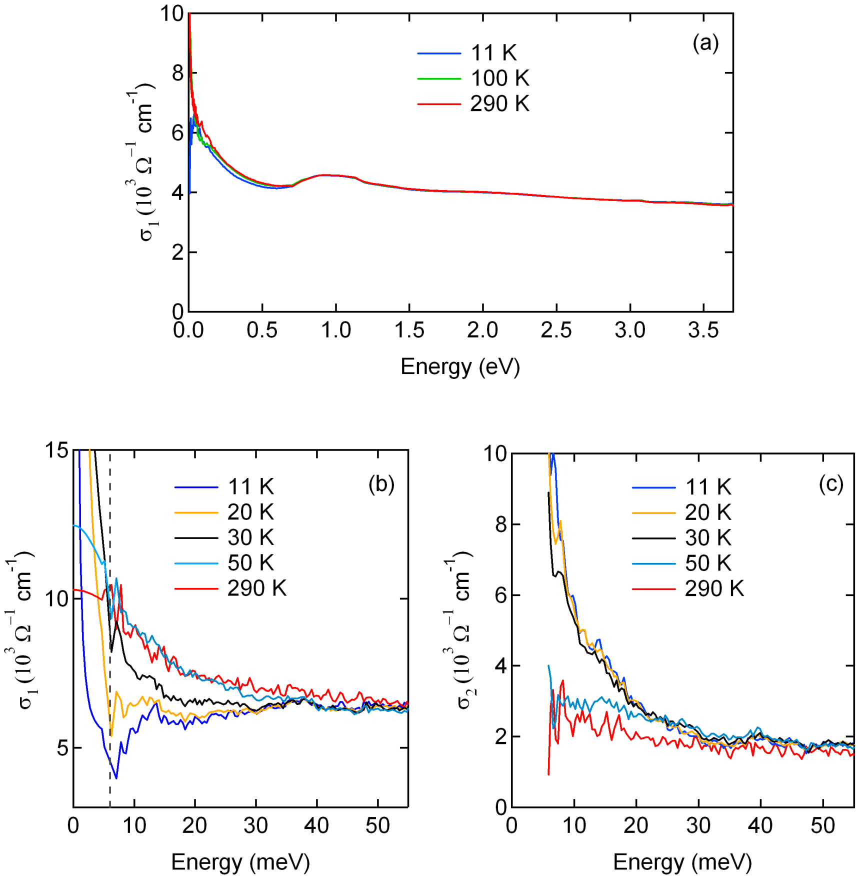

Figure 4.3: Optical conductivity spectra for several temperatures. - (a) $\sigma_1(\omega)$ over the entire measured spectral range from 6.2 meV to 3.7 eV. (b) The enlargement of the low-energy data including the zero-frequency extrapolations. (c) $\sigma_2(\omega)$ at different temperatures.

mode below the 6.2 meV threshold of the reflectivity data. The second piece of evidence is that comparing the dc resistivity at 11 and 290 K, $\sigma_1(\omega = 0)$ increases by a factor of 48. This ratio is very close to the extrapolated conductivity ratio $\sigma_1(\omega \rightarrow 0$, 11 K) / $\sigma_1(\omega \rightarrow 0$, 290 K) = 50. This proves that there is really a narrow zero-frequency mode in the optical spectra at low temperatures. Concomitantly, a maximum develops at 13.6 meV and a weak structure at 37 meV. As will be shown below, these features reflect various aspects of the coherent heavy fermion and ferromagnetic states.

4.3.3 Frequency dependent scattering rate and effective mass

In order to get further on analyzing the shape of the low-frequency spectra we use the extended Drude model. According to this formalism the optical constants are expressed in terms of frequency dependent effective mass, $m^*(\omega)/m$, and scattering rate, $1/\tau(\omega)$, by the following expression:

$$\frac{m^*(\omega)}{m} = -\frac{\omega_p^2}{4\pi\omega} Im\left[\frac{1}{\sigma(\omega)}\right], \qquad \frac{1}{\tau(\omega)} = \frac{\omega_p^2}{4\pi} Re\left[\frac{1}{\sigma(\omega)}\right], \tag{4.1}$$

where $\hbar\omega_p = \sqrt{4\pi n e^2/m_b} = 3.5$ eV is the total Drude plasma frequency and $\sigma(\omega)$ is the complex optical conductivity. $\hbar\omega_p$, which is determined through $m^*(\omega)/m = 1$ at 290 K and ω = 62 meV, acts as a normalization constant and does not affect the trends as a function of frequency and temperature.

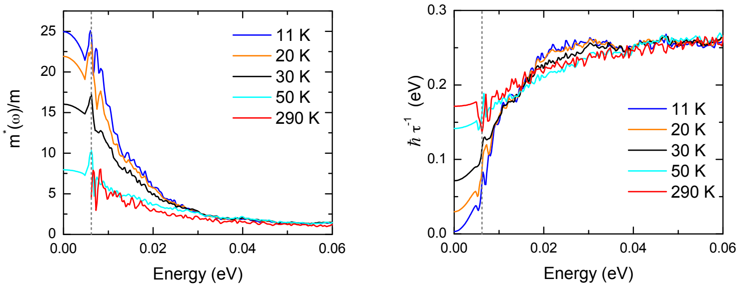

Figure 4.4: Extended Drude model for UGe$_2$. - Left panel: $m^*(\omega)/m$ versus frequency. Right panel: $1/\tau(\omega)$ versus frequency. The extrapolations towards zero-frequency are shown below 6.2 meV (dashed grey line) which yield an estimation of the quasi-particles effective mass.

Figure 4.4 displays the spectra of $m^*(\omega)/m$ (left panel) and $1/\tau(\omega)$ (right panel) as a function of frequency obtained from the extended Drude model for different temperatures. At room temperature both the scattering rate and the effective mass are nearly frequency independent. One should point out that the details in $1/\tau(\omega)$ above 12 meV are probably caused by the proximity of the onset of the low-energy interband transitions. As the sample is cooled down and the magnetic order develops the effective mass is strongly enhanced and the scattering rate suppressed. Such behaviour suggests the development of heavy quasi-particles at low-temperature. We observe that the strong increase in the effective mass and the rapid decrease in the scattering rate are largest below approximately 12 meV which can be regarded as the characteristic energy of the heavy quasi-particles. Below 6.2 meV we plot the extrapolation towards zero-frequency which gives an estimation of the quasi-particle’s effective mass. The optically observed mass enhancement exceeds the value of 25 for $\omega \rightarrow 0$ at the lowest measured temperature. Qualitatively this value is consistent with the cyclotron masses of (10 - 25)m_0 obtained by the dHvA measurements [5].

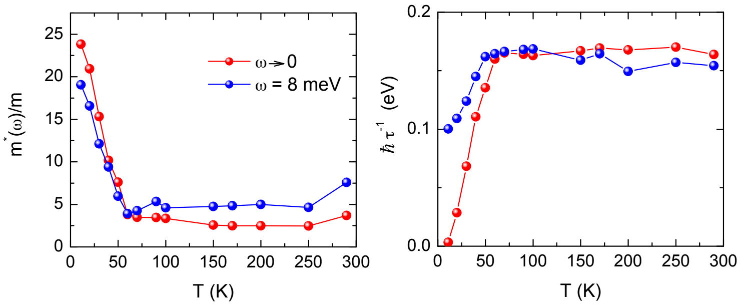

Figure 4.5: Temperature dependence of the effective mass and the scattering rate. - The left and right panels show $m^*(\omega)/m$ and $1/\tau(\omega)$ for $\omega \rightarrow 0$ and 8 meV, respectively.

In Figure 4.5 we present the temperature dependence of the effective mass (left panel) and scattering rate (right panel) at $\omega \rightarrow 0$ and 8 meV obtained from figure 4.4. Note that at high-temperature, in the paramagnetic state, both quantities are temperature independent. However, starting exactly at T_C the scattering rate becomes strongly suppressed and the effective mass enhanced. Such behaviour contrasts with the usual situation in heavy fermion compounds, where mass renormalizations develop below a coherence temperature, T^*, different than the transition temperature to a magnetic state. Moreover, the conventional view is that the coherent heavy fermion state should actually be *suppressed* at a magnetic transition as the dominance of the RKKY interaction is expected to quench the Kondo effect [29]. The observed behaviour is not completely unprecedented; however, a number of other multi f electron compounds have been found to undergo additional mass enhancements at the magnetic transition [36]. In the present case however the magnetic transition appears to actually trigger the heavy fermion state suggesting an intrinsic $T^* < T_C$. This behaviour may be related to multiple occupation of the $5f$-levels, although we note that a similar effect in $3d$-electron systems has also been observed at the T_C of ferromagnetic $\mathrm{Yb_{14}MnSb_{11}}$ [75] and helimagnetic FeGe (see Chapter 3).

4.4 Discussion

The relatively large mass enhancement observed in $\mathrm{UGe_2}$ suggests the evolution of renormalized itinerant charge carriers out of a Fermi gas coupled to a lattice of f electron local orbitals. At high-T the $5f$-electrons seem to be more localized [76]. As the temperature is decreased the character of $5f$-electrons changes from localized to itinerant. Several aspects of the behaviour of the f-electrons as they move from the localized to itinerant regime have been discussed in the literature[77, 78, 79]. It is generally accepted that the periodic Anderson model (PAM), which describes the hybridization of a localized level with a conduction band, captures the essential physics of such systems [27, 80]. In figure 4.6 we plot a schematic band dispersion of the PAM together with its optical conductivity at low and high temperatures. A significant difference is observed between the two limits. At high-temperature only a dispersive conducting band crosses the Fermi level (E_F), whereas the (partially filled) $5f$-bands at E_F are dispersionless. The intraband transitions give rise to a broad Drude conductivity sketched in figure 4.6(c). As the temperature is lowered, hybridization with the f-level splits the conduction band into two branches and is responsible for the large effective mass observed at low-temperature. The additional scattering suppression which onsets at T_C implies a strong coupling between heavy fermion effects and magnetic ones with important implications for superconductivity. Therefore the occurrence of the heavy fermion and the ferromagnetic states cannot be explained using only the hybridization model; the effects of ferromagnetism have to be included. As the temperature is lowered, the material enters in a magnetically ordered state, which on one hand suppresses the channel for inelastic spin-flip scattering near E_F, and on the other hand converts the $5f$ spin degrees of freedom into a narrow band of heavy charge carriers. This coherent band, partially occupied, and therefore pinned to E_F exhibits avoided crossings with the wide conduction bands, due to hybridization. Excitations between the split bands create the possibility for new interband transitions from filled states below the Fermi level into unoccupied levels above E_F shown by the vertical arrow in figure 4.6(b). The spectral weight is removed from the

Drude peak and redistributed between the high and low energies as sketched in figure 4.6(d).

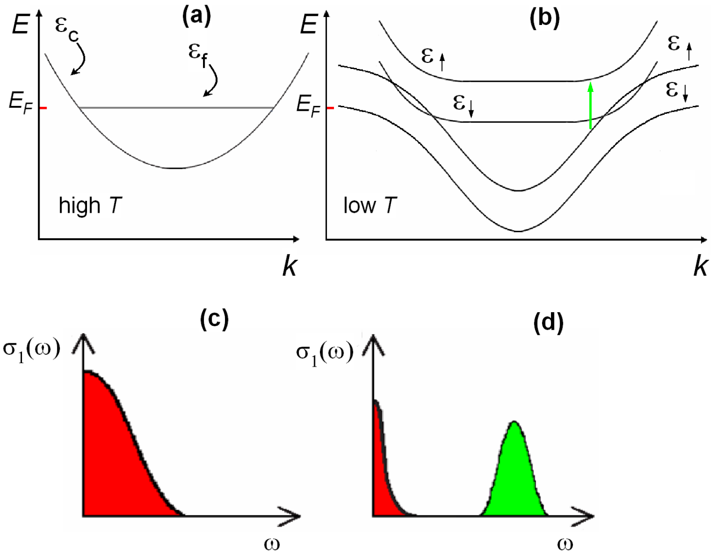

Figure 4.6: Band dispersion of the PAM together with its optical conductivity. - (a), (b) Schematic band structure within the PAM of the conduction, ϵ_c, and the $5f$-electrons, ϵ_f, at high and low temperatures, respectively. Vertical arrow indicates the interband transitions. $\epsilon_\uparrow$ and $\epsilon_\downarrow$ denote the spin-up and spin-down bands. (c), (d) Sketch of the optical conductivity at high and low temperatures.

Although this general picture should hold in UGe$_2$, additional features in principle are expected as a result of uranium’s nominal $5f^3$ configuration which results in several $5f$ bands being involved in the heavy electron state. Moreover, as has been suggested for CeCo$_{1-x}$Ir$_x$In$_5$, a distribution of hybridization gaps due to a momentum dependence of the $f-d$ coupling parameter [81, 78, 79] may result in multiple features in $\sigma_1(\omega)$, such as seen in figure 4.3(b) at 37 meV and 13.6 meV.

The observed suppression of the scattering rate is additional to that expected generically for heavy fermion compounds below their coherence temperatures. The usual expectation is that the effective mass, m^*, and the quasi-particle lifetime, τ^*, are renormalized by approximately the same factor [80]. In contrast, comparing the low-temperature scattering rates and masses with their high-temperature unrenormalized values we find the ratios $\frac{m^*}{m} \approx 6$ and $\frac{\tau^*}{\tau} \approx 50$, which disagree by a factor of 8. A similar analysis using instead the high-frequency values gives a similar discrepancy. It is also interesting to note that as the temperature increases the energy scale of the threshold in $1/\tau(\omega)$ does not appear to close at the transition, but instead the gap "fills in" and a remnant of this suppression persists even up to 290 K. Similar effects have been observed in ferromagnetic nickel [82]. This observation of gaps which fill in instead of closing is a common occurrence in strongly correlated systems [83].

In the optical spectra shown in figure 4.4 (right panel) we observe a rather strong but incomplete suppression of $1/\tau(\omega)$ for frequencies smaller than about 6 meV. The suppression of the scattering rate, which onsets at T_C is reminiscent of that which occurs at energies below the Stoner gap in fully spin-polarized ferromagnets such as CrO_2 [59]. In such cases longitudinal Stoner-type spin-flip scattering is forbidden at energies below a threshold set by the energy difference from the bottom of the minority band to the Fermi level (the Stoner gap). UGe_2 is not fully spin-polarized but has only a small minority spin population at E_F [84, 85]. Moreover, the behaviour of properties such as the pressure dependent magnetization and the pairing mechanism for superconductivity [70] have been interpreted as a consequence of narrow peaks in the density of states, which could give an effective gap to spin-flip excitations. Such a density of states is supported by band calculations [71]. Longitudinal fluctuations which can possibly mediate exotic superconductivity, have been found by neutron scattering [86]. An effective gap to longitudinal spin-flip excitations has also been inferred through a Stoner model fit to the strength of magnetic Bragg peaks at low-temperature with a gap that is on the order of the threshold in the optical scattering rate [87]. It is interesting that our spectra give a strong indication of a coupling of charge to these longitudinal fluctuations that were originally proposed as a possibility to mediate superconductivity in ferromagnetic compounds.

4.5 Conclusions

To summarise, we investigated the optical properties of UGe_2 over a wide range of energy and temperature. Our optical data show significant changes below the Curie temperature. In particular the reflectivity shows a distinct anomaly at this temperature. On the other hand the second phase transition at lower temperatures observed in transport and thermodynamic experiments, T_x, appears to be rather evasive and no signatures of it are seen in the optical spectra. At low temperatures a renormalized zero-frequency mode develops. The effective mass strongly increases on cooling below a characteristic energy of 12 meV. At 11 K it reaches the value of 25 for $\omega \rightarrow 0$. In the ferromagnetic state we find signatures of a strong coupling to the longitudinal magnetic excitations that have been proposed to mediate unconventional superconductivity in this compound. Our observations suggest an interesting interplay between spin polarization and the heavy fermion coherent state. We believe that this is at the origin of the rather rich behaviour of the optical conductivity, resulting in two structures appearing below T_C (13.6 and 37 meV) and large quasi-particle renormalizations. The optical data indicate that the magnetic order triggers the transition into a state characterized by heavy and weakly scattered charge carriers.

Chapter 5

Optical spectroscopy of $Gd_5Si_2Ge_2$

The discovery of a giant magnetocaloric effect in $Gd_5(Si_xGe_{1-x})_4$ [7], has motivated extensive investigation of this material during the last years. The alloys exhibit a number of unique properties associated with their crystallographic transformations in combination with the magnetic transitions [88]. The fact that the phase transition can be tuned by temperature, chemical composition, pressure and magnetic field, is accompanied by a giant magnetocaloric effect [7], a colossal magnetostriction [89] and a giant magnetoresistance [90] makes this class of material very attractive. The electronic properties of the pseudo-binary $Gd_5(Si_xGe_{1-x})_4$ are quite remarkable. Gd_5Ge_4 is an antiferromagnet below 15 K, while Gd_5Si_4, with just a slightly different crystal structure, is a ferromagnet up to 336 K [91]. The question why the Curie temperature of the sillicide Gd_5Si_4 is 40 K larger than in pure Gd has not been resolved for almost 40 years. By changing the chemical composition namely Si to Ge in $Gd_5(Si_xGe_{1-x})_4$, the Curie temperature can be changed from 20 K to room temperature. It is not known whether preferential site occupancy exists for Ge and Si or whether the distribution of Ge and Si sites is completely random.

Despite the fact that the magnetic effects are understood on phenomenological grounds, based on the phase transition and the known crystal structure, the electronic structure of these materials remains virtually unexplored, and the microscopic mechanism for the ferromagnetism has not yet been revealed.

In this chapter we report the optical properties of anisotropic $Gd_5Si_2Ge_2$ as measured by infrared reflectivity and ellipsometry in the spectral range of 6.2 meV to 6 eV. The results suggest the presence the of a new phase transition at low-temperature, below 45 K. The anisotropic optical conductivity is obtained, as well as the dielectric function, the reflectivity and important electronic properties such as interband transitions. By comparing the measured optical spectra with spectra that are based on first principles calculations, we obtain information on the electronic band structure of Gd$_5$Si$_2$Ge$_2$.

5.1 Crystal structure and magnetic properties

The crystal structure of intermetallic compound Gd$_5$Si$_2$Ge$_2$ is very complex containing 36 atoms per unit cell [92, 93]. At high-temperature Gd$_5$Si$_2$Ge$_2$ crystallizes in a monoclinic type crystal structure, as shown in figure 5.1. Upon cooling first, it orders magnetically at T_C = 299 K without changing the crystal structure. Then, upon further cooling a structural phase transition from high-temperature monoclinic to a low-temperature orthorhombic structure occurs simultaneously with a first-order ferromagnetic transition at T_C = 267 K. It is known from the susceptibility measurements that when warming up the coupled magnetic crystallographic transition occurs at 276 K. The nature of the high-

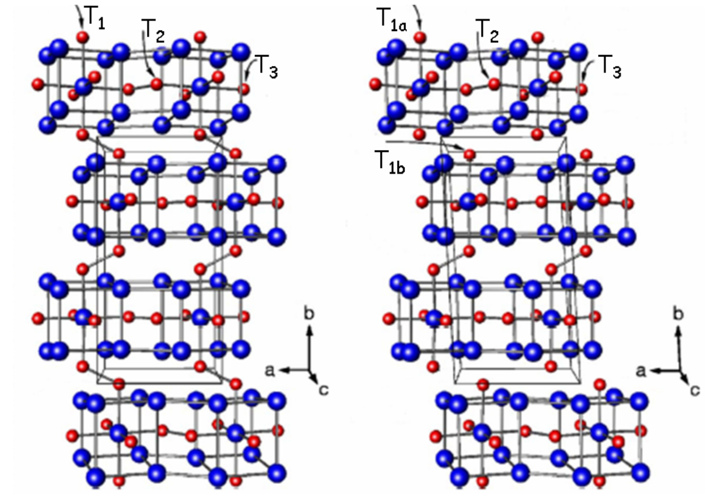

Figure 5.1: Crystal structure of Gd$_5$Si$_2$Ge$_2$. - Low-temperature orthorhombic phase (left panel) and high-temperature monoclinic phase (right panel) from Ref. [94]. Gd atoms are shown as a blue spheres and Si/Ge are shown as a red spheres. T_1 atoms represent a mixture of Ge and Si atoms (60% Ge and 40% Si) in the interslab positions, while T_2 and T_3 atoms represent a mixture of Si and Ge atoms (60% Si and 40% Ge) atoms in intraslab positions.

temperature magnetic transition is not clear at present but the magnetization data indicate a ferromagnetic behaviour without forming long range order. Under magnetic field, the temperature of both transitions increases which supports the magnetic nature of these transitions. In addition the magnetocaloric effect in $Gd_5Si_2Ge_2$, which is a consequence of the coexistence of the structural transformation with the magnetic order, is reversible when sweeping magnetic field. Moreover the magneto-structural transition is always complete and reversible, although it is characterized by a noticeable hysteresis. It is worth noting that this transition can be triggered by temperature, magnetic field and pressure.

The details of the exchange mechanism in $Gd_5Si_2Ge_2$ remain yet to be clarified. Although the indirect exchange RKKY interaction, accepted as the main mechanism responsible for magnetism in f-electron systems, can be used to describe the intralayer magnetic interactions, the formation of the covalent-like interslab bonds across the phase transition suggests that the superexchange type interaction mediated via a network of Gd-Si/Ge-Si/Ge-Gd bonds connecting the slabs plays an important role in magnetism of this material. The structural phase transition from the high-temperature monoclinic phase to the low-temperature ferromagnetic orthorhombic phase is caused by the breaking of the Si/Ge slabs. In the monoclinic structure two interslab bonds per unit cell are present, while in the orthorhombic phase all of the Si/Ge-Si/Ge pairs per cell are formed. One of the remarkable structural features of this transformation is breaking and reforming of covalent-like bonds between some of the Ge and/or Si atoms on heating and cooling, respectively.

Another interesting structural aspect of $Gd_5Si_2Ge_2$ is the fact that the low-temperature orthorhombic phase has a higher symmetry then the high-temperature monoclinic phase. This unusual behaviour arises from the strong magnetic exchange coupling at low-temperature in the orthorhombic phase. In addition it was found out that in the monoclinic phase the crystals show a macroscopic twinning, which vanishes as the crystal is cooled below T_C = 260 K in the orthorhombic phase, and reappears on heating above T_C [93].

5.2 Measurement details

Optical measurements were performed in the frequency range from 6.2 meV to 6 eV using near normal incident optical reflectivity in combination with ellipsometry with an overlapping frequency range. For the experiments the sample was aligned using an x-ray diffraction technique and freshly polished with, 0.5 μm diamond paper giving an optically flat surface. Immediately after polishing the sample was introduced in to a vacuum cryostat where the temperature dependence measurements were performed from room temperature down to 11 K. For ambient pressure measurements the sample was kept in a flow of dry nitrogen in order to avoid the oxidation of the surface. Near normal incidence reflectivity spectra, $R(\omega)$, were measured on the ab-plane using linearly polarized light. Two rotating polarizers were used in order to probe the optical response along a and b axes. The absolute value of the reflectivity was obtained using a reference gold layer evaporated *in situ* on the sample surface as described in Chapter 2.

Because Gd$_5$Si$_2$Ge$_2$ is an anisotropic material, in ellipsometry experiments we measured the complex pseudodielectric function for two different sample geometries. The corresponding spectra allow the extraction of the complex dielectric response for the a and b directions. As mentioned above the room temperature crystal structure of Gd$_5$Si$_2$Ge$_2$ is monoclinic, therefore off diagonal components occur in the Jones reflection matrix [95]. This requires a sophisticated analysis in order to obtain the dielectric tensor from the ellipsometry parameters [96]. However considering the small deviation of only 3 degrees from the orthogonal structure we expect only a small off-diagonal contribution.

5.3 Optical spectra

Figure 5.2 displays the reflectivity spectra of the Gd$_5$Si$_2$Ge$_2$ measured along the two crystallographic axes ($E\|a$, upper panel, and $E\|b$, lower panel) over a wide spectral range. For both polarizations, a sharp onset is seen in the reflectivity spectra near 0.5 eV, which can be identified as the plasma edge, $\omega_p^\star$. Further the reflectivity edge shifts in frequency from 0.54 eV at 290 K to 0.46 eV at 11 K along the a-axis and from 0.5 eV at 290 K to 0.39 eV at 11 K along the b-axis as shown in figure 5.2 (insets). The structures above $\omega_p^\star$ are due to interband transitions. With decreasing temperature, the mid-infrared reflectivity along the a-axis shows small changes and a gradual increase is observed below 0.2 eV. On the other hand the mid-infrared reflectivity along the b-axis is strongly temperature dependent and an increase appears below 0.1 eV. Moreover a small peak emerges around 0.12 eV along the b-axis. This peak is already present in the room temperature data (290 K) and does not seem to exhibit changes across the magneto-structural transition.

A deeper understanding of the optical response is obtained from the optical conductivity data. The real part of the optical conductivity, $\sigma_1(\omega)$, and of the corresponding dielectric function, $\epsilon_1(\omega)$, of Gd$_5$Si$_2$Ge$_2$ are displayed over a wide frequency range in figure 5.3 for the two polarizations, $E\|a$ and $E\|b$. Note that the general shapes and the trends of changes are quite similar for both directions. Both $\sigma_1(\omega)$ and $\epsilon_1(\omega)$ show a typical metallic behaviour, in the sense that

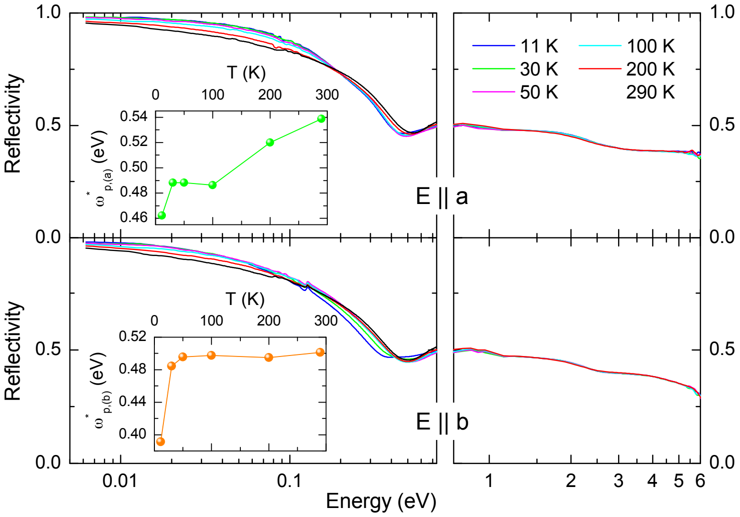

Figure 5.2: Reflectivity spectra of anisotropic $\mathbf{Gd_5Si_2Ge_2}$. - $R(\omega)$ for $E\|a$ (upper panel) and $E\|b$ (lower panel). Insets show the temperature dependence of the plasma edges $\omega^{\star}_{p,(a)}$ and $\omega^{\star}_{p,(b)}$, defined as the minimum of the reflectivity spectra.

the optical conductivity exhibits a Drude-like response and the dielectric function become negative as $\omega \rightarrow 0$. The sharp increase of $\epsilon_1(\omega)$ close to 1 eV is due to the proximity to the interband transitions. At high-temperature both spectra are quite broad with small frequency dependence. However as the temperature is lowered, the optical conductivity increases as $\omega \rightarrow 0$ leading to a narrowing of the zero-frequency mode. We also note that the optical conductivity spectra for both polarizations have similar interband transitions at about 1.6 eV and 3.6 for $E\|a$ and 1.5 eV and 3.3 eV for $E\|b$.

Most of the interesting changes in the optical conductivity of $Gd_5Si_2Ge_2$ occur in the infrared region at low-temperature far below T_C. This observation is in contrast with what we observed in FeGe and UGe_2 magnetic materials, where we could observe strong changes across the magnetic transition. In figure 5.4 we show a more detailed plot of the low-frequency optical conductivity at several temperatures along the a-and b-axes. For both polarizations $\sigma_1(\omega)$ is strongly frequency and temperature dependent. It is interesting to see that a strong depletion of the spectral weight occurs at low-temperature, which is stronger along the b-axis. Additionally there is a strong shift of the minimum position in the optical conductivity of about 0.1 eV to low-frequency, with decreasing temperature. We also see broad structure at 0.25 eV along the a-axis,

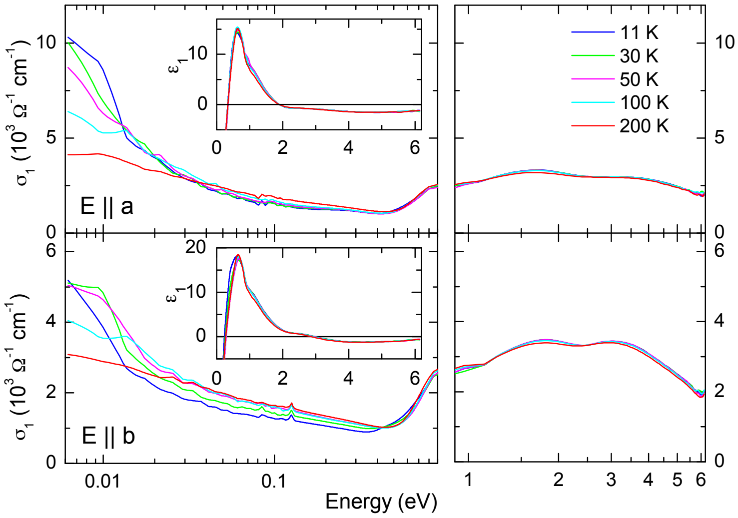

Figure 5.3: The optical conductivity and the dielectric function of anisotropic Gd$_5$Si$_2$Ge$_2$. - $\sigma_1(\omega)$ and $\epsilon_1(\omega)$ (insets) for the $E\|a$ (upper panel) and $E\|b$ (lower panel) as a function of frequency at several temperatures.

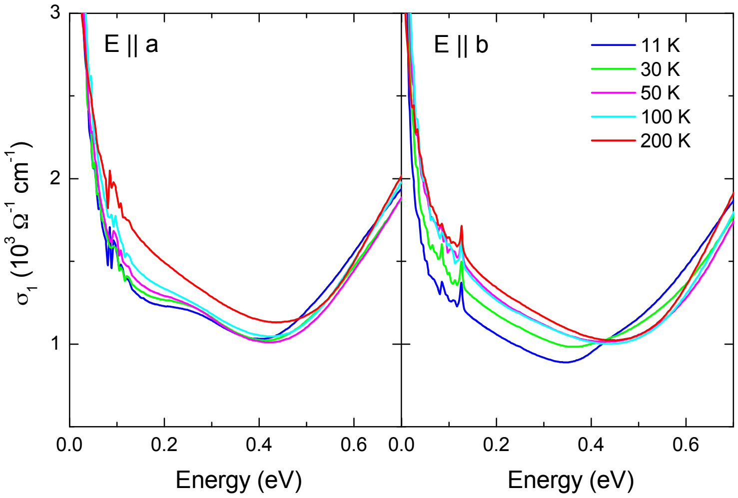

Figure 5.4: Low-frequency part of the optical conductivity spectra in Gd$_5$Si$_2$Ge$_2$. - Left panel: $\sigma_1(\omega)$ for the $E\|a$ and right panel: $\sigma_1(\omega)$ for $E\|b$.

which is probably an interband transition. We observe that this structure is not present in the 200 and 100 K curves, but only at low temperatures. In contrast, no such structure is present in this energy range along the b-axis. The structure at 0.12 eV from the reflectivity spectra for $E\|b$ appears as a sharp feature in the optical conductivity. No appreciable shifts of this peak are found as a function of temperature. Therefore we speculate that this structure may be attributed to an optical phonon mode. Additionally some small extra structures are seen near 0.08 eV, for both polarizations. They are due to the imperfect match between the far and mid-infrared measurements and should be ignored.

5.4 Comparison with band structure

The electronic structure of $Gd_5Si_2Ge_2$ has been studied theoretically [97] by local spin density approximation (LSDA) and local spin density approximation with on-site Coulomb (LSDA+U) band structure calculation. The standard LSDA approach places the Gd minority $4f$-bands at the Fermi level, as a result sharp peaks are observed in the density of states at the Fermi level. This incorrect position of the $4f$-bands reflects the difficulty of LSDA approximation to describe the strongly correlated nature of the Gd $4f$-electrons in this compound. To account for the on-site f-electron correlations, in the LSDA+U method the $4f$-electrons were considered partially localized. The Coulomb repulsion strongly influences the electronic structure of $Gd_5Si_2Ge_2$ and the $4f$ hole levels are completely unoccupied and well above the Fermi level, while the $4f$-bands are fully occupied and situated far below the Fermi level (about 8 eV).

Several band structure calculations have been reported for both monoclinic and orthorhombic phases of $Gd_5Si_2Ge_2$ [97, 98] but they are not all consistent with each other. The significant difference is the position of the interband transitions that are shifted by 1 eV. The major discrepancy is attributed to the different approximations used in the calculations. Figure 5.5 shows the total density of states of $Gd_5Si_2Ge_2$, in the low-temperature orthorhombic phase from Ref. [97]. The Gd $4f$-states are situated at the bottom of the Si and Ge s-states and do not influence the density of states near E_F.

Further insight into the band positions is given by the calculation of the optical conductivity from this band structure calculation. The optical conductivity spectra have been calculated using electric dipole matrix elements and averaged over all directions and broadened by convolution with a Lorentzian of 0.4 eV width [97]. In figure 5.6 we show the experimental, $\sigma_{1(a)}$ and $\sigma_{1(b)}$, together with the calculated, $\sigma_{1(calc.)}$, component of the optical conductivity [97] for the low-temperature orthorhombic phase. We see that the calculated curve reveals

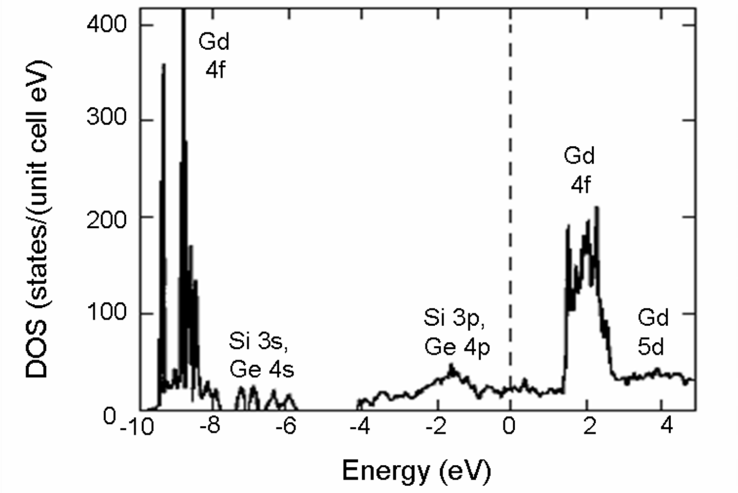

Figure 5.5: Total DOS of Gd$_5$Si$_2$Ge$_2$ in the LSDA + U approximation, adapted from Ref. [97]. - The density of states calculated for the low-temperature orthorhombic phase.

a structure similar to the experimental one. The calculated optical conductivity exhibits two peaks, at $\sim$ 1.8 eV and 5 eV, while experimentally we find a peak at 1.6 eV and a broad peak centered at 3.6 eV. The calculated peak at $\sim$ 1.8 eV may be identified as experimental peak at 1.6 eV. Additionally we observe interband transitions close to $\sim$ 3 eV, far below the theoretical maximum at 5 eV. But these transitions do not involve the empty or occupied $4f$-states. Finally, the transitions from the occupied $4f$ into the empty $5d$-bands should appear at much higher energy ($\sim$ 12 eV) then the upper limit of our spectra.

Recently, the dielectric function for the monoclinic phase was reported in Ref. [99]. Two peaks in the spectrum were observed: one at 2 eV for the b-axis and one broad peak at 2.7 for the a-axis. Contrary with what has been previously reported [99] we observe two peaks for both polarizations: at 1.5 eV and 3.3 eV along the b-axis and two peaks at 1.6 and 3.6 eV along a-axis (see figure 5.6). However in the previous measurements [99] only one peak for each direction is reported. We think that the difference between the previous results and ours can be explained by the different methods of surface preparation. Due to the fact that our sample was freshly polished and kept in a dry flow of nitrogen at ambient conditions, an oxide layer is unlikely to cause such changes. Verification has been made in order to check the effect of ambient pressure conditions in open air. For this we performed a measurement on the sample before and after switching off the flow of nitrogen. Under nitrogen flow the ellipsometric

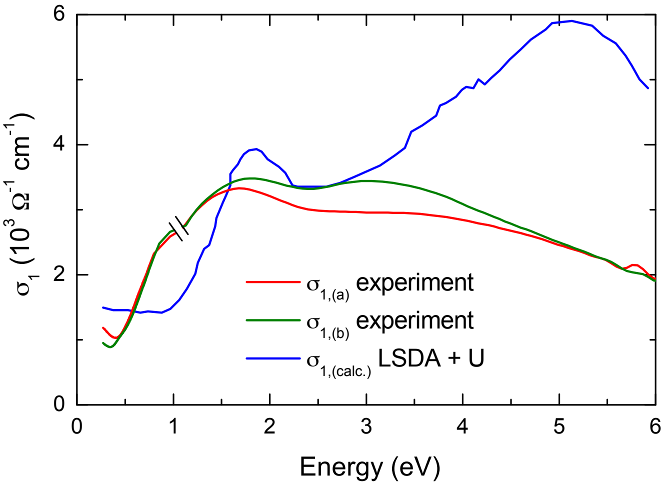

Figure 5.6: The experimental and calculated spectra of Gd$_5$Si$_2$Ge$_2$. - Red and green lines indicate the experimental spectra for $E\|a$ and $E\|b$, respectively. The interruption of the experimental curves at 1 eV is the result of slight mismatch between the two spectrometers. The blue line indicates the calculated spectra, reproduced from Ref. [97].

parameters (Δ and Ψ) are seen to be constant as a function of time. Once in open air significant changes are observed as a function of time, but the positions of the main features in the spectra seem to remain the same.

5.5 Spectral weight transfer

In order to further analyze the low-frequency optical conductivity spectra we calculate the spectral weight, which is defined as the integral of the optical conductivity up to a certain cutoff frequency:

$$N_{eff}(\omega) = \frac{2mV}{\pi e^2} \int_0^{\omega_c} \sigma_1(\omega) d\omega. \qquad (5.1)$$

Here ω_c is a cutoff frequency, m is the electron mass and V is the volume per unit cell calculated from the lattice parameter given in Ref. [93]. This relation plotted in figure 5.7 refers to the number of electrons that contribute to conduction below ω_c. For $\omega \to \infty$ this quantity is temperature independent and equals to the total number of electrons. We observe that the temperature distribution of the spectral weight for each polarization is very different. In particular as the temperature is decreasing, $N_{eff}(\omega)$ at low-frequency increases along the

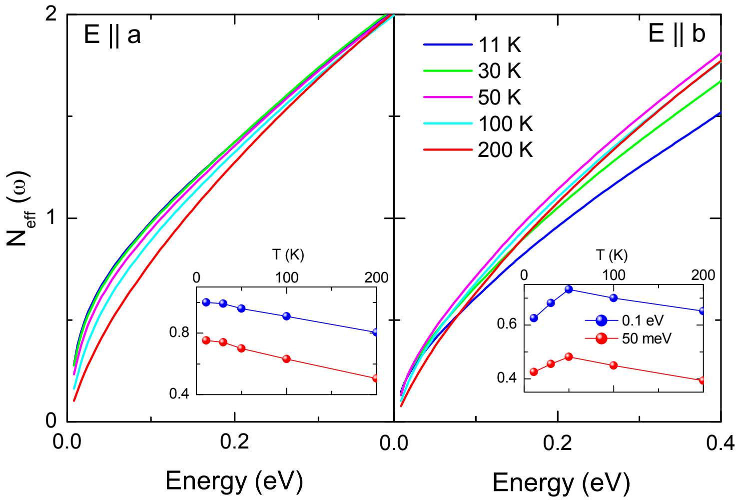

Figure 5.7: $N_{eff}(\omega)$ **versus frequency of Gd$_5$Si$_2$Ge$_2$.** - The effective numbers of electrons for the $E\|a$ (left panel) and $E\|b$ (right panel) derived from the integrated optical conductivity, $\sigma_1(\omega)$. The insets show $N_{eff}(\omega)$ versus temperature for two selected frequencies 0.1 eV and 50 meV, for the $E\|a$ (left panel) and $E\|b$ (right panel).

a-axis while the opposite behaviour is observed along the b-axis. This trend is better seen in the temperature dependence plotted in the inset in figure 5.7 for 50 meV and 0.1 eV. We see a moderate increase of $N_{eff}(\omega)$ as the temperature is decreasing for $E\|a$. However, we notice a clear decrease of $N_{eff}(\omega)$ at low-temperature for $E\|b$, which indicates a reduction of number of conduction electrons. This behaviour is consistent with the temperature dependence of the reflectivity spectra (see figure 5.2), which suggests the presence of a new phase transition at low-temperature. In addition for $E\|a$ above 0.3 eV the $N_{eff}(\omega)$ curves tend to merge. In other words, this tells us that a temperature distribution of the spectral weight occurs below 0.3 eV. In contrast the spectral changes extend up to much higher energy, up to 1 eV, for $E\|b$.

5.6 New phase transition

In figure 5.8 we show the temperature dependence of the reflectivity spectra for a few selected frequencies. Several aspects of the temperature dependence of the reflectivity spectra are interesting and unusual. First we note that upon cooling the sample, the reflectivity spectrum $R_b(\omega)$ goes through a slight maximum and strongly decreases below 45 K with the largest effect seen at 0.24 and 0.37 eV. Similar trend appears also in the $R_a(\omega)$ spectrum but the energy is slightly higher and the effect seems to be smaller then in the $R_b(\omega)$ spectrum. We also observe a sign change in the temperature-reflectivity spectra at 0.59 eV and, for both polarizations, $R(\omega)$ shows an increase below 45 K for $\omega > 0.49$ meV. The sharp changes in the reflectivity spectra, below 45 K, suggest the presence of a low-temperature state of matter which is qualitatively different from the ferromagnetic phase. The only other indication for a special low-temperature phase comes from a magnetoresistance experiment [100] where a small minimum was found near 44 K in the temperature dependence of a 4 T magnetic field. This effect was suggested to be due to the partially antifferomagnetic interactions in the Gd sublattices.

In order to obtain further insight into the nature of the observed low-temperature phase, we measured the resistivity and the magnetization on the same sample. However, no sign of an anomaly is observable in these quantities at 45 K, as can be seen from the figure 5.9. These observations rule out the possibility for an additional magnetic transition, because the magnetization is fully saturated. The scenario for a structural transition, for which one expects to see a clear signature in transport measurements can also be ruled out. It may be that the state of matter that occurs below 45 K is a crossover and not a true phase transition.

The low-temperature phase below 45 K is characterized by:

- Free carrier n/m^* about 20% reduced compared to T >45 K, as can be seen from figure 5.7 (inset, right panel);

- Reduced scattering rate, see figure 5.3 (lower panel), showing sudden narrowing of the Drude peak below 45 K;

- No change of ρ_{dc}, implying that $m\tau^* = m^*\tau$.

The latter observation implies a possible spin screening of the conduction electrons having their spin opposite to the net magnetization of the Gd states. These electrons can undergo processes whereby they flip their spin due to emission of a ferromagnetic magnon.

It is interesting to mention that there are another examples, like URu_2Si_2 [56] and UGe_2 [4], that show a phase transition of unknown nature at low-temperature. The common point between these materials and $Gd_5Si_2Ge_2$ is that the low-temperature *new* phase transition occurs within a magnetic phase.

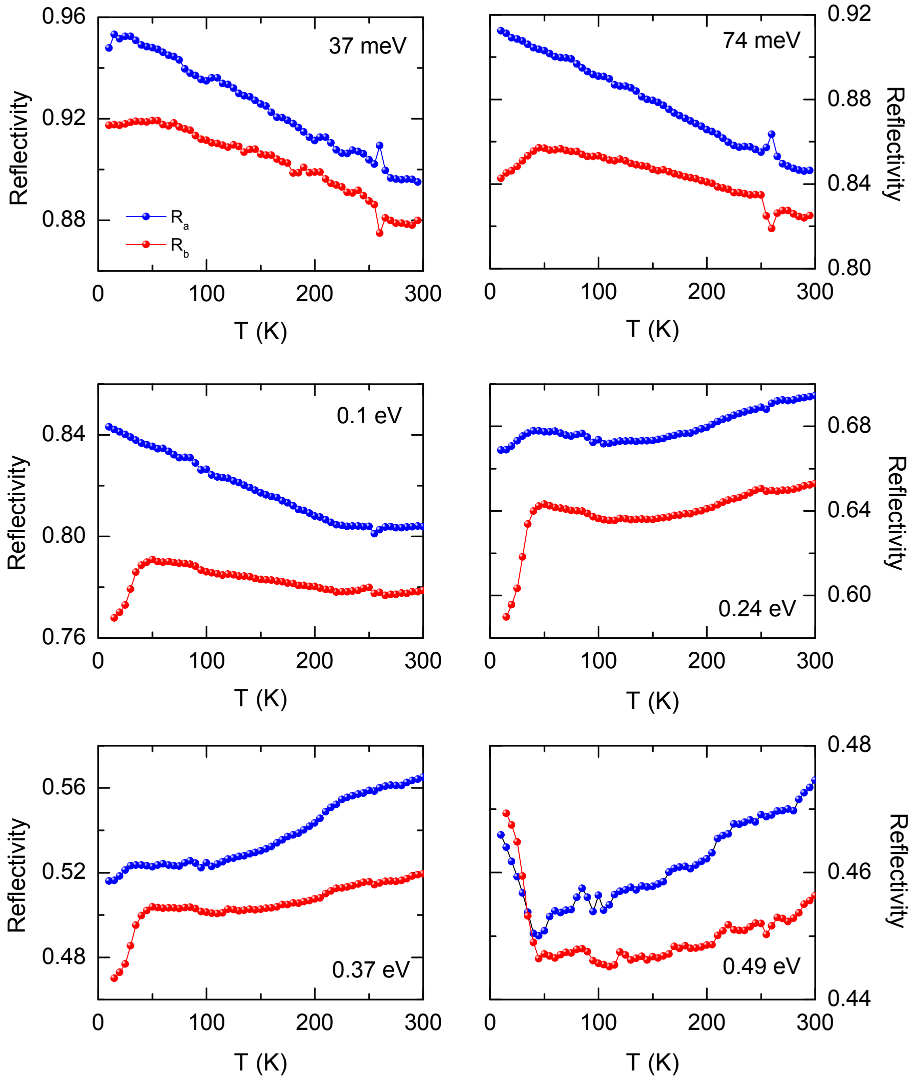

Figure 5.8: Temperature dependent reflectivity spectra. - $R_a(\omega)$ and $R_b(\omega)$ versus T for few distinct frequencies: 37 meV, 74 meV, 0.1 eV, 0.24 eV, 0.37 eV and 0.49 eV.

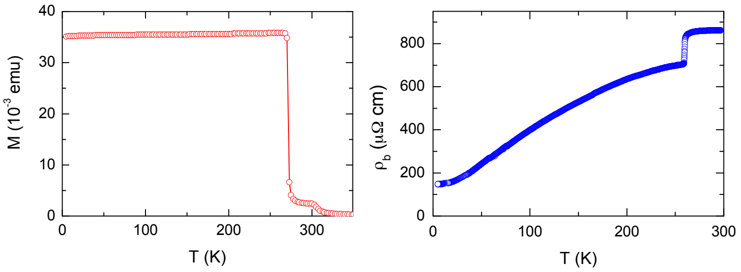

Figure 5.9: The magnetization and the resistivity of $Gd_5Si_2Ge_2$ as a function of temperature. - Left panel: magnetization versus temperature. Right panel: resistivity versus temperature.

5.7 Conclusions

In summary, we report an evidence for a new phase transition in the optical properties of anisotropic $Gd_5Si_2Ge_2$ system. The anisotropic optical conductivity is obtained as well as the dielectric function and the reflectivity as a function of frequency and temperature. The main result of our study is the temperature dependence of the reflectivity spectra, which shows a strong decrease at low-temperature, below 45 K, identified as a new state of matter. Another remarkable feature is the significant loss of spectral weight at low-temperature. It is worth noting that this transition appears at low-temperature far below the magneto-structural transition. Although sharp changes occur in the optical response, at low-temperature, the transport and magnetic measurements performed on the same sample show no sign of an anomaly. The present studies do not clarify the origin of this new phase, which remains to be unraveled by future work.

Chapter 6

The two colors of MgB_2

In this chapter, we present the anisotropic optical conductivity of MgB_2 between 0.1 and 3.7 eV at room temperature obtained on single crystals of different purity by spectroscopic ellipsometry and reflectance measurements. The bare (unscreened) plasma frequency ω_p is almost isotropic and equal to 6.3 eV, which contrasts some earlier reports of a very small value of ω_p. The data suggests that the σ-bands are characterized by a stronger electron-phonon coupling, λ_{tr}, but smaller impurity scattering, γ_{imp}, compared to the π-bands. The optical response along the boron planes is marked by an intense interband transition at 2.6 eV, due to which the reflectivity plasma edges along the a- and c-axes are shifted with respect to each other. As a result, the sample spectacularly changes color from a blueish-silver to yellow as the polarization is rotated from the in-plane direction towards the c-axis. The optical spectra are in good agreement with the published *ab initio* calculations. The remaining discrepancies can be explained by the relative shift of σ-bands and π-bands by about 0.2 eV compared to the theoretical band structure, in agreement with the de Haas-van Alphen experiments. The widths of the Drude and the interband peaks are both very sensitive to the sample purity.

6.1 Introduction

The discovery of superconductivity in MgB_2 [10] caused excitement in the physics community not only due to an unprecedentedly high T_c ($\sim$40 K) for a "conventional" electron-phonon superconductor, but also because it clearly shows the existence of two distinct gaps [11]; an intriguing phenomenon that, although addressed theoretically, had never been observed before. Magnesium diboride consists of graphite-like boron planes intercalated with Mg atoms as shown in figure 6.1. The metallic properties are determined by two distinct types of electronic bands: the strongly covalent almost 2D σ-bands formed by the hybridized sp_xp_y B orbitals and 3D π-bands made of p_z orbitals. The holes in the σ-bands are strongly coupled to the in-plane bond-stretching phonon modes, giving rise to a high electron-phonon coupling constant [101]. A remarkable implication of such a strong conduction band disparity is a multigap superconductivity: a large gap value on σ-bands and a small one on π-bands. Notably, the community has enjoyed a rapid advance in understanding the electronic structure and superconducting scenario of MgB$_2$, in contrast to the lengthy siege of the high-T_c problem in the cuprates.

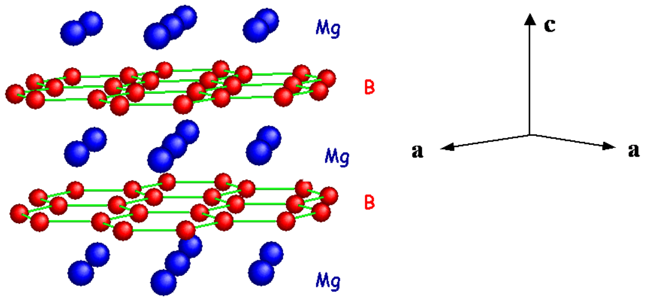

Figure 6.1: Crystal structure of MgB$_2$. - The boron atoms (red spheres) form graphite-like layers separated by hexagonal layers of Mg (blue spheres).

The early theoretical predictions of the electronic structure and the superconducting properties were soon confirmed by the isotope effect [102, 103], angle-resolved photoemission[104], de Haas-van Alphen (dHvA) [105], specific heat [106, 107, 108], tunneling measurements [109] and, recently, by the inelastic X-ray scattering [110]. Even though the far-infrared experiments [111, 112, 113, 114, 115, 116] have clearly shown the lowest of the superconducting gaps in agreement with the theory and other spectroscopic probes, the optical measurements so far demonstrated a rather poor reproducibility and equally poor consistency with the theoretical electronic structure. The most controversial issue is value of the Drude plasma frequency ω_p. While the theory predicts a high value of ω_p of $\approx$ 7 eV, which corresponds to about 1 conducting electron per unit cell, a number of groups [117, 112, 118, 119, 120, 121] reported a much smaller value of about 1.5 - 2.5 eV, corresponding to 0.15 electrons per cell. In Ref. [118], in addition to the narrow Drude peak, a broad continuum, which could contain the missing Drude spectral weight, was found below 1 eV. However, the existence of such a continuum was not reliably verified by other groups. Another inconsistency is related to the anisotropy of the plasma frequency. The calculations provide very close (within 5%) values of $\omega_{p,a}$ and $\omega_{p,c}$, which should be regarded, in fact, as a coincidence, because the plasma frequency of the carriers in the 2D σ-bands is strongly anisotropic. A study of the optical anisotropy of magnesium diboride was undertaken by Fudamoto and Lee[121] through the comparison of the reflectivity spectra measured on a mosaic of ab-oriented crystals and on a polycrystalline sample. They observed the in-plane reflectivity plasma edge at about 2 eV. The authors also suggested that an additional structure in the reflection of a polycrystal is due to the c-axis plasma edge at 2.2 eV. Thus the anisotropy ratio $\omega_{p,a}/\omega_{p,c} \approx 0.73$ was deduced, which is in contrast to the theoretical prediction.

The optically derived electron-phonon coupling constant λ_{tr} was also a subject of debate [117, 120, 122, 123]. Values of λ_{tr} ranging from 0.13 [117] to 1.5 [120] were reported. It was pointed out in Ref. [123] that the determination of λ_{tr} relies strongly on the plasma frequency, which is not yet well established. One should keep in mind that different values of the coupling constant for the σ- and π-bands are expected from the calculations [101] and observed in the dHvA experiment [105].

With a lack of large single crystals of MgB_2, especially along the c-axis, the optical measurements were done on polycrystalline samples [118, 116, 121], disoriented [120, 124] or ab-oriented [117, 114, 113] films as well as ab-oriented crystal mosaics [115, 121]. We believe that a large spread of the published optical results can be explained by (i) different purity levels of the samples used, (ii) experimental difficulties to extract the anisotropic complex conductivity from the standard measurements on such objects and (iii) a fast rate of surface degradation in air [118, 121].

6.2 Sample preparation

High-quality single crystals of MgB_2 have been grown using a cubic anvil technique via the peritectic decomposition reaction of the $MgNB_9$ and Mg at temperature up to 2000°C under a pressure of 30 - 35 kbar. The details of the crystal growth and extensive characterization are given elsewhere [125]. The measurements were done on two samples, referenced below as S1 and S2. The samples were grown under slightly different conditions. For the sample S1 the purity of Mg was 99.8%, while a 4N-pure (99.98%) magnesium was used in the second case. The maximum temperature of crystal growth was higher for the sample

S2 by about 80°C. The time at the highest temperature was 10 minutes for the first sample and 30 minutes for the second one. To characterize the samples a magnetization measurement was performed and plotted in figure 6.2. We see that T_c of both samples is close to 38 K although sample S2 shows a somewhat narrower transition and a larger field-cooled diamagnetic signal when compared to S1.

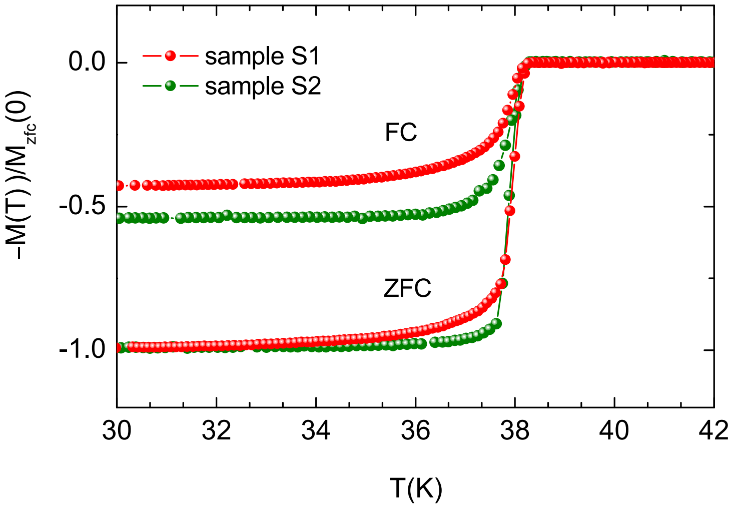

Figure 6.2: Magnetization versus temperature of MgB$_2$. - Magnetization measurements of the superconducting transition of the two single crystals of MgB$_2$ used in this work.

6.3 Experiment details

The dimensions ($a \times b \times c$) of the as-grown crystals were 0.7 × 0.5 × 0.27 mm^3 for S1 and 0.6 × 0.5 × 0.18 mm^3 for S2. We selected a thicker sample S1 to prepare the (ac) optical face, while sample S2 was used to measure on the (ab) face. Optical properties of MgB$_2$ at room temperature were obtained using spectroscopic ellipsometry at 0.75 - 3.7 eV and the reflectivity measurements in the infrared range from 0.1 to 0.85 eV. All measurements were done on individual freshly polished single crystals of different purity having no contact with the air. The faces were dry-polished using a 0.1 μm diamond abrasive, since the as-grown surfaces were not suitable for quantitative optical experiments. In all experiments, the sample was mounted on top of a cone and aligned with a laser.

As was noticed before [118, 121], the exposed surface of MgB$_2$ deteriorates quickly, largely due to the air moisture. In order to avoid the contamination, the samples were kept in a flow of dry nitrogen during and after the polishing until the end of the measurements. With this precaution, the optical characteristics did not change noticeably during the experiment. On the other hand, switching off the flow immediately affected the optical signal, as shown below.

The high-frequency spectra were collected using a Woollam VASE32 ellipsometer while the sample was kept in a flow of dry nitrogen. The in-plane $\epsilon_a(\omega) = \epsilon_{1,a}(\omega) + 4\pi i\sigma_{1,a}(\omega)/\omega$ and the c-axis $\epsilon_c(\omega) = \epsilon_{1,c}(\omega) + 4\pi i\sigma_{1,c}(\omega)/\omega$ components of the complex dielectric tensor were both extracted directly from the measurements on the ac-surface of the sample S1, using two orthogonal crystal orientations and three angles of incidence. For the sample S2, only the in-plane optical functions $\epsilon_{1,a}(\omega)$ and $\sigma_{1,a}(\omega)$ were derived from the measurement on the ab-plane, using the c-axis data from the sample S1 to correct for the admixture of the out-of-plane component. The details of the recovery of $\epsilon_a(\omega)$ and $\epsilon_c(\omega)$ from the ellipsometric output are given below.

The reflectivity, $R(\omega)$, was measured with a polarizer in the range 0.1 - 0.85 eV at a near-normal angle of incidence using a Fourier transform spectrometer Bruker 66/v. The sample was inside a vacuum chamber of a cryostat. A gold layer was evaporated *in-situ* on the crystal surface to get a reference signal. We reconstructed the full reflectivity spectrum using the ellipsometrically determined dielectric functions in the optical range:

$$R_\nu(\omega) = \left| \frac{1 - \sqrt{\epsilon_\nu(\omega)}}{1 + \sqrt{\epsilon_\nu(\omega)}} \right|^2, (\nu = a, c). \tag{6.1}$$

The spectra from two regions were combined in order to obtain the complex dielectric function in the whole spectral range, as described in Chapter 2.

6.4 Determination of $\epsilon_a(\omega)$ and $\epsilon_c(\omega)$ from ellipsometry

As we pointed out in Chapter 2 ellipsometry provides two parameters ψ and Δ, related to the ratio of reflection coefficients for the p- and s-polarized light:

$$\rho = r_p/r_s = \tan\psi \exp(i\Delta), \tag{6.2}$$

where r_p and r_s are given by the Fresnel formulas expressed in Eq. 2.17. In the case of optically uniaxial MgB$_2$ ($\epsilon_a = \epsilon_b \neq \epsilon_c$) three different orientations (xyz) are possible: (aac), (aca) and (caa) as shown in figure 6.3.

On the sample S1 we did ellipsometry in the orientations (caa) and (aca). This yields four independent quantities ψ_{aca}, Δ_{aca}, ψ_{caa} and Δ_{caa} at every photon energy and every chosen angle of incidence. Since each of these functions

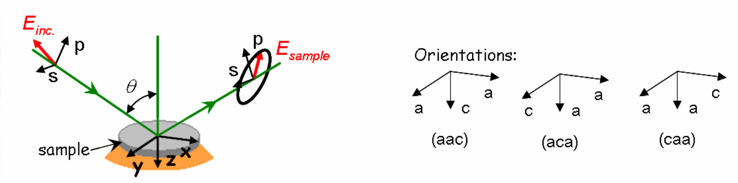

Figure 6.3: Principle of ellipsometry and sample geometries. - The general configuration of ellipsometric experiment (left panel) and the three specific sample orientations used in this work (right panel). The axes x, y and z are assumed to be along the principal axes of the dielectric tensor of the sample.

depends on the four values $\epsilon_{1,a}$, $\epsilon_{2,a}$, $\epsilon_{1,c}$ and $\epsilon_{2,c}$, the latter ones can be obtained by the numerical inversion of the four Fresnel equations. This procedure, when applied to three different angles of incidence (60°, 70° and 80°), gave close results. In order to improve the accuracy of the output, we determined by the least square fitting the values of $\epsilon_{1,a}$, $\epsilon_{2,a}$, $\epsilon_{1,c}$ and $\epsilon_{2,c}$ that render the best match to the measured ellipsometric parameters at all mentioned angles of incidence simultaneously. The experimental and fitting curves for the sample S1 for the orientations (aca) and (caa) are shown in figure 6.4.

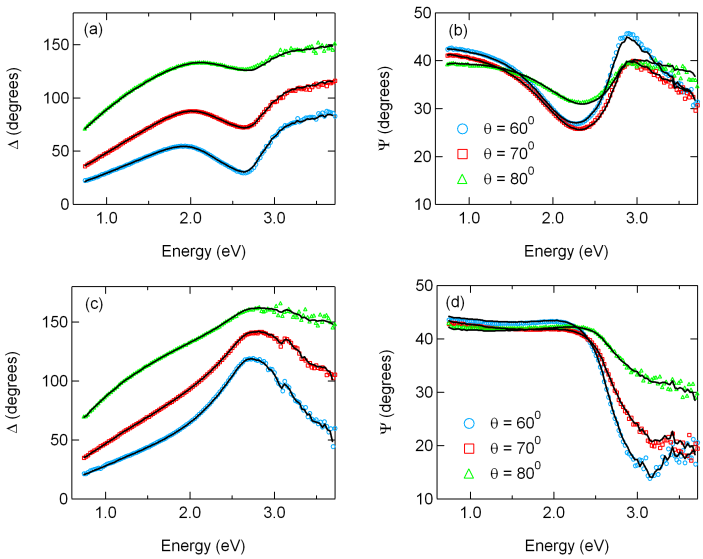

Figure 6.4: Ellipsometric spectra measured on sample S1. - (a) Δ and (b) ψ for the orientation (aca), (c) Δ and (d) ψ for the orientation (caa) (see figure 6.3), for three angles of incidence (60°, 70°, and 80°). Symbols are the measurement results, the solid lines correspond to the fit as described in the text.

The second experiment was done on the sample S2 in the orientation (aac). The corresponding spectra of ψ_{aac} and Δ_{aac} for the same three angles of incidence are shown in figure 6.5. These data, taken alone, are not sufficient to extract both ϵ_a and ϵ_c independently. Since ψ_{aac} and Δ_{aac} are not very sensitive to the value of ϵ_c except close to the screened plasma frequency (according to Aspnes approximation) [126], we extracted $\epsilon_a(\omega)$, assuming that $\epsilon_c(\omega)$ is the same as the sample S1. One should realize that this introduces some uncertainty, because the samples S1 and S2 might have somewhat different c-axis dielectric functions. This uncertainty is negligible below 2 eV, but somewhat enhanced close to the c-axis plasmon at 2.6 eV. The best fit of ψ and Δ is given by the solid lines in figure 6.5.

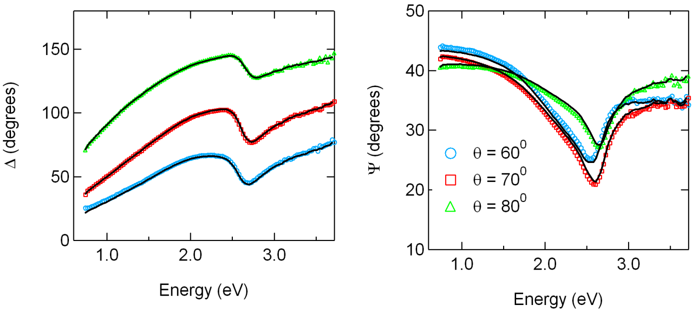

Figure 6.5: Ellipsometric spectra measured on sample S2. - Δ (left panel) and ψ (right panel) for three angles of incidence (60°, 70°, and 80°) in the orientation (aac). Symbols are the measurement results, the solid lines correspond to the fit as described in the text.

We are aware of the fact that the surface degrades in air very fast after polishing. In order to check this problem we measured the ellipsometric parameters Δ and Ψ as a function of time. Figure 6.6 shows that the ellipsometric parameters are affected immediately when a surface is exposed to air, due to the formation of a contamination layer. On the other hand, the flow of dry nitrogen efficiently preserves the surface quality. Analysis of the contaminated layer reveals important oxygen concentration, suggesting that this layer is most likely MgO. One likes to know how much the systematic errors of the surface degradation contribute to the optical constants. Indeed from the time dependence of the optical parameters Ψ and Δ one can estimate the error bars caused by the surface deterioration during the measurement. For example, from figure 6.6 one can see that the change of Δ and Ψ at 1.5 eV during the period of measurement does not exceed 0.5 degrees. We have similar time dependencies of ellipsometric parameters for several photon energies. The effect of this change

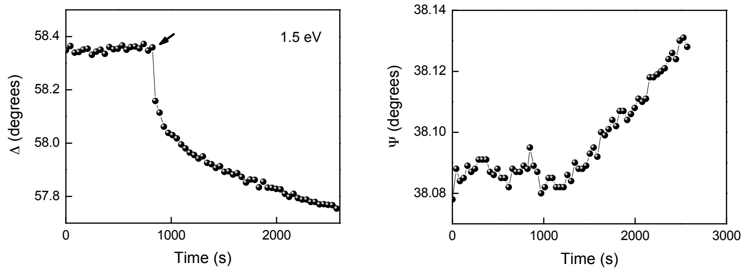

Figure 6.6: The effect of the exposure to the air on the optical properties of MgB$_2$. - The time dependence of ellipsometric parameters Δ and Ψ at 1.5 eV is shown (sample S1, geometry (caa), angle of incidence 70°). Initially the sample was kept in a flow of dry nitrogen, which was switched off at the moment designated by the arrow.

on the optical spectra turns out to be negligible. Thus the possible presence of the minority phases cannot explain the difference between the optical properties of the samples S1 and S2 presented below.

6.5 Optical spectra and plasma frequency

Figure 6.7 shows the anisotropic reflectivity, $R(\omega)$, optical conductivity, $\sigma_1(\omega)$ and the dielectric function, $\epsilon_1(\omega)$, measured on sample S1. Qualitatively, both in-plane and c-axis spectra exhibit a similar metallic behaviour, characterized by a reflectivity plasma edge, a Drude peak in $\sigma_1(\omega)$ and negative $\epsilon_1(\omega)$. However, one can see a strong anisotropy. The in-plane reflectivity shows a broad plasma edge at about 2 eV. The dielectric function $\epsilon_{1,a}(\omega)$ almost reaches zero at the same frequency, but then it varies non-monotonically while remaining negative at least up to 3.7 eV. In contrast, the c-axis plasma edge is significantly sharper and is higher in energy by about 0.5-0.6 eV. Correspondingly, $\epsilon_{1,c}(\omega)$ behaves monotonically and crosses zero at $\omega^*_{p,c} \approx 2.6$ eV. These results agree with the previous findings of Fudamoto and Lee [121] who obtained a plasma edge at about 2 eV on a mosaic of ab-oriented crystals. Although no direct reflectivity measurements for $E \parallel c$ were reported so far, the same authors suggested[121] that the additional step-like structure at 2.7 eV in the reflectivity of polycrystalline samples comes from the c-axis plasma edge. The present study fully confirms this assignment. The in-plane optical conductivity $\sigma_{1,a}(\omega)$ shows an intense interband peak at $\sim$ 2.6 eV, which is totally absent in the $\sigma_{1,c}(\omega)$ (figure 6.7(b). Its origin will be discussed below. Since this peak is close to the screened plasma frequency, it broadens the plasma edge and shifts it to lower

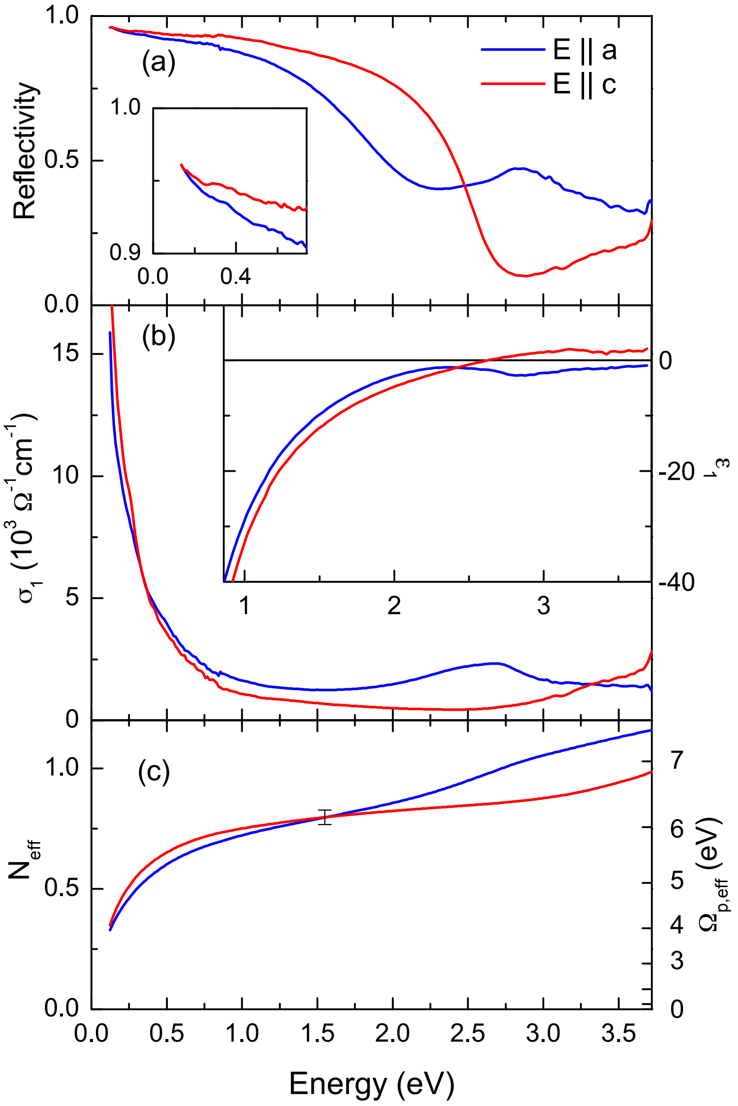

Figure 6.7: Optical anisotropic spectra of MgB_2 at 300 K derived from the ellipsometry and reflectivity measurements on the sample S1. - (a) The near-normal incidence reflectivity, (b) the optical conductivity and the dielectric function, (c) the effective number of carriers and the effective plasma frequency. The a-axis and the c-axis spectra are shown by the blue and red lines, respectively.

frequencies by providing an additional screening of the charge carriers. It is also responsible for a non-monotonic behaviour of $\epsilon_{1,a}(\omega)$ at higher frequencies and even for a structure in $R_a(\omega)$ above 3 eV, which resembles a "second" plasma edge.

Figure 6.7(c) displays the partial sum rule (effective number of carriers) function:

$$N_{\text{eff}}\,(\omega) = \frac{2mV_c}{\pi e^2}\int_0^{\omega}\sigma_1(\omega')d\omega', \tag{6.3}$$

where m is the free electron mass, V_c = 28.9 Å^3 is the unit cell volume, e is the electron charge, and the corresponding effective plasma frequency:

$$\Omega_{\text{p,eff}}(\omega) = \left[8\int_0^{\omega}\sigma_1(\omega')d\omega'\right]^{1/2}. \tag{6.4}$$

Since the integration of $\sigma_1(\omega)$ has to start from zero-frequency, while the optical data are taken down to 100 meV, one has to be vigilant about the error bars involved. Fortunately, the fact that the dielectric function obtained by the method used [38] satisfies the KK relations and describes both $\epsilon_1(\omega)$ and $\epsilon_2(\omega)$ at high frequencies poses fairly tight bounds [shown in figure 6.7(c)] on the allowed values of N_{eff}. One can see that at the photon energy of 1.7 eV, which is high enough to comprise most of the intraband spectral weight, but below the interband peak at 2.6 eV, N_{eff} is about 0.8 for both polarizations, which corresponds to a plasma frequency of 6.3 eV. A more rigorous estimate of the ω_p which take into account the broadening of the Drude peak, as described below, gives almost the same value of the plasma frequency (see Table 6.1). This is in contrast with the conclusion of Ref. [121] about a strong anisotropy of the plasma frequency, based on the different positions of the reflectivity plasma edge for the two polarizations. The anisotropy of the reflectivity plasma edge is caused by extra screening due to the in-plane interband transition at 2.6 eV and not by the strong anisotropy of the unscreened plasma frequency.

It is interesting to compare the in-plane optical properties of the two samples (S1 and S2), which were prepared under different conditions and have presumably slightly different impurity levels (see figure 6.8). One can see that the two most prominent features of the optical conductivity: i) the Drude peak and ii) the 2.6 eV interband peak are significantly sharper in sample S2. As a result, the reflectivity plasma edge is also sharper and the "double-plasmon" structure in $R_a(\omega)$ is more pronounced than in sample S1. One should keep in mind that sample S2 was prepared from a more pure magnesium, and it shows a sharper superconducting transition (figure 6.2). This suggests that even a small impurity

Table 6.1: Model parameters which give the best match to the measured optical spectra of MgB$_2$ at 300 K and the ratio $\rho_a(300K)/\rho_a(40K)$ from Ref. [127], as described in the text. Parameters, marked by *, were fixed to the values given by the band calculations.

Parameter	ab-plane	c-axis
$\omega_{p,\sigma}$	4.14* eV	0.68* eV
$\omega_{p,\pi}$	4.72 eV	6.31 eV
$\omega_{p,tot}$	6.28 eV	6.35 eV
$\gamma_{\sigma imp}$	12.4 meV	
$\gamma_{\pi imp}$	85.6 meV	
ω_1	2.60 eV	3.92 eV
S_1	1.79	1.7
γ_1	1.11 eV	1.51 eV
ω_2	8.57 eV	-
S_2	6.81	-
γ_2	100.2 eV	-
ϵ_∞	3.31	3.07

level (about 0.2% in this case) affects significantly optical and transport properties of MgB$_2$.

The close values of $\epsilon_{1,a}(\omega)$ for the two samples suggest that their in-plane plasma frequencies are similar, although the N_{eff} is slightly higher for sample S1, which could be related to a stronger broadening of the interband peaks.

6.6 Extended Drude analysis

The extended Drude model has been commonly used to analyze interactions in electronic systems. In this formalism, the frequency dependent scattering rate, $1/\tau(\omega)$, and effective mass, $m^*(\omega)/m$, are derived from the measured complex dielectric function:

$$\frac{m^*(\omega)}{m} + \frac{i}{\omega\tau(\omega)} = \frac{\omega_p^2}{\omega^2(\tilde{\epsilon_\infty} - \epsilon(\omega))}. \tag{6.5}$$

The only parameters of this conversion are the total Drude plasma frequency ω_p and the high-frequency dielectric constant $\tilde{\epsilon}_\infty$, due to all contributions other than the conduction electrons. Both $1/\tau(\omega)$ and $m^*(\omega)/m$ have a direct microscopic interpretation in the context of the electron-phonon interaction. One

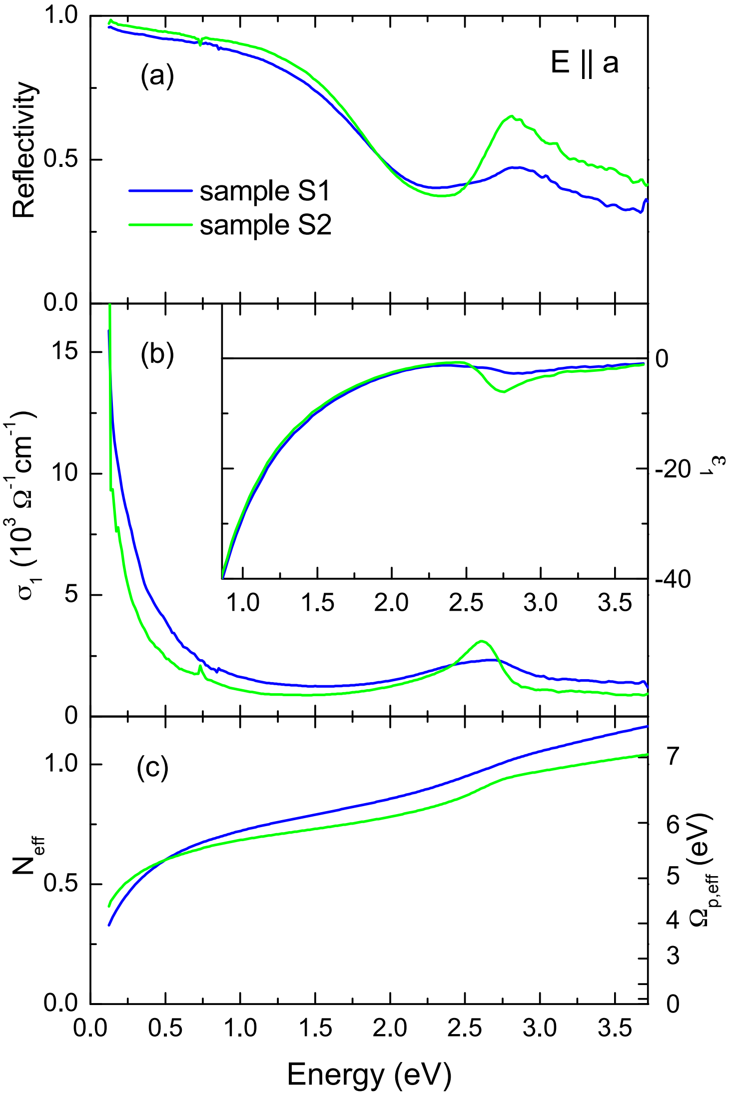

Figure 6.8: Comparison of the in-plane optical spectra measured on different samples. - The same types of spectra are presented as in figure 6.7. The spectra of samples S1 and S2 are shown by the blue and green lines, respectively. Sample S2 has presumably a smaller concentration of impurities than sample S1.

should keep in mind, however, that the model assumes that only one type of carrier contributes to the Drude response. In the case of MgB_2, which has two distinct systems of bands (σ and π), the scattering rate and the effective mass obtained by equation 6.5 should be regarded as an averaged value of contributions from each band. Figure 6.9 (symbols) shows $1/\tau(\omega)$ and $m^*(\omega)/m$ for the in-plane and the c-axis directions, measured on the sample S1. We took

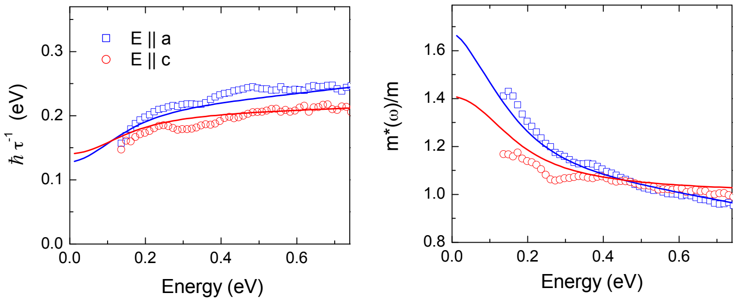

Figure 6.9: Extended Drude analysis of the optical conductivity of MgB_2 (sample S1) at 300 K along the in-plane and the c-axis directions. - The symbols are the data, the solid curves show the two-component fit as described in Section 6.8.

the values $\omega_{p,a}$ = 6.28 eV, $\omega_{p,c}$ = 6.35 eV, $\tilde{\epsilon}_{\infty,a}$ = 11.9, $\tilde{\epsilon}_{\infty,c}$ = 4.77, which are suggested by the data fitting in Section 6.8 (see Table 6.1). The value of $\tilde{\epsilon}_{\infty}$ here is given by the sum of ϵ_{∞} in the Table 6.1 and the oscillator strengths S_i of the Lorentz oscillators. The solid curves in figure 6.9 were calculated using the results of the fit described in Section 6.8. One can see that the scattering rate and the mass renormalization are larger for the in-plane direction. It is worth mentioning that the σ-bands with a cylinder-like Fermi surface must have a small electromagnetic response along the c-axis, while the π-bands are expected to have comparable contributions in both directions. The present result thus suggests that the electron-phonon coupling is stronger in the σ-bands. This is in agreement with the first-principle calculations of Kong *et al.* [101], who found that the total strength of the electron-phonon interaction is dominated by the coupling of the σ-holes to the bond-stretching optical phonons. A quantitative analysis of the electron-phonon interaction must take into account the multi-band electronic structure.

6.7 Electron-phonon coupling and interband transitions

A deeper insight can be attained by the comparison of the optical data with the existing first-principle calculations of the band structure and electron-phonon interaction. One can compute the dielectric function, assuming that the intraband optical conductivity is formed by the additive contributions of carriers in the σ- and the π-bands. The two bands are characterized by different electron-phonon (Eliashberg) transport functions $\alpha^2_{tr}F(\omega)$ and impurity scattering rates γ_{imp}. Intraband optical response can be calculated using finite-temperature memory-function formalism for electron-boson interaction [128]. The total conductivity is a sum of the intraband, interband (ϵ^{IB}) and core-electron (ϵ_∞) responses:

$$\epsilon_\nu(\omega) = \sum_{\beta=\sigma,\pi} \frac{\omega^2_{p,\nu\beta}}{-\omega[\omega + iM_\beta(\omega,T)]} + \epsilon^{IB}_\nu(\omega) + \epsilon_{\nu\infty} \qquad (\nu = a, c). \tag{6.6}$$

The contribution of each of the two bands is determined by its respective anisotropic plasma frequency ($\omega_{p,a}$, $\omega_{p,c}$) and the memory function [128]:

$$M_\beta(\omega,T) = \gamma_{\beta imp} - 2i\int_0^\infty d\Omega\ \alpha^2_{tr}F_\beta(\Omega)K\left(\frac{\omega}{2\pi T}, \frac{\Omega}{2\pi T}\right), \tag{6.7}$$

where

$$\begin{aligned} K(x,y) = \frac{i}{y} \quad + \quad & \frac{y-x}{x}[\psi(1-ix+iy) - \psi(1+iy)] + \\ & \frac{y+x}{x}[\psi(1-ix-iy) - \psi(1-iy)], \end{aligned}$$

and $\psi(x)$ is a digamma function.

All the ingredients to compute $\epsilon(\omega)$, except the impurity scattering rates $\gamma_{\sigma,imp}$ and $\gamma_{\pi,imp}$, which depend on the level and the nature of the impurities (substitutions, vacancies, dislocations etc.), are provided by the *ab initio* LDA calculations.

The spectra of the interband optical conductivity $\sigma^{IB}_1(\omega)$ obtained by different groups using the LMTO [129, 130], full-potential LAPW [131] and time dependent DFT [132] methods, although showing some differences, are close to each other. In particular, we took the interband conductivity spectra, presented in Ref. [118] (figure 5) on the base of the full-potential LAPW method [131], and computed the corresponding dielectric function $\epsilon_1^{IB}(\omega)$ by the KK transformation. The plasma frequencies reported by different groups [131, 129, 130] are also close to each other. We used the values $\omega_{p,a\sigma}$ = 4.14 eV, $\omega_{p,a\pi}$ = 5.89 eV, $\omega_{p,c\sigma}$ = 0.68 eV and $\omega_{p,c\pi}$ = 6.85 eV [131, 119].

The *ab initio* calculated electron-phonon interaction functions were presented in Ref. [101]. We used effective interaction functions for the two bands $\alpha_{tr}^2 F_\sigma(\omega) \equiv \alpha_{tr}^2 F_{\sigma\sigma}(\omega) + \alpha_{tr}^2 F_{\sigma\pi}(\omega)$ and $\alpha_{tr}^2 F_\pi(\omega) \equiv \alpha_{tr}^2 F_{\pi\pi}(\omega) + \alpha_{tr}^2 F_{\pi\sigma}(\omega)$ from the Refs. [101, 108]. The electron-phonon coupling constant $\lambda_{tr} = 2\int_0^\infty d\Omega\ \alpha_{tr}^2 F(\Omega)/\Omega$ is calculated to be about 1.1 for the σ-bands and 0.55 for the π-bands.

The calculated optical spectra are presented in figure 6.11. Here the scattering rates $\gamma_{\sigma imp}$ = 12.4 meV and $\gamma_{\pi imp}$ = 85.6 meV were taken; this choice is substantiated by the data fitting in the next Section. Comparing figures 6.7 and 6.11, one can notice a remarkable overall agreement and even a reasonable quantitative match. We begin with the interband transitions. Both theoretical and experimental interband optical conductivities show a very strong anisotropy. Notably, the theory predicts no sizeable optical intensity along the c-axis of the interband transitions below 4 eV, whereas there are two low-lying peaks at 0.35 eV (denoted as A) and 2.4 eV (denoted as B) for polarization parallel to the boron planes (see the dotted blue curve in figure 6.11(b). In order to identify the interband transitions we refer to the band structure dispersion, indicating the bands contributing to the structures of the optical conductivity spectra, sketched in figure 6.10. The calculated optical transitions are denoted as A, B and C and shown as arrows. The 2.4 eV peak (denoted as B) is due to a transition from the σ-band to the π-band close to the M-point, where a van Hove singularity

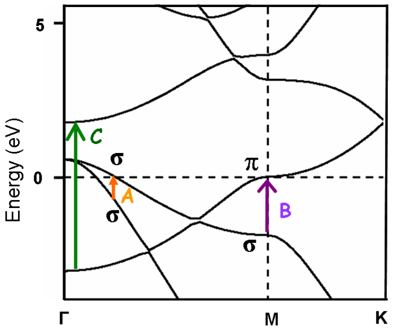

Figure 6.10: Band structure of MgB$_2$ along some high symmetry lines, adapted from Ref. [11]. - The optical interband transitions corresponding to the calculated peaks are denoted by arrows.

strongly enhances the density of states [131]. The peak at 0.35 eV (denoted as A) corresponds to the transition between two close σ-bands. The σ carriers are localized within the boron planes, which explains why these two transitions are optically very weak along the c-axis.

Obviously, a strong peak in the experimental spectrum along the a-axis at 2.6 eV matches the theoretical peak at 2.4 eV (denoted as B). The discrepancy in the peak position suggests that the separation between σ-band and π-band is about 0.2 eV larger than predicted by the theory. It is remarkable [133], that the same shift brings the results of the dHvA experiments [105] in MgB$_2$ close to theoretical predictions [133, 119].

According to the calculation, the $\sigma \rightarrow \sigma$ transition at 0.35 eV (denoted as A) should manifest itself as a small dip of about 1% in the in-plane reflectivity spectrum [see inset in figure 6.11(a)]. Such a dip is not observed in the experimental spectra displayed in figure 6.7(a). This peak may thus be shifted to even lower frequencies or be heavily overdamped. The first possibility is consistent with a shift of the σ-bands with respect to the Fermi energy compared to the calculation, as proposed in Ref. [133]. The broadening can be caused by the interaction with the conduction electrons, since the energy of this transition is within the width of the Drude peak. Nevertheless such peak was reported in Ref. [134] at $\sim$ 0.47 eV and found that it shifts to lower energy with aluminum and carbon doping. However this effect does not seem be present in other optical studies. To clarify this point more experiments are needed.

A very intense sharp peak in the out-of-plane conductivity $\sigma_{1,c}(\omega)$ is expected around 5 eV (denoted as C) [129, 118, 132]. This excitation was closely studied in Ref. [132] by the time dependent density functional method. In the band picture, it comes from a transition between almost parallel bands. From the real-space point of view, this mode involves charge fluctuations between B and Mg sheets, dynamically screened by the intraband transitions [132]. As a consequence, a sharp plasma mode at 2.5 eV should emerge. Although 5 eV is beyond our experimental range, there is a sizeable increase of $\sigma_{1,c}(\omega)$ above 3 eV, which can be a low-energy tail of this mode. The c-axis plasmon is at 2.6 eV, which is only slightly higher than the calculated value ($\sim$ 2.5 eV). This is in agreement with the inelastic X-ray scattering experiment [110].

The shape and the width of the Drude peak agree well with the experiment, which suggests that phonons and impurities are the main factors of electron scattering. The integrated spectral weight $N_{\text{eff}}(\omega)$ grows faster according to the calculations, especially for the in plane response. This indicates that the theory overestimates the value of the plasma frequency.

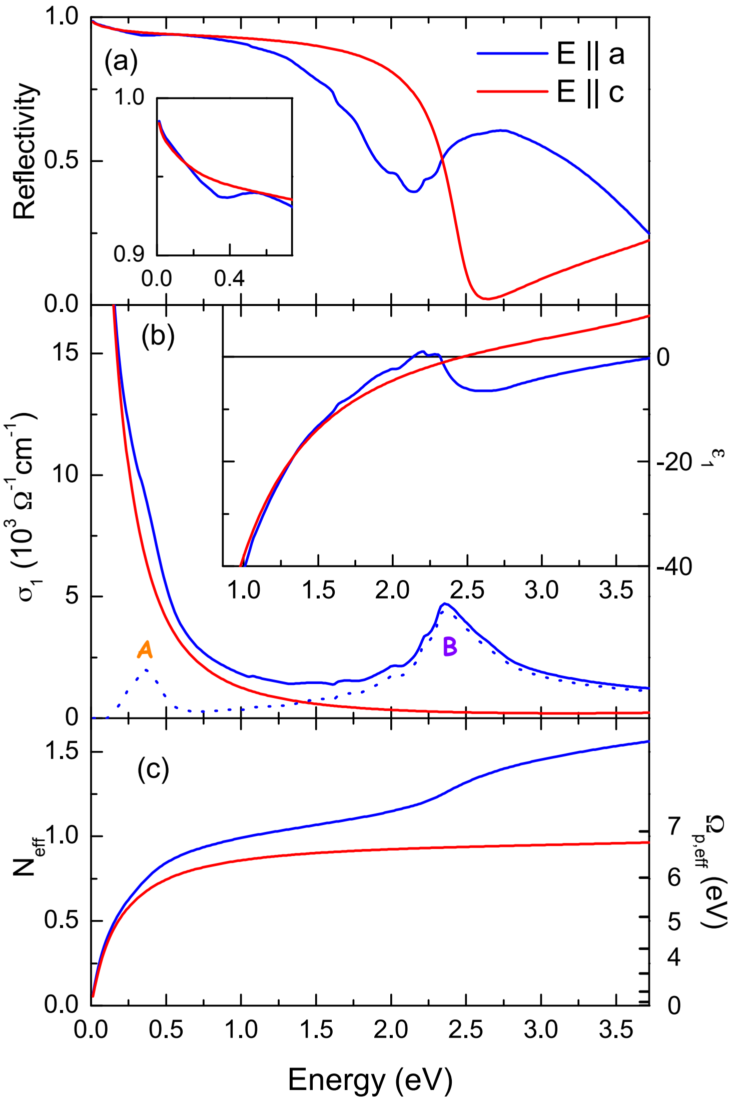

Figure 6.11: Theoretical optical spectra of MgB_2 at 300 K. - The anisotropic optical spectrum was calculated using the results of the published first-principle studies [131, 101] as described in the text. The same types of spectra are shown as in figure 6.7. Additionally, the interband contribution along the a-axis is presented in (b) as a dotted blue line and the interband transitions marked as A and B. The interband conductivity along the c-axis is negligible in the shown energy range.

6.8 Two-band fitting of the spectra

The overall good agreement between the experimental and calculated data allows us to use the chosen model to fit the spectra, treating the plasma frequencies and scattering rates as adjustable parameters. We could achieve a satisfactory least-square fit of reflectivity $R(\omega)$ in the mid-infrared and $\epsilon_1(\omega)$ and $\sigma_1(\omega)$ at higher frequencies using formulas (6.6) and (6.7) as it is shown in figure 6.12. The corresponding parameter values are given in Table 6.1. It turns out that leaving all four plasma frequencies adjustable makes the fitting procedure under-determined. Therefore, assuming the 2D nature of the σ-band, we fixed the plasma frequencies of the σ-band to the values given by *ab initio* calculations, and left only the total in-plane and c-axis plasma frequencies $\omega_{p,tot}^2 = \omega_{p,\sigma}^2 + \omega_{p,\pi}^2$ adjustable. Another assumption was that the *ab initio* calculations [101, 108] correctly describe the electron-phonon functions $\alpha_{tr}^2 F_{\sigma,\pi}(\omega)$.

We modeled the interband conductivities by Lorentz oscillators ($\nu = a, c$):

$$\epsilon_{\nu}^{IB}(\omega) = \sum_i \frac{S_{\nu i}\omega_{\nu i}^2}{\omega_{\nu i}^2 - \omega^2 - \gamma_{\nu i}\omega}, \tag{6.8}$$

with adjustable frequency $\omega_{\nu i}$, oscillator strength $S_{\nu i}$ and width $\gamma_{\nu i}$. Keeping in mind the two interband peaks below 3 eV predicted by the theory, we put two Lorentzians to model $\epsilon_a^{IB}(\omega)$. Only one oscillator term above 3 eV was taken for $\epsilon_c^{IB}(\omega)$.

One can see that the bare plasma frequencies $\omega_{p,\sigma}$ and $\omega_{p,\pi}$ are almost the same and equal to 6.3 eV, which confirms our previous estimate based on the partial sum rule [figure 6.7(c)]. This value is much higher compared to previous reports [117, 112, 118, 119, 120, 121] of 1.5-2.5 eV. Thus, the discrepancy with the theoretical value of 7 eV is likely to be much less than it was thought before. However, the current mismatch is not negligible since it results in about 20-25% deviation of the Drude spectral weight. It is important to mention that the extremal orbit areas in the de Haas-van Alphen experiment [105] on both σ and π Fermi surfaces are also somewhat smaller than predicted by theory [119, 133]. It was pointed out [133] that the discrepancy can be removed by a shift of the σ-bands downward by about 115 meV and the π-bands upward by 125 meV. This is in perfect agreement with our observation of the mismatch of 0.2 eV in the position of the 2.6 eV peak, as it is mentioned before. This also qualitatively explains the smaller value of the plasma frequency.

The impurity scattering rate in the π-band $\gamma_{\pi imp}$ is about 85 meV. Since the π-electrons have rather strong optical spectral weight and a modest electron-

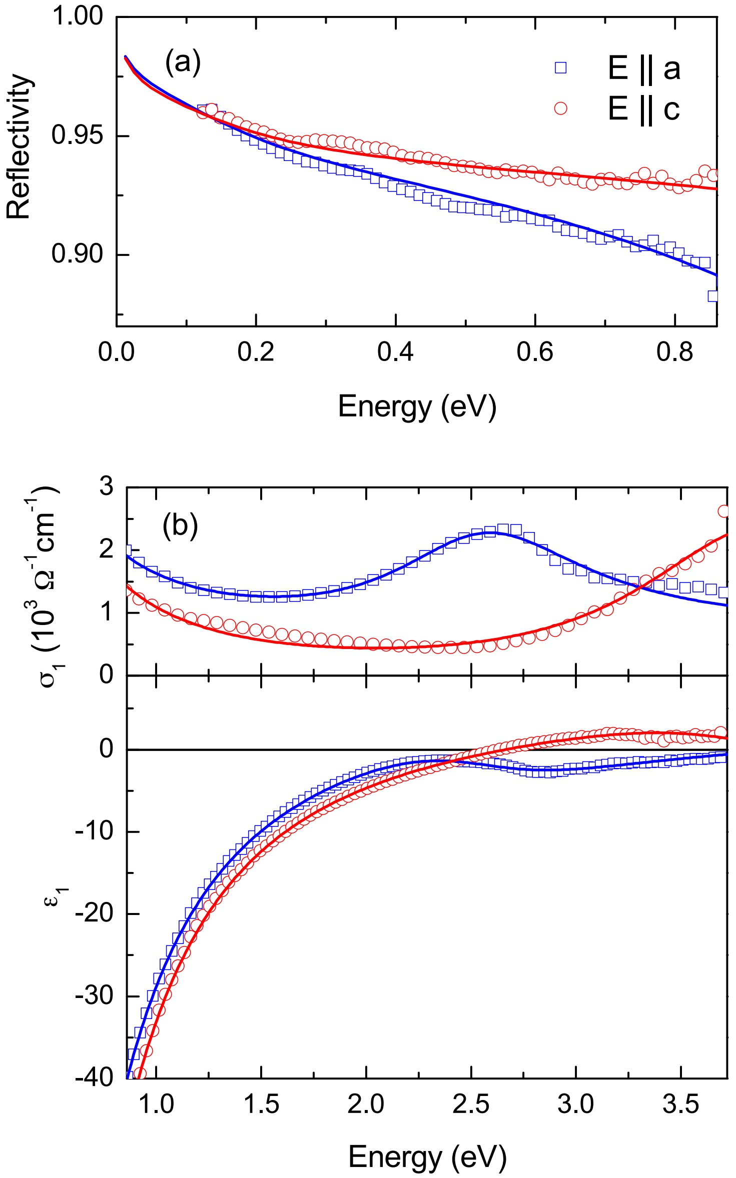

Figure 6.12: Multi-band fitting of the spectra. - Experimental data (symbols) and the multi-band fit (solid lines) of the reflectivity (a) and the dielectric function (b) along the a-axis (blue) and the c-axis (red).

phonon interaction, the absolute values of both $R_a(\omega)$ and $R_c(\omega)$ are quite sensitive to this parameter. In contrast, the value of $\gamma_{\sigma imp}$ does not significantly affect the spectra and cannot be accurately determined from the fit, because a large electron-phonon interaction in the σ-band dominates the total scattering above 100 meV at 300 K. However, $\gamma_{\sigma imp}$ influences drastically the shape of the temperature dependent in-plane dc resistivity $\rho_a(T) = 1/\sigma_{1,a}(\omega \to 0, T)$ curves, most notably the value of $\rho(300K)/\rho(40K)$ (RRR), as can be seen from figure 6.13. A measurement [127] on a crystal grown by the same group under similar conditions, showed RRR $\approx$ 5 along the a-axis. Therefore we have chosen of $\gamma_{\sigma imp}$ = 12.4 meV, which gives the same resistivity ratio (see figure 6.13). The assumption $\gamma_{\sigma imp} = \gamma_{\pi imp}$ gives RRR less than two, which strongly suggests that $\gamma_{\sigma imp}$ is actually several times smaller than $\gamma_{\pi imp}$. This agrees with the Raman study [135] on single crystals, where a relation $\gamma_{\pi imp}/\gamma_{\sigma imp} = 6-9$ was found, although the absolute values of the scattering rates are smaller than in our case.

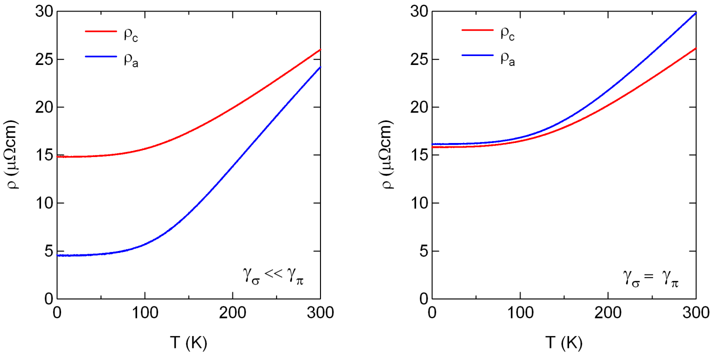

Figure 6.13: Temperature dependent resistivity. - The curves along the a-axis (blue) and c-axis (red), calculated using the results of the fit of the optical data for $\gamma_{\pi,imp}$ = 85.6 meV and different values of the scattering rate in the σ-band: $\gamma_{\sigma,imp}$ = 12.4 meV $\ll \gamma_{\pi imp}$ (left panel) and $\gamma_{\sigma,imp} = \gamma_{\pi,imp}$ (right panel).

A disparity between the impurity scattering rates in the two bands and a small interband $\sigma \leftrightarrow \pi$ scattering were proposed in Ref. [119] to explain the surprisingly small dependence of T_c on the impurity level, unexpected for a two-band superconductor. Microscopically, this can be explained by the fact that the electronic wave functions in σ-bands are confined to the boron planes and not efficiently scattered by the magnesium vacancies and substitutions. On the other hand, the same defects strongly scatter the electron states in the 3D π-bands. Our results support this conjecture.

The first Lorentz term for the a-axis at 2.6 eV clearly corresponds to the previously discussed interband transition. However, the second oscillator is extremely broad and it cannot be matched with a predicted interband peak at 0.35 eV. This probably means that this relatively weak peak is shifted and/or broadened so much that it cannot be identified in the optical spectrum. The second Lorentz term may thus describe the background formed by the tails of several broadened interband peaks.

6.9 The color of magnesium diboride

Finally we address a practical question: what is the color of MgB_2? The characterizations given in the literature varied significantly, ranging from the 'golden' and 'tan' to 'silver-metallic', 'black' and even 'blue'. Lee [136] has noticed that, depending on the polarization, "...the fresh surface of as-grown crystals in the ab-plane changes the color from silver to dark gray. In contrast, for the ac-plane of the crystals a beautiful change of color from golden-yellow to blue can be seen." Figure 6.14 shows the two images of the unpolished ac-plane of the sample S1 for different polarizations of the incident white light. One can see that the sample spectacularly changes color from a blueish-silver for $E \parallel ab$ to the yellow for $E \parallel c$. The explanation comes naturally from the reflectivity curves shown in figure 6.7(a). For the c-axis polarization, it is a sharp plasma edge at about 2.5 eV, the same as of gold, which makes the sample yellow. For the ab-plane polarization, the plasma edge is smeared due to the strong interband transition at 2.6 eV. As a result, the reflectivity spectrum in the visible range (1.8 - 3.1 eV) is relatively flat with a maximum (stronger in sample S2) at ~ 2.8 eV which makes the color blue-silver.

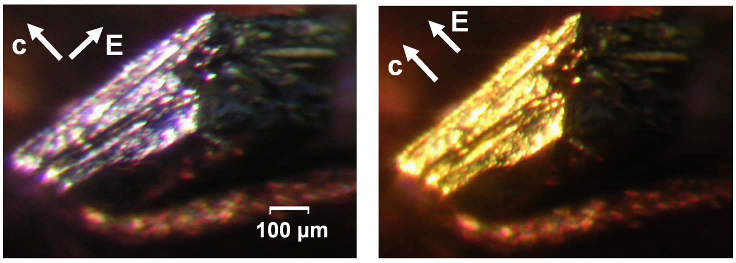

Figure 6.14: Color of MgB_2. - Two images of the same sample (ac-plane) made in a polarized light: $E \parallel ab$ (left) and $E \parallel c$ (right). The sample looks golden for $E \parallel c$, due to a sharp reflectivity plasma edge at around 2.5 eV, while the plasma edge is smeared for $E \parallel ab$ by a strong $\sigma \rightarrow \pi$ interband transition at 2.6 eV.

6.10 Effective-medium approximation

Using the effective medium theories it is possible to model the microstructure and characterize the optical properties of a complex system. Knowing the anisotropic spectra, we can predict the reflectivity shape of MgB$_2$ in polycrystalline form. If the light wavelength, λ, is much larger than a typical grain size, l, one can apply the effective-medium approximation (EMA) as prescribed in Ref. [137]. In the short-wavelength limit $\lambda \ll l$, it is more adequate to average directly the reflectivities along the two axes, as it was done in Ref. [121]. In figure 6.15 both calculated curves $R_{EMA}(\omega)$ (for sphere-like and plate-like crystallites) and $R_{av}(\omega) = (2/3)R_{ab}(\omega) + (1/3)R_c(\omega)$ are shown, together with the spectrum on a polycrystal from our previous study [118]. Notably, $R_{EMA}(\omega)$ and $R_{av}(\omega)$ are close to each other and their overall shape in the visible range matches well the measured spectrum. The latter shows only a weak step-like feature near 2.5 eV, coming from the c-axis contribution[121], which explains why the polycrystalline samples have typically black, or slightly tan, color. The absolute value of the experimental reflectivity from Ref. [118] is by 10-20% lower than the calculated one, which is likely caused by an overdamping of the π-bands due to a much higher impurity level (presumably MgO) of the sample used.

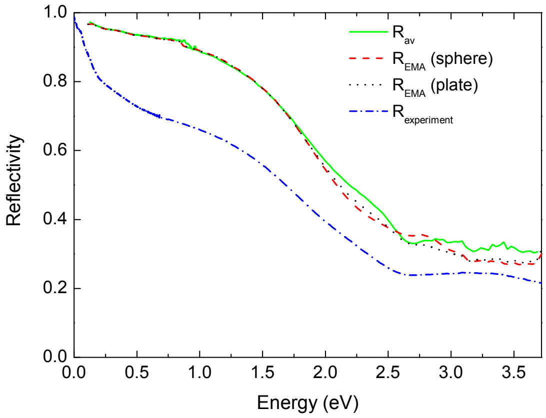

Figure 6.15: Comparison with the effective-medium approximation. - Reflectivity spectra of polycrystalline MgB$_2$ at 300 K. The spectra, calculated using the effective-medium approximation (spherical or plate-like crystallites) and the direct reflectivity averaging, are compared with experimental spectrum from Ref. [118].

6.11 Conclusions

We investigated anisotropic optical properties of MgB_2 single crystals of different purity at room temperature in the energy range 0.1 - 3.7 eV and compared them with the existing first-principle calculations of the electronic structure and electron-phonon coupling. The analysis of the anisotropy allowed us to distinguish properties of the σ- and π-bands. The total bare plasma frequencies along the in-plane and c-axis directions are almost the same and equal to 6.3 eV, which is much higher than the previously reported values. However, it is still smaller than the theoretical value of about 7 eV.

The shape of the Drude peak is well described by the electron scattering on phonons and impurities. The data suggest that the impurity scattering in the π-bands is several times larger than in the σ-bands in agreement with a proposal of Ref. [119], aimed to explain a surprisingly small dependence of the critical temperature on the sample purity. The electron-phonon interaction is stronger in the σ-bands, in agreement with the theory [101] and de Haas-van Alphen experiments [105].

The in-plane optical conductivity clearly shows an intense peak at 2.6 eV, which corresponds to a transition from the σ- to the π-band. It is higher by about 0.2 eV than the theoretical value. An interband peak due to the transitions between two close σ-bands, expected to be at 0.35 eV, was not seen in the experiments which can be explained by an overdamping or a shift towards lower frequencies relative to the theoretical calculations.

The width of the Drude peak and the interband $\sigma \rightarrow \pi$ peak at 2.6 eV are very sensitive to the sample purity. This can partially explain the spread of the results of previous optical studies.

The two quantitative mismatches between the experiment and the theory, namely (i) a smaller plasma frequency, (ii) a higher by 0.2 eV energy of the 2.6 eV $\sigma \rightarrow \pi$ transition, tell us that the σ-bands are probably shifted down and π-bands are shifted up compared to the calculations, so that their relative shift is about 0.2 eV. Notably, the same conclusion was derived in Ref. [133] from the analysis of the dHvA measurements [105].

The positions of the reflectivity plasma edges for two polarizations are very different ($\sim$ 2 eV for a-axis and $\sim$ 2.5 eV for the c-axis). This is caused by an additional screening of the intraband carriers by the interband transition at 2.6 eV, but not due to different ab-plane and c-axis bare plasma frequencies. As a result, the color of the sample depends on the polarization of the light: it is blueish-silver for E $\parallel$ a and yellow for E $\parallel$ c.

Unfortunately, due to the smallness of the sample the experimental range of optical studies was limited to room temperature and the mid-infrared frequency range. Far-infrared measurements at low-temperature are highly desirable in order to complete the understanding of the two-gap superconductivity in MgB$_2$.

Acknowledgements

I am very thankful to all those who contributed to the accomplishment of this thesis. First, I would like to express my sincere gratitude to Prof. Dirk van der Marel, for providing me the opportunity to work with several interesting topics, for the guidance you provided throughout all this five years on both theoretical and experimental area and for your patience and understanding. I am also thankful to you for numerous discussions on both scientific and non-scientific questions to which you have never been indifferent. Above all, I enjoyed a lot working with you.

It is a great pleasure for me to thank Prof. John Ditusa, Prof. Patrycja Paruch and Dr. Didier Jaccard for agreeing to join the thesis committee. Thank you also for your reading your comments and interesting questions.

Many thanks to crystal growth people for providing us with beautiful crystals for measurements: H. Wilhelm for FeGe samples, A. Huxley, S. S. Saxena for UGe_2 samples, V. K. Pecharsky for $Gd_5Si_2Ge_2$ sample and J. Karpinski for MgB_2 samples.

Special thanks go to Daniel and Paul for the great help by reading, checking and correcting of the manuscript.

I would like to thank Alexey for his help during experiments, for precious advices, for numerous discussions and very important contribution to MgB_2 project. It was great pleasure to work with you.

I am very grateful to Peter Armitage for the intense collaboration and fruitful discussions on the UGe_2 project. Our many discussions have allowed me to better understand the physics of heavy fermions.

I would also like to acknowledge Alexander Brinkman for helpful discussions, which stimulated the work on the $Gd_5Si_2Ge_2$ project.

7. ACKNOWLEDGEMENTS

It would be impossible to recall all the occasions when I received assistance from colleagues or discussing with me on one of the numerous topics. In particular I would like to thank Jeremie, Riccardo, Erik, Joachim, Fabrizio, Florence, Dook, Romain, Enrico, Hajo and Natalia. Thank you Riccardo for making beautiful pictures of the MgB_2 sample.

I especially want to thank Mehdi and Cor for the irreplaceable technical assistance and help during experiments. I would also like to thank Patrick Magnin, Patrick Cerutti and Géraldine Cravotto for their technical support, availability and kindness.

I am thankful to Edmond Koller and Jean-Noel Chotard for the x-ray diffraction and Laue measurements. Many thanks to Alexander Petrovic and Rolf Lortz for the specific heat and resistivity measurements.

I would also like to thank Iris, Iman, Michael, Jason, Julien, Alberto and Jack who joined the group recently.

I am grateful to T. Jarlborg for the interest in FeGe project. I would also like to acknowledge the interesting discussions with D. Basov and J. A. Mydosh.

I would like to sincerely thank the members of the physics department in particular, Christine, Fabienne, Nathalie and Lilianne for all their help and sympathy. Thank you a lot Fabienne for numerous letters you wrote for me.

Finally, I wish to thank my friends: Andrey, Aliona, Peggy, Josiane and my family for their ongoing encouragement and support during all these years.

Nevertheless, I would like to apologize to all whose contributions are not mentioned here.

Thanks a lot to all of you.
Violeta

References

[1] B. Lebech, J. Bernard, and T. Frelhoft. *J. Phys.: Condens. Matter* **1**, 6105 (1989).

[2] S. Yeo, S. Nakatsuji, A. D. Bianchi, P. Schlottmann, Z. Fisk, L. Balicas, P. A. Stampe, and R. J. Kennedy. *Phys. Rev. Lett.* **91**, 046401 (2003).

[3] V. Guritanu, D. van der Marel, J. Teyssier, T. Jarlborg, H. Wilhelm, M. Schmidt, and F. Steglichi. *Phys. Rev. B* **75**, 155114 (2007).

[4] S. S. Saxena, P. Agarwal, K. Ahilan, F. M. Grosche, S. R. Julian, P. Monthoux, G. G. Lonzarich, A. Huxley, I. Sheikin, D. Braithwaite, and J. Flouquet. *Nature* **604**, 587 (2000).

[5] Y. Ōnuki, S. W. Yun, I. Ukon, I. Umehara, K. Satoh, I. Sakamoto, M. Hunt, P. Meeson, P. A. Probst, and M. Springford. *J. Phys. Soc. Jpn.* **60**, 2127 (1991).

[6] V. Guritanu, N. P. Armitage, R. Tediosi, S. S. Saxena, A. Huxley, and D. van der Marel. *Phys. Rev. B* **78**, 172406 (2008).

[7] V. K. Pecharsky and K. A. Schneider Jr. *Phys. Rev. Lett.* **78**, 4494 (1997).

[8] V. K. Pecharsky and K. A. Gschneidner Jr. *J. Magn. Magn. Mater.* **167**, L179 (1997).

[9] V. K. Pecharsky and K. A. Gschneidner Jr. *J. Magn. Magn. Mater.* **200**, 44 (1999).

[10] J. Nagamatsu, N. Nakagawa, T. Muranaka, Y. Zenitani, and J. Akimitsu. *Nature* **410**, 63 (2001).

[11] I. I. Mazin and V. P. Antropov. *Physica C* **385**, 49 (2003).

[12] V. Guritanu, A. B. Kuzmenko, D. van der Marel, S. M. Kazakov, N. D. Zhigadlo, and J. Karpinski. *Phys. Rev. B* **73**, 104509 (2006).

[13] J. E. Hirsch. *Phys. Rev. B* **59**, 6256 (1999).

[14] E. C. Stoner. *Proc. R. Soc. London, Ser. A* **165**, 372 (1938).

[15] W. Heisenberg. *Z. Phys.* **49**, 619 (1928).

[16] T. Moriya. *Spin Fluctuations in Itinerant Electron Magnetism*. Springer, Verlag Berlin, Heidelberg, (1985).

[17] J. Kondo. *Prog. Theor. Phys.* **32**, 37 (1964).

[18] A. C. Hewson. *The Kondo Problem to Heavy Fermions*. Cambridge University Press, (1993).

[19] P. W. Anderson. *Phys. Rev.* **164**, 352 (1967).

[20] P. W. Anderson, G. Yuval, and D. R. Hamann. *Phys. Rev. B* **1**, 4464 (1970).

[21] K. G. Wilson. *Rev. Mod. Phys.* **47**, 773 (1975).

[22] N. Andrei. *Phys. Rev. Lett.* **45**, 379 (1980).

[23] P. B. Wiegmann. *Sov. Phys. JETP Lett.* **31**, 392 (1980).

[24] S. V. Dordevic, D. N. Basov, N. R. Dilley, E. D. Bauer, and M. B. Maple. *Phys. Rev. Lett.* **86**, 684 (2001).

[25] P. A. Lee, T. M. Rice, J. M. Serene, L. J. Sham, and J. W. Wilkins. *Comments Condens. Matter Phys.* **12**, 99 (1986).

[26] G. Zwicknagl. *Adv. Phys.* **41**, 203 (1993).

[27] P. Fulde, J. Keller, and G. Zwicknagl. *Solid State Physics* **41**, 1 (1988).

[28] T. Brugger, T. Schreiner, G. Roth, P. Adelmann, and G. Czjzek. *Phys. Rev. Lett.* **71**, 2481 (1993).

[29] S. Doniach. *Physica B* **91**, 231 (1977).

[30] A. Eiling and J. S. Schilling. *Phys. Rev. Lett.* **46**, 364 (1981).

[31] W. H. Lee, R. N. Shelton, S. K. Dhar, and K. A. Gschneider Jr. *Phys. Rev. B* **35**, 8523 (1987).

[32] D. Kaczorowski. *Solid State Commun.* **99**, 949 (1998).

[33] V. H. Tran, R. Troć, Z. Bukowski, D. Badurski, and C. Sulkowski. *Phys. Rev. B* **71**, 094428 (2005).

[34] N. B. Perkins, M. D. N. Regueiro, B. Coqblin, and J. R. Iglesias. *Phys. Rev. B* **76**, 125101 (2007).

[35] F. Wooten. *Optical properties of solids*. Academic Press, (1972).

[36] M. Dressel and G. Gruner. *Electrodynamics of solids*. Cambridge University Press, (2002).

[37] E. van Heumen and D. van der Marel. In *LECTURES ON THE PHYSICS OF STRONGLY CORRELATED SYSTEMS XI: Eleventh Training Course in the Physics of Strongly Correlated Systems,* F. Mancini and A. Avella, editors, AIP Conference Proceedings Volume 918, Materials Physics and Applications, 203. AIP, (2007).

[38] A. B. Kuzmenko. *Rev. Sci. Instrum.* **76**, 083108 (2005).

[39] R. Wäppling and L. Häggström. *Phys. Lett. A* **28**, 173 (1968).

[40] T. Jarlborg. *J. Mag. Mag. Mat.* **283**, 238 (2004).

[41] V. Jaccarino, G. K. Wertheim, J. H. Wernick, L. R. Walker, and S. Arajs. *Phys. Rev.* **160**, 476 (1967).

[42] Y. Takahashi and T. Moriya. **46**, 1451 (1979).

[43] G. Aeppli and Z. Fisk. *Comments Condens. Matter Phys.* **16**, 155 (1192).

[44] D. Mandrus, J. L. Sarrao, A. Migliori, J. D. Thompson, and Z. Fisk. *Phys. Rev. B* **51**, 4763 (1995).

[45] V. I. Anisimov, S. Y. Ezhov, I. S. Elfimov, I. V. Solovyev, and T. M. Rice. *Phys. Rev. Lett.* **76**, 1735 (1996).

[46] K. Urasaki and T. Saso. *Physica B* **282**, 313 (2000).

[47] Z. Schlesinger, Z. Fisk, Hai-Tao Zhang, M. B. Maple, J. F. DiTusa, and G. Aeppli. *Phys. Rev. Lett.* **71**, 1748 (1993).

[48] A. Damascelli, K. Schulte, D. van der Marel, and A. A. Menovsky. *Phys. Rev. B* **55**, R4863 (1997).

[49] T. Jarlborg. *Phys. Rev. B* **59**, 15002 (1999).

[50] V. I. Anisimov, R. Hlubina, M. A. Korotin, V. V. Mazurenko, T. M. Rice, A. O. Shorikov, and M. Sigrist. *Phys. Rev. Lett.* **89**, 257203 (2002).

[51] P. Pedrazzini, H. Wilhelm, D. Jaccard, T. Jarlborg, M. Schmidt, M. Hanfland, L. Akselrud, H. Q. Yuan, U. Schwarz, Yu. Grin, and F. Steglich. *Phys. Rev. Lett.* **98**, 047204 (2007).

[52] M. Richardson. *Acta Chem. Scand.* **21**, 2305 (1967).

[53] R. B. Coles. *Solid State Commun.* **1**, 5 (1963).

[54] F. P. Mena, D. van der Marel, and J. L. Sarrao. *Phys. Rev. B* **72**, 045119 (2005).

[55] J. F. DiTusa, K. Friemelt, E. Bucher, G. Aeppli, and A. P. Ramirez. *Phys. Rev. B* **58**, 10301 (1998).

[56] D. A. Bonn, J. D. Garrett, and T. Timusk. *Phys. Rev. Lett.* **61**, 1305 (1988).

[57] A. M. Awasthi, L. Degiorgi, G. Grüner, Y. Dalichaouch, and M. B. Maple. *Phys. Rev. B* **48**, 10692 (1993).

[58] F. P. Mena. PhD thesis, (2004).

[59] E. J. Singley, C. P. Weber, D. N. Basov, A. Barry, and J. M. D. Coey. *Phys. Rev. B* **60**, 4126 (1999).

[60] N. Manyala, Y. Sidis, J. F. DiTusa, G. Aeppli, D. P. Young, and Z. Fisk. *Nature* **404**, 581 (2000).

[61] N. Manyala, Y. Sidis, J. F. DiTusa, G. Aeppli, D. P. Young, and Z. Fisk. *Nat. Mater.* **3**, 255 (2004).

[62] F. P. Mena, J. F. DiTusa, D. van der Marel, G. Aeppli, D. P. Young, A. Damascelli, and J. A. Mydosh. *Phys. Rev. B* **73**, 085205 (2006).

[63] D. van der Marel, A. Damascelli, K. Schulte, and A. A. Menovsky. *Physica B* **244**, 138 (1998).

[64] V. L. Ginzburg. *Sov. Phys. JETP* **4**, 153 (1957).

[65] D. Fay and J. Appel. *Phys. Rev. B* **22**, 3173 (1980).

[66] A. Huxley, I. Sheikin, E. Ressouche, N. Kernavanois, D. Braithwaite, R. Calemczuk, and J. Flouquet. *Phys. Rev. B* **63**, 144519 (2001).

[67] C. Pfleiderer and A. D. Huxley. *Phys. Rev. Lett.* **89**, 147005 (2002).

[68] C. G. Oomi, T. Kagayama, and Y. Ōnuki. *J. Alloys Compd.* **271-273**, 482 (1998).

[69] N. Tateiwa, K. Hanazono, T. C. Kobayashi, K. Amaya, T. Inoue, K. Kindo, Y. Koike, N. Metoki, N. Y. Haga, R. Settai, and Y. Onuki. *J. Phys. Soc. Jpn.* **70**, 2876 (2001).

[70] K. G. Sandeman, G. G. Lonzarich, and A. J. Schofield. *Phys. Rev. Lett.* **90**, 167005 (2003).

[71] A. B. Shick, V. Janiš, V. Drchal, and W. E. Pickett. *Phys. Rev. B* **70**, 134506 (2004).

[72] G. Oomi, T. Kagayama, K. Nishimura, S. W. Yun, and Y. Ōnuki. *Physica B* **206-207**, 515–518 (1995).

[73] G. Motoyama, S. Nakamura, H. Kadoya, T. Nishioka, and N. K. Sato. *Phys. Rev. B* **65**, 020510R (2001).

[74] K. Oikawa, T. Kamiyama, H. Asano, Y. Ōnuki, and M. Kohgi. *J. Phys. Soc. Jpn.* **65**, 3229 (1996).

[75] K. S. Burch and A. Schafgans. *Phys. Rev. Lett.* **95**, 046401 (2005).

[76] M. Biasini and R. Troc. *Phys. Rev. B* **68**, 245118 (2003).

[77] T. M. Rice and K.Ueda. *Phys. Rev. B* **34**, 6420 (1986).

[78] J. H. Shim, K. Haule, and G. Kotliar. *Science* **318**, 1615 (2007).

[79] H. Weber and M. Vojta. *Phys. Rev. B* **77**, 125118 (2008).

[80] A. J. Millis and P. A. Lee. *Phys. Rev. B* **35**, 3394 (1987).

[81] K. S. Burch, S. V. Dordevic, F. P. Mena, A. B. Kuzmenko, D. van der Marel, J. L. Sarrao, J. R. Jeffries, E. D. Bauer, M. B. Maple, and D. N. Basov. *Phys. Rev. B* **75**, 054523 (2007).

[82] D. E. Eastman, F. J. Himpsel, and J. A. Knapp. *Phys. Rev. Lett.* **40**, 1514 (1978).

[83] N. Furukawa. *Physics of Manganites, ed. T. Kaplan and S. Mahanti (Plenum Publishing, New York)* (1999).

[84] A. B. Shick and W. E. Pickett. *Phys. Rev. Lett.* **86**, 300 (201).

[85] H. Yamagami. *J. Phys.: Condens. Matter* **15**, S2271 (2003).

[86] A. D. Huxley, S. Raymond, and E. Ressouche. *Phys. Rev. Lett.* **91**, 207201 (2003).

[87] N. Aso, G. Motoyama, Y. Uwatoko, S. Ban, S. Nakamura, T. Nishioka, Y. Homma, Y. Shiokawa, K. Hirota, and N. K. Sato. *Phys. Rev. B* **73**, 054512 (2006).

[88] V. K. Pecharsky, G. D. Samolyuk, V. P. Antropov, A. O. Pecharsky, and K. A. Gschneider Jr. *J. Solid State Chem.* **171**, 57 (2003).

[89] L. Morellon, P. A. Algarabel, M. R. Ibarra, J. Blasco, B. García-Landa, Z. Arnold, and F. Albertini. *Phys. Rev. B* **58**, R14721 (1998).

[90] L. Morellon, J. Stankiewicz, B. García-Landa, P. A. Algarabel, and M. R. Ibarra. *Appl. Phys. Lett.* **73**, 3462 (1998).

[91] F. Holtzberg, R. J. Gambino, and T. R. McGuire. *J. Phys. Chem. Solids* **28**, 2283 (1967).

[92] V. K. Pecharsky and K. A. Gschneider Jr. *J. Alloys Compd* **260**, 98–106 (1997).

[93] W. Choe, V. K. Pecharsky, A. O. Pecharsky, K. A. Gschneidner Jr., V. G. Young Jr., and G. J. Miller. *Phys. Rev. Lett.* **84**, 4617 (2000).

[94] D. Paudyal, V. K. Pecharsky, K. A. Gschneidner Jr., and B. N. Harmon. *Phys. Rev. B* **73**, 144406 (2006).

[95] M. Born and E. Wolf. *Principles of Optics*. Pergamon Press, London, 6th ed., (1980).

[96] A. B. Kuzmenko, E. A. Tishchenko, and V. G. Orlov. *J. Phys.: Condens. Matter* **8**, 6199 (1996).

[97] B. N. Harmon and V. N. Antonov. *J. Applied Phys.* **91**, 9815 (2002).

[98] J. Y. Rhee. *Journ. Kor. Phys. Soc.* **43**, 621 (2003).

[99] J. M. Park, D. W. Lynch, S. J. Lee, D. L. Schlagel, T. A. Lograsso, A. O. Tsokol, J. E. Snyder, and D. C. Jiles. *Phys. Rev. B* **73**, 035110 (2006).

[100] E. M. Levin, V. K. Pecharsky, and K. A. Gschneidner Jr. *Phys. Rev. B* **60**, 7993 (1999).

[101] Y. Kong, O. V. Dolgov, O. Jepsen, and O. K. Andersen. *Phys. Rev. B* **64**, 020501(R) (2001).

[102] S. L. Bud'ko, G. Lapertot, C. Petrovic, C. E. Cunningham, N. Anderson, and P. C. Canfield. *Phys. Rev. Lett.* **86**, 1877 (2001).

[103] D. G. Hinks, H. Claus, and J. D. Jorgensen. *Nature* **411**, 6836 (2001).

[104] H. Uchiyama, K. M. Shen, S. Lee, A. Damascelli, D. H. Lu, D. L. Feng, Z. X. Shen, and S. Tajima. *Phys. Rev. Lett.* **88**, 157002 (2002).

[105] E. A. Yelland, J. R. Cooper, A. Carrington, N. E. Hussey, P. J. Meeson, S. Lee, A. Yamamoto, and S. Tajima. *Phys. Rev. Lett.* **88**, 217002 (2002).

[106] Y. Wang, F. Bouquet, I. Sheikin, P. Toulemonde, B. Revaz, M. Eisterer, H. W. Weber, J. Hinderer, and A. Junod. *J. Phys.: Condens. Matter* **15**, 883 (2003).

[107] F. Bouquet, Y. Wang, I. Sheikin, T. Plackowski, A. Junod, S. Lee, and S. Tajima. *Phys. Rev. Lett.* **89**, 257001 (2002).

[108] A. A. Golubov, J. Kortus, O. V. Dolgov, O. Jepsen, Y. Kong, O. K. Andersen, B. J. Gibson, K. Ahn, and R. K. Kremer. *J. Phys.: Condens. Matter* **14**, 1353 (2002).

[109] M. R. Eskildsen, M. Kugler, S. Tanaka, J. Jun, S. M. Kazakov, J. Karpinski, and O. Fischer. *Phys. Rev. Lett.* **89**, 187003 (2002).

[110] S. Galambosi, J. A. Soininen, A. Mattila, S. Huotari, S. Manninen, Gy. Vankó, N. D. Zhigadlo, J. Karpinski, and K. Hämäläinen. *Phys. Rev. B* **71**, 060504R (2005).

[111] B. Gorshunovand C. A. Kuntscher, P. Haas, M. Dressel, F. P. Mena, A. B. Kuzmenko, D. van der Marel, T. Muranaka, and J. Akimitsu. *Eur. Phys. J. B* **21**, 159 (2001).

[112] R. A. Kaindl, M. A. Carnahan, J. Orenstein, D. S. Chemla, H. M. Christen, H. Y. Zhai, M. Paranthaman, and D. H. Lowndes. *Phys. Rev. Lett.* **88**, 027003 (2002).

[113] A. Pimenov, A. Loidl, and S. I. Krasnosvobodtsev. *Phys. Rev. B* **65**, 172502 (2002).

[114] J. H. Jung, K. W. Kim, H. J. Lee, M. W. Kim, T. W. Noh, W. N. Kang, Hyeong-Jin Kim, Eun-Mi Choi, C. U. Jung, and Sung-Ik Lee. *Phys. Rev. B* **65**, 052413 (2002).

[115] A. Perucchi, L. Degiorgi, J. Jun, M. Angst, and J. Karpinski. *Phys. Rev. Lett.* **89**, 097001 (2002).

[116] M. Ortolani, D. Di Castro, P. Postorino, I. Pallecchi, M. Monni, M. Putti, and P. Dore. *Phys. Rev. B* **71**, 172508 (2005).

[117] J. J. Tu, G. L. Carr, V. Perebeinos, C. C. Homes, M. Strongin, P. B. Allen, W. N. Kang, E. M. Choi, H. J. Kim, and S. Lee. *Phys. Rev. Lett.* **87**, 277001 (2001).

[118] A. B. Kuzmenko, F. P. Mena, H. J. A. Molegraaf, D. van der Marel, B. Gorshunov, M. Dressel, I. I. Mazin, J. Kortus, O. V. Dolgov, T. Muranaka, and J. Akimitsu. *Solid State Commun.* **121**, 479 (2002).

[119] I. I. Mazina, O. K. Andersen, O. Jepsen, O. V. Dolgov, J. Kortus, A. A. Golubov, A. B. Kuzmenko, and D. van der Marel. *Phys. Rev. Lett.* **89**, 107002 (2002).

[120] Mi-Ock Mun, Young Jin Kim, Yu Park, Jae Hoon Kim, S. H. Moon, H. N. Lee, H. G. Kim, and B. Oh. *J. Supercond.* **15**, 475 (2002).

[121] Y. Fudamoto and S. Lee. *Phys. Rev. B* **68**, 184514 (2003).

[122] F. Marsiglio. *Phys. Rev. Lett.* **87**, 247001 (2001).

[123] E. G. Maksimov, J. Kortus, O. V. Dolgov, and I. I. Mazin. *Phys. Rev. Lett.* **89**, 129703 (2002).

[124] D. Chvostova, V. Zelezny, L. Pajasova, A. Tarasenko, A. Plecenik, P. Kus, and L. Satrapinsky. *Thin Solid Films* **455**, 213 (2004).

[125] J. Karpinski, M. Angst, J. Jun, S. M. Kazakov, R. Puzniak, A. Wisniewski, J. Roos, H. Keller, A. Perucchi, L. Degiorgi, M. R. Eskildsen, P. Bordet, L. Vinnikov, and A. Mironov. *Supercond. Sci. Technol.* **16**, 221 (2002).

[126] D. E. Aspnes. *J. Opt. Soc. Am.* **70**, 1275 (1980).

[127] A. V. Sologubenko, J. Jun, S. M. Kazakov, J. Karpinski, and H. R. Ott. *Phys. Rev. B* **66**, 014504 (2002).

[128] O. V. Dolgov and S. V. Shulga. *J. Supercond.* **8**, 511 (1995).

[129] V. P. Antropov, K. D. Belashchenko, M. van Schilfgaarde, and S. N. Rashkeev. *Studies of High Temperature Superconductors* **38**, 91 (2002).

[130] P. Ravindran, P. Vajeeston, R. Vidya, A. Kjekshus, and H. Fjellvag. *Phys. Rev. B* **64**, 224509 (2001).

[131] J. Kortus, I. I. Mazin, K. D. Belashchenko, V. P. Antropov, and L. L. Boyer. *Phys. Rev. Lett.* **86**, 4656 (201).

[132] W. Ku, W. E. Pickett, R. T. Scalettar, and A. G. Eguiluz. *Phys. Rev. Lett.* **88**, 057001 (2002).

[133] H. Rosner, J. M. An, W. E. Pickett, and S.-L. Drechsler. *Phys. Rev. B* **66**, 024521 (2002).

[134] D. Di Castro, M. Ortolani, E. Cappelluti, U. Schade, N. D. Zhigadlo, and J. Karpinski. *Phys. Rev. B* **73**, 174509 (2006).

[135] J. W. Quilty, S. Lee, S. Tajima, and A. Yamanaka. *Phys. Rev. Lett.* **90**, 207006 (20003).

[136] S. Lee. *Physica C* **31**, 385 (2003).

[137] P. E. Sulewski, T. W. Noh, J. T. McWhirter, and A. J. Sievers. *Phys. Rev. B* **36**, 5735 (1987).